Terahertz Antenna Design for Future Wireless Communication

Abdoalbaset Abohmra

Submitted in fulfilment of the requirements for the Degree of Doctor of Philosophy

School of Engineering
College of Science and Engineering
University of Glasgow

February 2021

Abstract

A Terahertz (THz) antenna with a size of a few micrometres cannot be accomplished by just reducing the extent of a traditional metallic antenna down to a couple of micrometres. This approach has several downsides. For example, the low mobility of electrons in nanoscale metallic structures would result in high channel attenuation. Thus, using traditional micrometre metallic antennas for THz wireless communication becomes unfeasible. The THz band refers to the electromagnetic spectrum between the microwave and infrared frequency bands, which is colloquially referred to as the band gap due to the lack of materials and technological advancements. As opposed to their visible-spectrum features, metals such as gold and silver, which typically exhibit surface plasmon polaritons (SPPs), have completely different THz physical properties. 2D materials, which typically refer to single-layer materials, have been the focal point of researchers since the advent of graphene. 2D materials, for example, graphene, perovskite, and MoS2 (TMDs), provide a ground-breaking stage to control the propagation, modulation, and detection of THz waves. Moreover, 2D materials can enable the propagation of SPP waves in the THz band. These materials offer a promise of a future technological revolution. Combined with other profound advantages in lightweight, mechanical flexibility, and environmental friendliness, 2D materials can be used to fabricate low-cost wearable devices. This study also reported $CH_3NH_3PbI_3$ perovskite as a promising material for THz antennas for wearable applications. $CH_3NH_3PbI_3$ has a high charge carrier mobility and diffusion length, indicating that this material is a potential candidate for antenna design. The attractive feature about perovskite, graphene and other 2D materials is the ultra-high specific surface areas that enable their energy band structures to be sensitive to external basing. In the literature, scientists have tested a wide range of nano-antenna designs using modelling and simulation approaches. Nano-antenna fabrication and measurement using 2D materials is still the missing piece in the THz band. The design, fabrication, and measurement of THz antennas based on 2D materials for wearable wireless communication is the primary goal of this PhD study, including designing, fabrication, and measurement. In this study, we have designed, fabricated, and measured five different designs using different materials in the THz band, which will pave the way for enabling future THz short-range wireless communication.

Contents

List of Tables

List of Figures

Acknowledgements

First and foremost, I am extremely thankful to my supervisor **Prof. Qammer H. Abbasi** for giving me the opportunity to work in this exciting field and for his guidance and motivation and the freedom he provided me to pursue my research. I would also like to thank my co supervisor Dr. Hassan Abbas for his guidance and support during my first and second year. I would also like to thank my other co-supervisor Prof. Muhammad Ali Imran and for his technical guidance and support. Special thanks to Abbasi lab group for amazing memories, dinners, parties, and trips. I am also extremely grateful to the staffs of JWNC, without whose support none of the work in this report would have been possible. Finally and most importantly, I am thankful to my wonderful family. I would like to thank my Mom and Dad for the love and support I have had received since the day I was born. I would like to thank my wife for her patient during my PhD study.

List of Symbols, Acronyms

- THz Terahertz.
- mmWave Millimetre wave.
- IoT Internet of Things.
- GHz Gigahertz.
- SEM Scanning electron microscope.
- 2DMs Two-dimensional materials.
- h-bn Hexagonal boron nitride material
- SPPs surface plasmon polaritons.
- $CH_3NH_3PbI_3$ Lead halide perovskites.
- WBANs wireless body area networks
- PEN Polyethylene naphthalate
- PET polyethylene terephthalate
- RF Radio Frequency.
- RIE Reactive Ion Etching.
- PICA planar inverted cone antenna.
- SEM Scanning Electron Microscope.
- SOLT Short-Open-Load-Thru.
- S-parameters Scattering Parameters.
- PEC perfect electric conductor
- Ebl Electroin beam lithography.

- GSG Ground signal ground
- GSGSG Ground signal ground signal ground
- SPs surface plasmons
- SPR surface plasmon resonance
- RHM Remote Health Monitoring
- ISM Industrial Scientific Medical
- BCNs connectivity in body-centric networks
- EM electromagnetic wave
- IPA Isopropyl alcohol
- Al aluminum
- CPW coplanar waveguide
- CVD Chemical vapor deposition
- SEM scanning electron microscope.
- AFM atomic force microscopy
- VCO Voltage Controlled Oscillator.
- STDs Schottky diodes.
- VNA Vector Network Analyser.
- UTC-PDs uniform-traveling-carrier photodiodes.

Declaration

With the exception of chapters 1, 2 and 3, which contain introductory material, all work in this thesis was carried out by the author unless otherwise explicitly stated.

List of Publication

The work presented in this thesis has culminated in the following journal publications and conference proceedings:

[Journal]

1. Abohmra, A., Abbas, H. , Al-Hasan, M., Mabrouk, I. B., Alomainy, A., Imran, M. A. and Abbasi, Q. H. (2020) Terahertz antenna array based on a hybrid perovskite structure. IEEE Open Journal of Antennas and Propagation, 1, pp.464 − 471 (**The paper was one of the most popular papers on IEEE open access journal, from August 2020 to March 2021.**)

2. Abohmra, A., Abbas, H. , Kazim, J. u. R., Rabbani, M. S., Li, C. , Alomainy, A., Imran, M. A. and Abbasi, Q. H. (2021) An ultrawideband microfabricated gold-based antenna array for terahertz communication. IEEE Antennas and Wireless Propagation Letters,(doi : 10.1109/$LAWP$.2021.3072562) (**The paper presents the first fabricated antenna that operates at 1 THz frequency.**)

3. Abohmra, A., Khan, Z. U., Abbas, H. T., Shoaib, N., Imran, M. A. and Abbasi, Q. H. (2022) Two-dimensional materials for future terahertz wireless communications. IEEE Open Journal of Antennas and Propagation. (**The paper considered for inclusion among the featured articles of OJAP's website**)

[Book]

1. Baset, A. Imran, M. A., Alomainy, A. and Abbasi, Q. H. (2019) Terahertz antenna design for wearable applications. In: Alomainy, A., Yang, K., Imram, M. A., Yao, X.-W. and Abbasi, Q. H. (eds.) Nano-Electromagnetic Communication at Terahertz and Optical Frequencies: Principles and Applications. Institution of Engineering and Technology, pp. 57-75. ISBN 9781785619038. **(Book chapter)**

[Conferences: Best papers award]

1. Abohmra, A., Ramani, S., Sharif, A., Imran, M. A. , Abbasi, Q. and Ahmad, W. (2019) Novel Flexible and Wearable 2.4 GHz Antenna for Body Centric Applications. In: 2nd IEEE International Workshop on Healthcare with Intelligent Sensing, System, and Data (HISSD), Fukuoka, Japan, 05-08 Aug 2019, pp. 402-405. ISBN 9781728130248

2. Abohmra, A., Jilani, F., Abbas, H., Ghannam, R. , Heidari, H. , Imran, M. A. and Abbasi, Q. H. (2019) Low-profile Flexible Perovskite based Millimetre Wave Antenna. In: IEEE MTT-S 2019 International Microwave Biomedical Conference (IMBioC2019), Nanjing, China, 6-8 May 2019, ISBN 9781538673959 (doi:10.1109/IMBIOC.2019.8777839)

3. Abohmra, A., Jilani, F., Abbas, H., Alomainy, A., Imran, M. A. and Abbasi, Q. H. (2019) Terahertz Antenna based on Graphene for Wearable Applications. In: 6th IEEE MTT-S International Wireless Symposium (IEEE IWS 2019), Guangzhou, China, 19-22 May 2019, ISBN 9781728107172

[Conferences]

1. Abohmra, A., Jilani, F., Abbas, H., Alomainy, A., Ur-Rehman, M. , Imran, M. A. and Abbasi, Q. H. (2019) Flexible and Wearable Graphene-based Terahertz Antenna for Body-Centric Applications. In: 2019 Second International Workshop on Mobile Terahertz Systems (IWMTS), Bad Neuenahr, Germany, 01-03 Jul 2019,

2. Abohmra, A., Jilani, F., Abbas, H. , Alomainy, A., Imran, M. A. and Abbasi, Q. H. (2019) Hybrid Terahertz Antenna Design for Body-Centric Applications. In: IET Antennas and Propagation Conference (APC 2019), Birmingham, UK, 11-12 Nov 2019,

3. Abohmra, A., Kazim, J., Abbas, H. , Imran, M. , Alomainy, A., Rehman, M. and Abbasi, Q. H. (2021) Ultra-wideband Hybrid PICA Terahertz Antenna for High-Resolution Biomedical Imaging. In: 2020 IEEE International Symposium on Antennas and Propagation and North American Radio Science Meeting, Montréal, QC, Canada, 05-10 Jul 2020, pp. 1759-1760. ISBN 9781728166704

4. Abohmra, A., Jilani, S., Abbas, H., Alomainy, A., Imran, M. and Abbasi, Q.(2019) High Bandwidth Perovskite Based Antenna forHigh-ResolutionBiomedical Imaging at Terahertz. In: 2019 IEEE Symposium on Antennas and Propagation and USNC-URSI Radio Science Meeting, At 7 anta, GA, USA, 07 – 12 Ju1 2019, ISBN 9781728106922 doi:10.1109/APUSNCURSINRSM.2019.8888453

5. Omeke, K. G., Abohmra, A., Imran, M. A. , Abbasi, Q. H. and Zhang, L. (2019) Characterization of RF signals in Different Types of Water. In: Antennas and Propagation Conference 2019, Birmingham, UK, 11-12 Nov 2019, ISBN 9781839531705

6. Kazim, J. u. R., Ur-Rehman, M. , Abohmra, A., Sheikh, F., Kaiser, T., Al-Hasan, M., Mabrouk, I. B., Imran, M. A. and Abbasi, Q. H. (2020) A 1-bit High-Gain Flexible Metasurface Reflectarray for Terahertz Application. In: Third International Workshop on Mobile Terahertz Systems (IWMTS 2020), Essen, Germany, 02-03 Jul 2020, ISBN

7. Kazim, J. u. R., Abohmra, A., Ur Rehman, M. , Imran, M. A. and Abbasi, Q. H. (2021) A Corrugated SIW Based Slot Antenna for Terahertz Application. In: 2020 IEEE International Symposium on Antennas and Propagation and North American Radio Science Meeting, Montréal, QC, Canada, 05-10 Jul 2020, pp. 1407-1408. ISBN

Chapter 1

Introduction

Terahertz (THz) waves, known as sub-millimetre waves are observed between the optical and microwave frequency regions of the electromagnetic spectrum [1,2]. This is the frequency range between 0.3 GHz and 10 THz (between 1 mm and 30um for free space wavelength (λ)) [3]. In addition to that, also refers to the frequency range between 0.1 GHz and 10 THz [4].

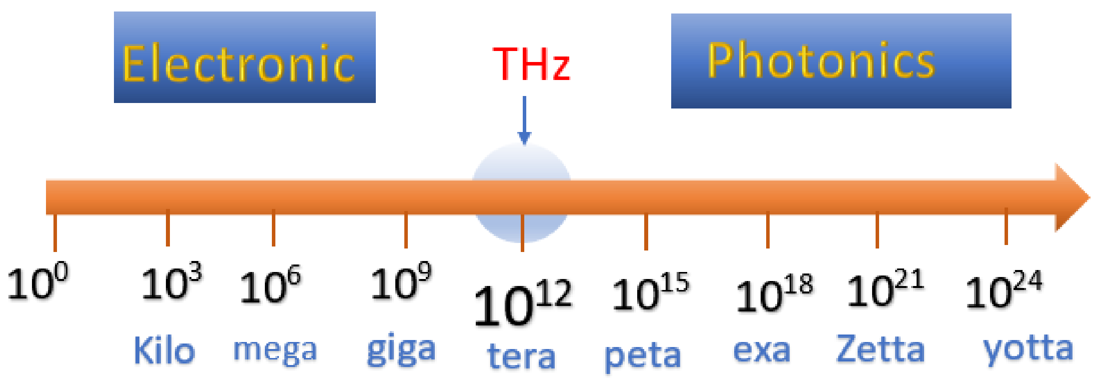

Figure 1.1: Electromagnetic spectrum illustrating the THz frequency band's placement between the radio and infrared spectrums.

THz radiation is non-ionizing, making it a safer alternative to other forms of ionising radiation used in medical diagnostics, such as X-rays, which may have physiological consequences. Additionally, although THz radiation can not permeate metals or water, it does penetrate a wide variety of ordinary materials, including leather, fabric, cardboard, wood, clothes, plastic, ceramics, and paper, enabling novel sensing possibilities [5]. Portable THz technology would enhance airport security by allowing for the identification of harmful goods. THz frequencies may provide very wide bandwidths, in the tens of GHz range. As a result, it has the ability to support very high data rates in the tens of Gbps [6].

THz frequencies may be used in a variety of scientific domains, including medical diagnostics, security imaging, and wireless communication. Devices operating in the optical and infrared spectra are generally characterized by electromagnetic beams that contain many modes, and the dimensions of such devices are typically much larger than the operating wavelength. On the contrary, THz frequency-based devices are comparable in size to the operating wavelength [7]. Such devices have the potential to fulfil the future wireless communications need of ultra−high bandwidth and data rates. Moreover, the problems of channel congestion can be overcome using THz based communication systems. There has been an ever-increasing demand for data-based wireless communication in the past decade. Moreover, throughout the world, the urban population has been growing at an alarming rate. These two factors have created enormous challenges in implementing high-speed and reliable networks that can serve many people at the same time [8].

A natural solution to overcome this challenge is to shift the network operating frequency to the THz region. However, with the available technologies, THz systems are affected by high atmospheric attenuation and therefore, yield much lower propagation distances. Hence, there is a demand for novel techniques through which the performance of a THz based communication system can be increased. To do so, micro-and nanoscale device fabrication techniques have of late been actively studied. Additionally, the search for highly conductive materials is an active research area to develop efficient THz devices. In conventional wireless communication systems, metallic antennas are fabricated separately from microelectronics. It is not currently possible to operate the circuitry in the THz frequency region simply by downscaling the traditional metallic antenna to a few micrometres [9]. The downside of small metallic structures is their limited electron mobility. As a result, metallic antennas have a lower frequency limit. They will eventually cease to resonate and will cease to convey any energy. Additionally, metallic antennas are not tuneable. If you alter the frequency, you must likewise alter the size.

By moving up in the frequency, the device physics changes drastically and the approach of using a metal-based antenna has several limitations, chief among them is the low mobility of electrons in the nanoscale metallic structures. This results in the antennas being highly lossy at the resonant frequencies, which would result in a high attenuation and subsequently, poor efficiency of the overall system [10]. To address this lossy behaviour, meta-material-based nanostructures have emerged as attractive solutions [11]. Graphene is an atomically thin, two-dimensional crystalline form of carbon in which the carbon atoms are arranged in a hexagonal lattice structure. It was discovered in 2004 by Novoselov and Geim, who peeled off a small amount of monolayer graphene with the help of adhesive tape, therefore, obtaining free-standing graphene in the air. For their ground−breaking discovery, they were awarded the Nobel Prize in Physics in 2010. Graphene is considered one of the thinnest materials yet in terms of mechanical properties, the strongest material measured [12]. Its theoretical specific surface area is as high as $2630\,\mathrm{m^2\,g^{-1}}$, thermal conductivity as high as $5300\,\mathrm{W\,m^{-1}\,K^{-1}}$ at room temperature, which is higher than that of carbon nanotube or crystalline silicon [13].

Nonetheless, the electrical resistivity of graphene is of the order of $1 \times 10^{-6}\,\Omega\mathrm{cm}$, lower than copper and silver, which are considered the best conducting materials. All these attractive

Materials	Fundamental properties at THz
2DMs	supporting surface plasmon propagation at THz. Superconductivity. Tunnelling. Ultra-thin material. flexible
Conventional materials	High loss material at nano structure high surface resistivity. Low SPP at THz

Table 1.1: A comparison between conventional materials and 2DMS

characteristics enable graphene to display extra-ordinary electromagnetic phenomena. When an electromagnetic wave, especially in the THz frequency range is an obliquely incident wave upon graphene, SPPs are excited. Due to the high conductivity of graphene, the SPPs are tightly confined to the graphene surface having a wavelength much smaller than its free-space equivalent. Moreover, the graphene SPPs exhibit moderate loss, and vital property of tuning of the resonant frequency through external electrical and magnetic bias and chemical doping [14]. Most importantly, the resonant frequency of graphene lies in the THz and mid-infrared frequency ranges.

Hence, this property, coupled with the lightweight and flexible nature of graphene, opens the possibility of creating miniaturized and flexible antenna devices operating in the THz frequency domain that is well suited for wearable applications. The electrical conductivity of graphene in the THz frequency range can be described using a semi−classical electronic model in the absence of magnetic bias [15].

This leads to poor efficiency in terms of radiation as the SPPs have a lower propagation length along the graphene surface. Therefore, to observe a strong resonant behaviour and improve efficiency, μ_c needs to be enhanced, which is usually done through chemical doping. Although both the increase in μ_c and μ lead to efficient radiation, the effect on the resonant frequency is different in both cases. Moreover, an increase in the radiated energy affects the width of the resonant frequency response introducing ringing tails around the centre frequency. Such broadening of the temporal response is coherent with the sharpening of the resonant behaviour that is observed when μ is increased. On the other hand, a stronger resonant behavior is observed when τ is increased [16]. On the other hand, perovskite which was first discovered in the Ural Mountains and named after a Russian scientist, Lev Perovskite [17], is a mineral with a unique crystalline structure. A perovskite structure is any intensified that has a similar structure to the perovskite mineral.

True perovskite (mineral) is made of calcium, titanium, and oxygen in the structure $CaTiO_3$. Then, a perovskite structure is whatever has the conventional structure ABX_3 and the equivalent crystallographic structure as the mineral perovskite [18]. Perovskites have been widely inspected all around the world given their attractive properties especially regards to their photovoltaic and plasmonic applications [19]. Perovskite materials display many outstanding characteristics in terms of superconductivity, ferroelectricity, and high thermo-power [20]. Recently, there has been an increased interest in the lead halide−based perovskite−type crystals owing to their extraordinary optical properties. They are self-organized low-dimensional crystals. However, $CH_3NH_3PbI_3$ type perovskite and has been recognized as promising materials, having high carrier mobility and diffusion length indicating that these materials can be to design antennas. Despite the attractive properties of perovskites, controlling the physical properties during the design and fabrication phase is still quite challenging, which is currently a limitation in the realization of next-generation functional devices meant for high frequencies [21]. Moreover, various environmental factors including moisture, ultraviolet light exposure, and thermal stress play a key role in the instability of perovskite materials [18].

1.1 Identifying the problem

Low electron mobility in nonstructure in traditional metals such as copper, gold, and others causes significant channel attenuation and makes it difficult to implement a THz-frequency nano transmitter. Using a micrometer-sized metallic antenna to make wireless communication possible inside the nanosystem proved impossible to do.

1.2 Motivation

The military, healthcare, and sports monitoring are just a few of the many fields in which wearable antennas might be put to use. A total of 187.2 million wearable gadgets are estimated to be sold annually by 2022. All current applications demand a lightweight, low-cost, and flexible antenna profile for wearable antennas. Wireless body area network (WBAN) antenna design is more difficult than in free-space situations because of the skin's absorption in the network's human users. Traditional frequencies up to 60 GHz have been heavily used, limiting available bandwidth. THz-bandwidth is needed for major multi-gigabit or perhaps terabit wireless transmission capacity enhancements. A band between 0.1 THz and 10 THz, which is between the optical and microwave bands, gives the possibility of high data rates and high bandwidths. In addition, this kind of communication is less susceptible to weather conditions like rain and fog than free-space optical communication.

1.3 Aim

Industrial and scientific applications in security screening, sensing, material characterization, and astronomy might all benefit from THz waves. Through the use of novel materials and manufacturing processes, this PhD research intends to study and build low-loss THz waveguide structures for guided transmission, passive devices, and antennas. Printing antennas in the THz range are the focus of this research, which aims to simulate, fabricate, and test these devices. The tests will be done on PEN, PET, and polyimide, among other flexible substrates.

1.4 Main contributions

• This thesis proposes numerous THz antenna designs based on innovative 2DMs to address the issues related to metal skin depth effects in the THz band. Various 2DMs are verified and tested. As far as we know, this is one of the first studies to look at the potential usage of Perovskite and MoS2 materials in THz antenna design.
• Furthermore, creating an antenna array structure that includes components that can function in a broad frequency spectrum ranging from 0.75 THz to 1.1 THz, has a high gain, a low sidelobe level, and is flexible for wearable applications.
• Secondly, a unique hybrid design strategy is presented to combine the benefits of 2DMs with traditional metals, which solves several fabrication and measurement challenges in the THz range.
• Finally, this thesis develops a fabrication process for flexible substrates and 2DMs, including a dry etching technique that preserves the graphene material quality.

1.5 Thesis outline

The thesis is composed of seven chapters:

Chapter 1 Introduction include.
• General Background.
• Problem Statement.
• Research Motivation and Challenges.
• Research Objectives.
• Thesis Organization.

Chapter 2 The chapter introduces the 2DMs that will enable future wireless communications. The chapter discusses the properties and applications of 2DMs, as well as their growth and future opportunities in the field of THz applications. Discussion techniques and their evaluation in the most recent research need more attention in the area of wireless communication.

Chapter 3 Wearable THz antennas based on graphene have been developed and tested on three layers of human skin to meet the demands of contemporary THz systems. Because of the absorption of radiated energy, the antenna performance of wearable antennas will be reduced. We expect the antenna to work best at a distance of 1 or 2 millimetres from the surface of the human body. Due to human body proximity, antenna performance was impacted in terms of frequency detuning and radiation pattern distortion.

Chapter 4 Fabrication of PICA antenna arrays using Electron-Beam Lithography (EBL). A gold-based 1×4 PICA array operating in the THz frequency range of 0.75 to 1.1 THz is designed and fabricated. A simple and commonly available metal deposition technique to fabricate the structure is used. An ungrounded coplanar waveguide feeding line was used to excite the antenna. To the best of the authors knowledge, the proposed design is the first instance of the THz antenna for which the scattering response was measured. The design has achieved a measured 10 dB impedance bandwidth of 400 GHz at the centre frequency 0.925 THz. Results also show that other antenna performance characteristics, such as radiation efficiency and gain, are also high.

Chapter 5 THz antenna array for high-speed THz wireless communication fabrication using photolithography for on-wafer measurement.

Chapter 6 This chapter discusses future work as well as ideas for how to enhance the THz antenna devices for future applications.

Chapter 2

Background and literature review

2.1 THz applications

As the frequency spectrum is shifted higher, the free space attenuation and molecule absorption rise. Due to the fact that frequencies in the THz range are more susceptible to water vapour absorption, THz waves have a significant reflection loss. The scattering effect of transmitted waves gets more pronounced as it has short wavelengths, Fig 2.1.

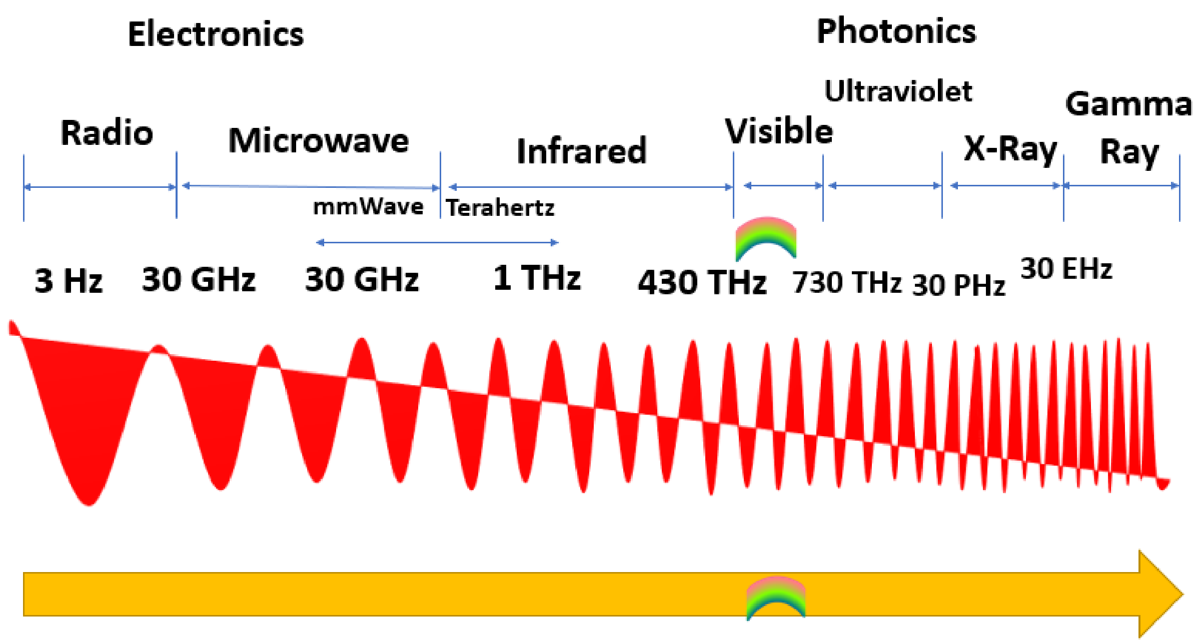

Figure 2.1: The electromagnetic spectrum

THz radiation can have high-resolution imaging—because THz signals have shorter wavelengths than microwaves, they can produce image with submillimeter resolution. Unlike ionising radiation, mmWave and THz radiation are nonionizing because the photon energy is insufficient (0.1 to 12.4 meV, more than three orders of magnitude weaker than ionising photon energy levels) to liberate an electron from an atom or molecule, whereas ionisation typically requires 12 eV [22] [23]. THz radiation has this feature, which makes it useful in biological and medical applications such as medical imaging for the identification of contaminated tissues. Low scattering, because THz signals have a longer wavelength than visible light, they disperse substantially less. Intensity, THz signals are far simpler to collimate and concentrate than radio waves [24] [25].

THz band is mostly between 0.1 THz and 10 THz in frequency, with data rates ranging from 10 to 160 Gbps with a transmission range of ten metres [23]. To boost spectral efficiency and data throughput in the THz band, new transceiver and physical layer designs are necessary. Additionally, Table 2.1 provides a full estimated comparison. This area of THz has been investi-

Technology	Frequency Ranges	Transmission Range	Peak Data Rate
Bluetooth Low Energy (BLE) [26]	2.4 GHz	100 m	1 Mbps
Low Power Wide Area Network (LoRaWAN) [27]	868 MHz, 0.9 Ghz, Sub 1 GHz	10 Km	50 Kbps
NarrowBand -Internet of Things (NB-IoT) [28]	0.7 to 0.9 GHz	10 Km	200 Kbps
Millimeter Wave (mmWave) Communication [29]	$\sim$ 24 to 100 GHz	100 meters	10 Gbps
THz Communication [30]	0.1 THz -10 THz	10 meters	10 Gbps to 160 Gbps

Table 2.1: Comparison between THz and other wireless technologies

gated only by a few researchers in a few domains, including chemical spectroscopy, astronomy, and solid-state physics. THz technology, on the other hand, is in high demand in a wide range of domains today, from fundamental research such as biochemical spectroscopy, astronomy, and materials science to applied sciences such as wireless communication, healthcare, agriculture, and security [3] [5]. THz technology has lately sparked considerable attention in academic and business. This is because there are a lot of interesting things about THz waves, like the fact that they can have bandwidths of tens or hundreds of GHz and that they do not pose much of a health risk [31].

Despite its advantages, THz communication does have a few disadvantages. In the THz range, the free space path loss is larger than at lower frequencies. This is the fundamental cause of the difference between received and transmitted power. The Friis transmission equation is

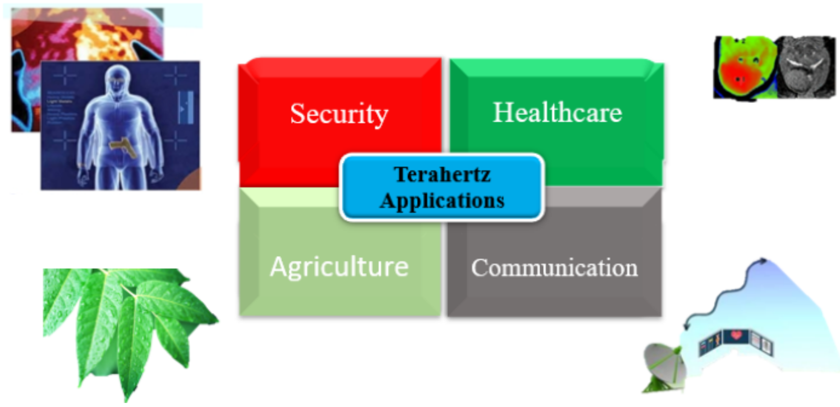

Figure 2.2: Various applications of THz radiation

used to compute the route loss in free space. [32].

$$\text{FSPL} = 20\log\left(\frac{4\pi d}{\lambda}\right)[\text{dB}] \quad (2.1)$$

where λ is the wavelength and d is the distance. The THz band, according to the Friis equation, has a higher propagation loss. Additionally, the THz signal is subject to both molecule absorption and propagation losses. Due to the loss of molecule absorption, multiple degrees of high attenuation are established [33]. The spreading loss in the THz frequency is 60 dB more than in the microwave range. Apart from the path loss features, the THz band's reflection properties are distinct from those of the microwave band [34] [35]. For devices in interior environments, surface differences are on the order of THz wavelength (several hundred microns). As a result, the indoor object surfaces are rough in the THz range. We know from the scattering effect that the reflection angle for a rough surface might vary from the incidence angle, and the reception antennas receive signals from various areas, resulting in multi-path scattering [36].

However, with the possibility of THz sources becoming more widely available, careful research into the biological and molecular effects of THz radiation on human health should be conducted [22], as even though THz is more than two orders of magnitude lower in frequency than ionising radiation, it would be prudent to know for certain that heating is the only health concern at THz. There will be a plethora of THz cameras, video cameras, and communication gadgets in the near future. THz technology will become more commonplace in our daily lives when these gadgets are small enough to be carried in our pockets or purses. Increasing the sensitivity of detection and the amount of electricity generated will become more crucial in order to accomplish this. Further advances in materials, device structure, operating principles, etc. are needed for the development. Nanotechnology, In the future, thz technology will play a key role in optimising the performance of THz technology.

2.2 2DMs for future THz wireless communication

An important advancement in developing materials and device design has been made at this frequency range. Despite the substantial progress in THz device work recently THz applications are still in the initial stages of development. As a result, numerous additional potential applications can be added to healthcare, short-range wireless communications, safety, food quality detection, spectroscopic analysis [37] [38] [39].

Functional materials are now considered as the fundamental building blocks for the realisation of THz devices [40]. In this regard, 2DMs such as hexagonal boron nitride (h-BN), transition metal dichalcogenides (TMD)s, graphene, and perovskites family have gained more consideration for THz applications [41]. 2DMs are characteristically described as single-layer materials that have become a central research point ever since the emergence of graphene. A particular crystal form and nuclear layer stacking sequence, particularly in TMDs, can result in vastly different physical properties such as superconductors, metal, insulator, and semiconductor [42]. The family of 2DMs shows a widespread series of novel mechanical and electrical properties, for instance thermal stability, bandgap tunability, and high conductivity [43]. Moreover, in stark contrast with their bulk counterparts, one of the fascinating features of 2DMs is the ultra-high specific surface areas that enable their energy construction vulnerable to voltage biasing [44]. However, there are numerous other 2DMs that remain undiscovered. Furthermore, combining different 2DMs results in new structures with unique physical and concoction properties [45].

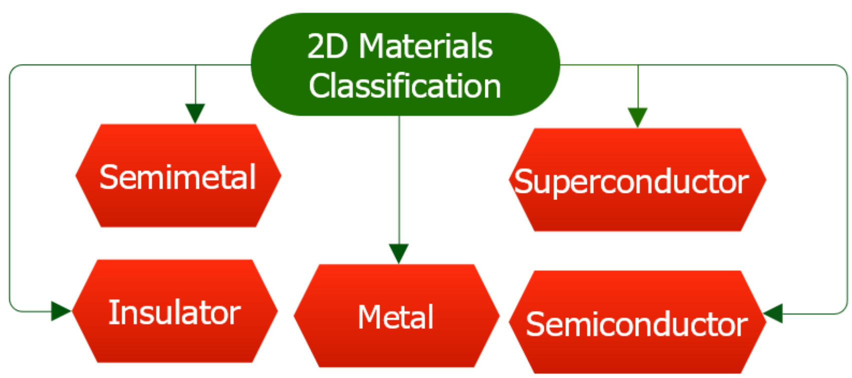

Figure 2.3: 2DMs family.

2DMs also enable the development of sensing systems that can be tuned through the electronic band structure by controlling their thickness and amount of dopants, alloying between various materials [46]. Metals, such as gold and copper regularly show SPP in the optical frequency range, but have vastly different physical properties in the THz band effecting their performance [47] [48] [49]. As the THz resonance is far beneath the aforementioned metals plasma frequencies, these materials have high conductivity which causes them to behave as a perfect electric conductor (PEC) to a more prominent degree [47]. In this manner, the SPP's electric field just enters the metal, showing poor repression, accordingly, losing a lot of points of interest [50].

Additional line of research pries the field wide open as the exploration of new functional 2DMs and experimentally accessible 2DMs grow at a rapid pace, such a diverse family encompasses a large variety of material properties including insulators, semiconductors, semimetals, and metals as shown in Fig 2.3. An exciting aspect of 2DMs is to get benefit of the greatly unique properties of and load them into a configuration to make new THz devices created from ultra-thin elements [51]. Every 2DM identified or to be realized might consequently offer a new application for THz waves [52] [53] [54] [55].

2.3 2DMs electronic properties

In the scope of 0.1 THz to 1 THz frequency range, the wavelength ranges from 10^8 to 10^5 nm, which is exceptionally short [56]. The skin depth is a convenient method to identify the radius of a metal in which the majority of the current is flowing. It is unnecessary to use a wire with a radius that is considerably greater than the skin depth since the current moves in the skin-depth area regardless of the conductor size [57], [56], [57]. Due to its unique structural and physical properties (Fig 2.5 (a), h-BN is considered a potential assistance material for improving the electrical and optoelectronic performance of other 2DMs [58], [59]. Furthermore, graphene/h-BN heterostructure offers a platform for researching many-body correlation phenomena of Dirac fermions, such as the fractional quantum Hall effect in the high magnetic field of graphene [60] [61]. h-BN has also been discovered to be useful in other areas [61], [62], including carrier tunnelling and deep ultraviolet optoelectronics [63].

2.3.1 THz graphene plasmonics

Because of the skin depth effect, the surface resistivity of typical conductors rises with frequency for conventional metals, and so the radiation efficiency of nano-radius antennas is relatively poor owing to substantial ohmic losses at very tiny scales. [56], [64]. As a result, it is probable that the 2DMs will surpass traditional metal-based antennas in terms of radiation efficiency. [65].

SPPs are electromagnetic waves that propagate along the surface of a conductor [66]. These waves produced in the structure of collective oscillations of electrons allow the sequestration and management of electromagnetic power at sub wavelength scales [67].

Graphene supports the propagation of SPPs that are with no substantial loss, and more importantly, it exhibits the excellent property of being tunable through electrical/magnetic bias or synthetic doping [13] [68]. Zero-bias thermoelectric photodetectors based on a single graphene sheet produced by chemical vapour deposition were used to tune throughout the whole THz range from 0.1 to 10 THz (CVD) [69]. Biased graphene with dielectric constants of ε_1 and ε_2

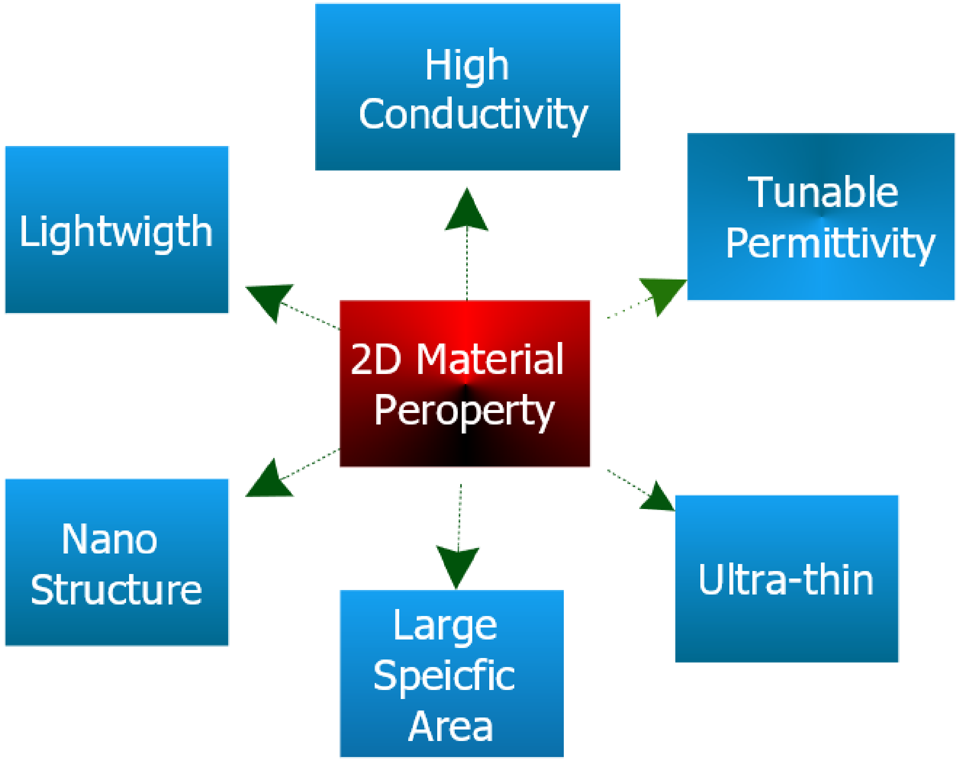

Figure 2.4: 2DMs Property

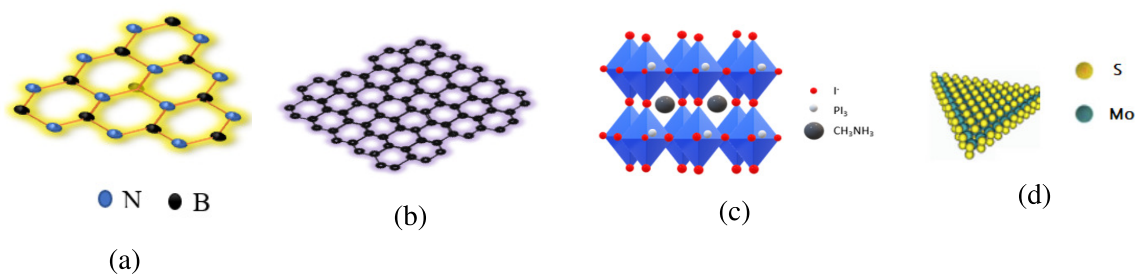

Figure 2.5: The 2DM structure: (a) hexagonal boron nitride (h-BN) (b) Graphene (c) Perovskite $CH_3NH_3PbI_3$ (d) Molybdenum disulphide (MoS_2).

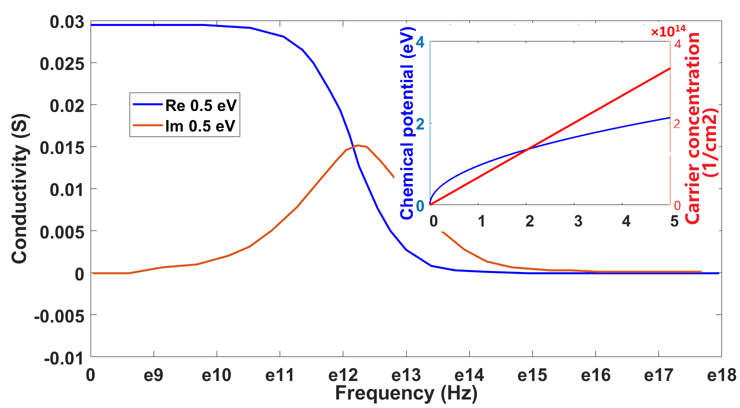

Figure 2.6: Real and imaginary conductivity of graphene.

and the collective oscillations in graphene are stirred up by electromagnetic waves of transverse magnetic approach, the dispersion described as [70].

$$k_{spp} = \varepsilon_0 \frac{\varepsilon_1 + \varepsilon_2}{2} \frac{2i\omega}{\sigma(\omega, q)} \tag{2.2}$$

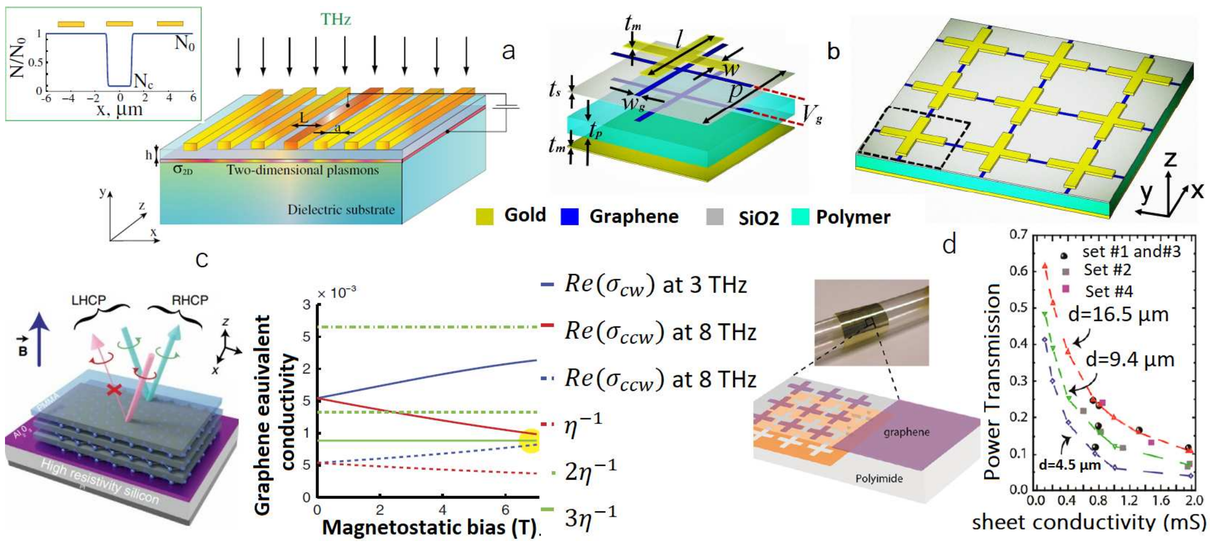

Figure 2.7: Graphene-based THz devices and THz graphene plasmonics. (a) A split grating gate field effect transistor [71]. (b) Diagram of graphene plasmon nonlinear absorption [72]. (C) Metamaterial modulator made of graphene [73]. The top of the polyimide substrate is covered with nonpatterned and patterned graphene layers. (d) A diagram of the graphene metamaterial absorber's structure in [74].

Where k_{spp} is a complex, the real part is the corresponding to the plasmonic wave, and the imaginary part is the decay. Where plasmonic wave can be accomplished in the far infrared as the large imaginary conductivity and small Ohmic loss in the real part. However, in the infrared frequency region, the plasmonic wavelengths can increase to 100. The plasmons on graphene can be manipulated by optical pumping, doping, and electrostatic gating. Graphene's conductivity can be modeled in the THz band using [75],

$$\sigma_0 = \frac{e^2 k_B T \tau}{\pi h^2} \left\{ \frac{\mu_c}{k_B T} + 2\ln\left(e^{-\mu_c/k_B T} + 1\right) \right\} \tag{2.3}$$

Where the scattering time is τ, the Boltzmann constant is kB, the electron charge is e, the temperature is T, the Planck constant is h, the angular frequency is ω, and the chemical potential is μ_c. The conductivity of graphene regulates its reactivity using a chemical potential and relaxation time that can be calculated by, [14],

$$\mu_c = h v_f \sqrt{\pi n} \tag{2.4}$$

$$\tau = \frac{\mu_c \mu}{e v_f^2} \tag{2.5}$$

where v_f is the Fermi velocity $\left(10^6 \text{ s/m}\right)$, n is the carrier density and μ is the carrier mobility of the electrons. Frequency changing and a wide bandwidth can be accomplished by changing the chemical potential and scattering time. However, increasing chemical potential affects the radiation from graphene as the absorption level will increase. An important characteristic of the graphene band structure is that under zero doping conditions the chemical potential remains along with the Dirac point and thus there are only a few available free electrons. Any change in position of the chemical potential, μ, can have drastic consequences on the free carrier density of the system. In extremely low μ and carrier mobility, invalid force reactions are found. This suggests that reverberation is not achieved due to the attenuation of SPPs as they spread on the graphene surface. Even though the rise of the μ and the carrier mobility support the radiated energy, they have their effect on the impulse response. However, the increase in the μ and the carrier mobility affects the width of the response (bandwidth) [76].

It has been emphasized the relevance of intraband and interband contributions to surface wave propagation [77]. The intraband conductivity can be adjusted by modifying the chemical potential at infrared frequencies, allowing for certain control over surface wave characteristics. According to [78], a transverse electromagnetic mode may be adjusted from radio to infrared by altering the density of charge carriers in graphene through a gate voltage.

Plasmonic in graphene with many more attractive properties like high carrier mobility, low gate voltage, and nanostructure shows an excellent capability for THz resonant devices operating in the THz frequency range. The Electric field effect variation of electron density and generate periodic plasmonic lattices with a defect cavity introduced in [71]. In addition, deeply pumped cavity plasmon types are excited in a periodic plasmonic lattice by an incident THz radiation causing a deep subwavelength concentration of THz energy (Fig 2.7(a)). A great field enhancement of two orders of magnitude is better than the value in conventional metals at THz. Another important feature of graphene is that graphene can be used in creating tunable THz devices. A cross-shaped metamaterial containing a two-layer of graphene was designed for accomplishing a tunable polarization absorber, as shown in Fig.2.7 (b). The absorption was performed with the highest frequency tuning range of 15%. The peak absorption has been determined by regulating the Fermi energy which can be accomplished by changing the bias voltage. The device can turn the reflected wave through a linear polarization of the tunable azimuth angle from 0° to 90° at the operating frequency [72].

A THz nonreciprocal isolator with circular polarization based on biased graphene has been introduced in [73]. The isolator displays nearly 20 dB isolation and 7.5 dB insertion loss at 2.9 THz (Fig. 2.7 (c)). The hybrid graphene metamaterial paves the way for actively manipulating the mutual interaction of THz waves and matter at the deep subwavelength scale and enabling a variety of THz applications such as tunable memory devices and modulators [74] (Fig. 2.7 (d)). Another sort of THz modulator has been developed, which utilises a frequency selective surface to resonantly boost graphene's THz response.

2.3.2 Perovskite and MoS2 THz properties

Perovskites have been extensively examined in the field of THz application given their appealing properties [79] [80], however, perovskite application is usually limited to photovoltaic and solar domains. The properties of perovskite family materials have allowed the development of many novel devices and applications. Perovskite materials reveal several exceptional physical characteristics such as ferroelectricity, superconductivity, and high thermopower [20]. Perovskite were discovered by Weber in 1978 [81]. However, $CH_3NH_3PbI_3$ perovskite has been recognized as promising material due to its high charge carrier mobility, and diffusion length indicating that this material could be a potential candidate for THz application (Fig 2.5 (c). Therefore, lead iodide perovskite precursor solution can be made by combining the CH_3NH_3I and PbI2 at 151 molar ratios to meet the atom ratio in $CH_3NH_3PbI_3$ [82]. This material could have a potentional high efficiency in THz frequency [83]. The complex photoconductivity $\Delta\tilde{\sigma}(w,\tau)$ is the sum of Drude and Smith conductivities in the Drude-Smith model [84] [85].

$$\Delta\tilde{\sigma}(\omega,\tau) = \frac{\varepsilon_0 \omega_p^2}{\Gamma - i\omega}\left[1 + \frac{c_1}{1 - i\frac{w}{\Gamma}}\right] \tag{2.6}$$

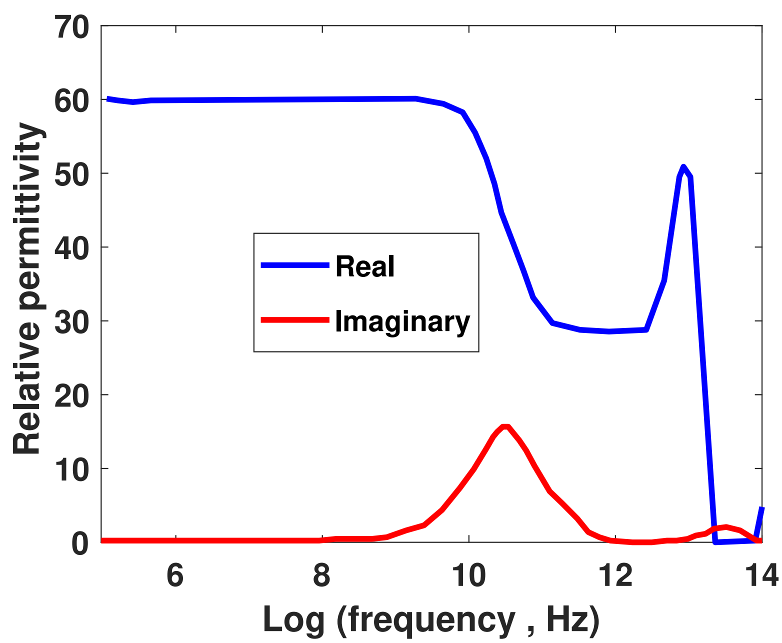

Figure 2.8: Permittivity and conductivity of $CH_3NH_3PbI_3$ perovskite (Ref [82])

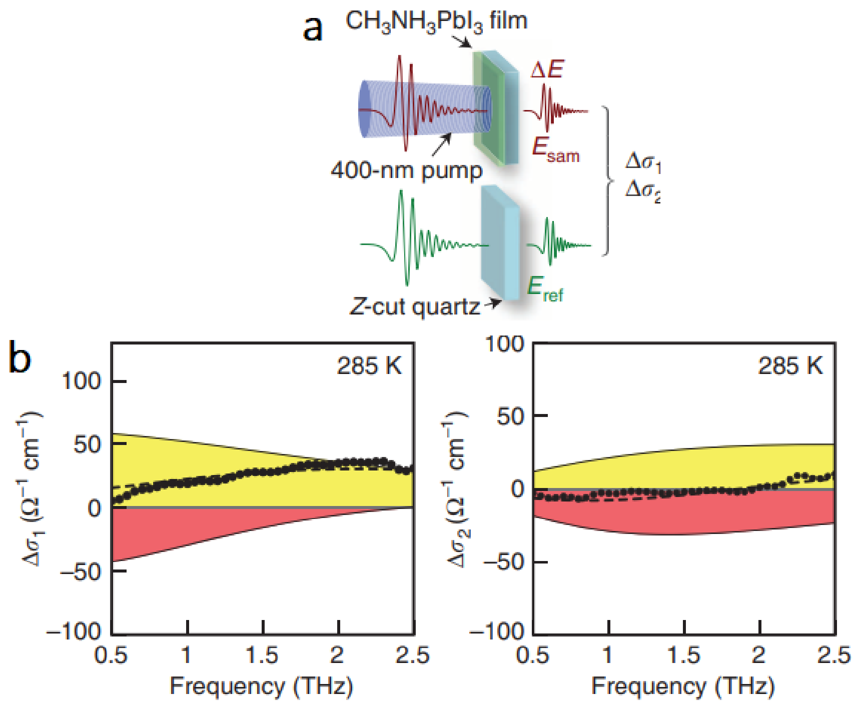

Figure 2.9: (a) THz transient of the $CH_3NH_3PbI_3$ thin film after optical excitation with 400 nm pump pulses with a fluence of 27 μcm^{-2}. The Smith term arises from the sample disorder and contributes both a downturn in $\Delta\sigma_1$ and a negative $\Delta\sigma_2$ at the lowest frequencies [84].

Where the first term $\Delta\tilde{\sigma}_{(\omega\cdot\sigma)} = \varepsilon_0 w_P^2/(\Gamma - i\omega)$ is the Drude conductivity. The second Smith term $C_1\Delta\widetilde{\sigma_D}/(1-i\omega/\Gamma)$.

Figures 2.8 show the permittivity and conductivity of at 300 K for $CH_3NH_3PbI_3$. At low frequencies, the dielectric constant is large; it has been reported to be 60.9 over the 20 Hz – 1MHz range, which is consistent with the low frequency value of 60 obtained from fits at higher frequencies. This low-frequency value is appropriate in determining steady-state properties, with static fields consequently varying slowly with position five times slower than in silicon under similar electrostatic disturbances. At infrared frequencies, the ionic component drops out, leaving only the electronic response. The dielectric constant drops to 6.5 at optical frequencies, lower than that of inorganic semiconductors with a similar bandgap [86]. The other possibility is that $CH_3NH_3PbI_3$ may possess paraelectric or even ferroelectric properties at room temperature and above [82].

Coating the perovskite material on a wafer allows the modulation of THz band at 50 GHz modulating speed. Therefore, the ultrafast response opens the excellent potential in flexible photonics, wavefront control, and short-range wireless THz communication applications [80] [87] [88].

However, it is very difficult to produce a dynamic response in flexible photonic gadgets. In [90] experimentally prove that the solution of perovskite with an intrinsic ultrafast response could be an ideal platform for developing active flexible photonic devices. A novel silicon-

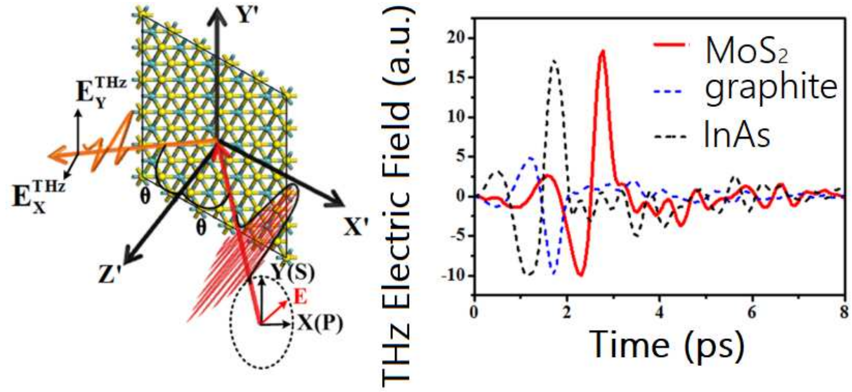

Figure 2.10: (a) THz radiation in reflection configuration. XYZ and $X'Y'Z'$ represent the laboratory and crystal coordinate, respectively. Generated THz pulses in (b) time and domain from layered MoS2 (red solid curve), graphite (blue dash curve), and InAs crystal (black dash curve) [89].

contained THz metallic split-ring metamaterial is proposed in [91]. The Fano resonance and transmission can be controlled through external biasing. Fano resonance and transmission amplitude abate drastically with the rise of current bias. As the current bias is increased, both the thickness and conductivity of the silicon carrier layer are modulated simultaneously.

Transition metal dichalcogenides (TMDs) consist of transition metal atoms covalently bonded to chalcogens (S, Se, or Te) to form atomic trilayers [92]. Although TMDs are appropriate for innovative THz devices, their performance in the THz range has only been studied in a few papers in the literature [93] [94] [95]. Molybdenum disulfide (MoS_2) is already showing promise for use in electronic and photonic devices [96] [97] [98] [99]. The lattice and band structures of monolayer MoS2 are shown Fig 2.5 d. MoS_2 belongs to the family of 2D layered TMDs [100] [101]. Ultrafast carrier dynamics in monolayer and trilayer MoS2 and WSe2 were observed using time-resolved photoluminescence and THz spectroscopy [102]. The ultrafast reaction time of photoconductivity and photoluminescence in the monolayer MoS2 is 350 fs, while it is 1 ps in the trilayer MoS2 and monolayer WSe2. These findings demonstrate the enormous potential of these materials for use in high-speed THz devices [7]. Recently, a monolayer of MoS_2, such as monolayer MoS_2 nanostructure, have become potential materials of SPPs due to direct bandgap and strong spin-obit couplings, which can effectively reduce losses of SPPs. Moreover, MoS_2 nanostructure exhibits excellent photoelectric properties and has been suggested to be used in field effect transistors [47].

Measurement of ultrafast charge carrier dynamics in monolayers and trilayers of TMDs (MoS_2) and WSe_2 using a combination of time-resolved photoluminescence and THz spectroscopy showed the possibility of TMDs as high-speed optoelectronic [102]. MoS_2 can produce THz radiation with a linearly polarized femtosecond laser [89]. The radiated THz amplitude of MoS_2 has a linear dependence on ever-increasing pump fluence and thus quadratic with the pump electric field.

Table 2.2: THz uses of two-dimensional materials: graphene and beyond

Material	**Fundamental properties**	**Frequency of operation**	**Usage in THz wireless communication**
Graphene	Surface plasmon propagation. Ultra-thin Flexibility	0.1 to 10 THz	Antenna [103] [104], absorption [105], metasurface [106], detection [107], and modulation [108]
Mos2	SPP, high conductivity, Ultra-thin	0.1 to 10 THz	Modulation [109] [47], Enhanced THz emission [110], and tunable THz broadband absorber [111]
Perovskite	Ferroelectricity, Superconductivity	0.1 to 10 THz	Antenna [112]
, Modulation [113] [114]			
h-BN	Tunnelling and deep ultraviolet optoelectronics	0.1 to 10 THz	used in conjunction with other 2DMs to improve performance [115] [58] [59]

Controlling the propagation of THz waves is very important in THz technologies, practically in high-speed communication. An optically tunable THz modulator using multilayer-MoS_2 and a silicon substrate are presented in [116]. The modulator shows higher modulation efficiency than the graphene modulator. An alternative mechanism for modulating the emission from a quantum-cascade laser (QCL) device in which optically generated acoustic phonon pulses are used to perturb the QCL band structure, enabling fast amplitude modulation that can be controlled using the QCL drive current or strain pulse amplitude, up to a modulation depth of 6% [117].

In [118] design based on MoS_2, the mid-infrared to THz can be realized. A MoS_2 layer between 200 nm diameter gold nanoparticle (AuNP) and 150 nm gold film is enhanced by more than four times compared with the bare MoS_2 sample. The implications of these atomic-scale hybrid materials could be revolutionary for THz applications. The potential THz applications of 2DMs, Graphene and beyond are shown in Table 2.2.

2.4 2DMs THz application

With the fast advancement of graphene and other 2DMs, it is possible to increase the 2DMs' THz responsiveness and regulate THz waves. Many THz devices can be made because of the large variety of material characteristics and the ability to combine 2DMs in a hybrid construction. In Fig. 2.11 (a), Hybrid silicon-perovskite structures are proposed for optically controlled THz wave switching between 0.2 and 2 THz. The THz amplitude modulation was controlled by using a 532 nm external laser to generate free carriers. Perovskite and silicon in a one-step manufacturing technique showed excellent stability and modulation efficiency. With this configuration, a THz switch could be achievable [113]. The progress on 2DMs such as graphene

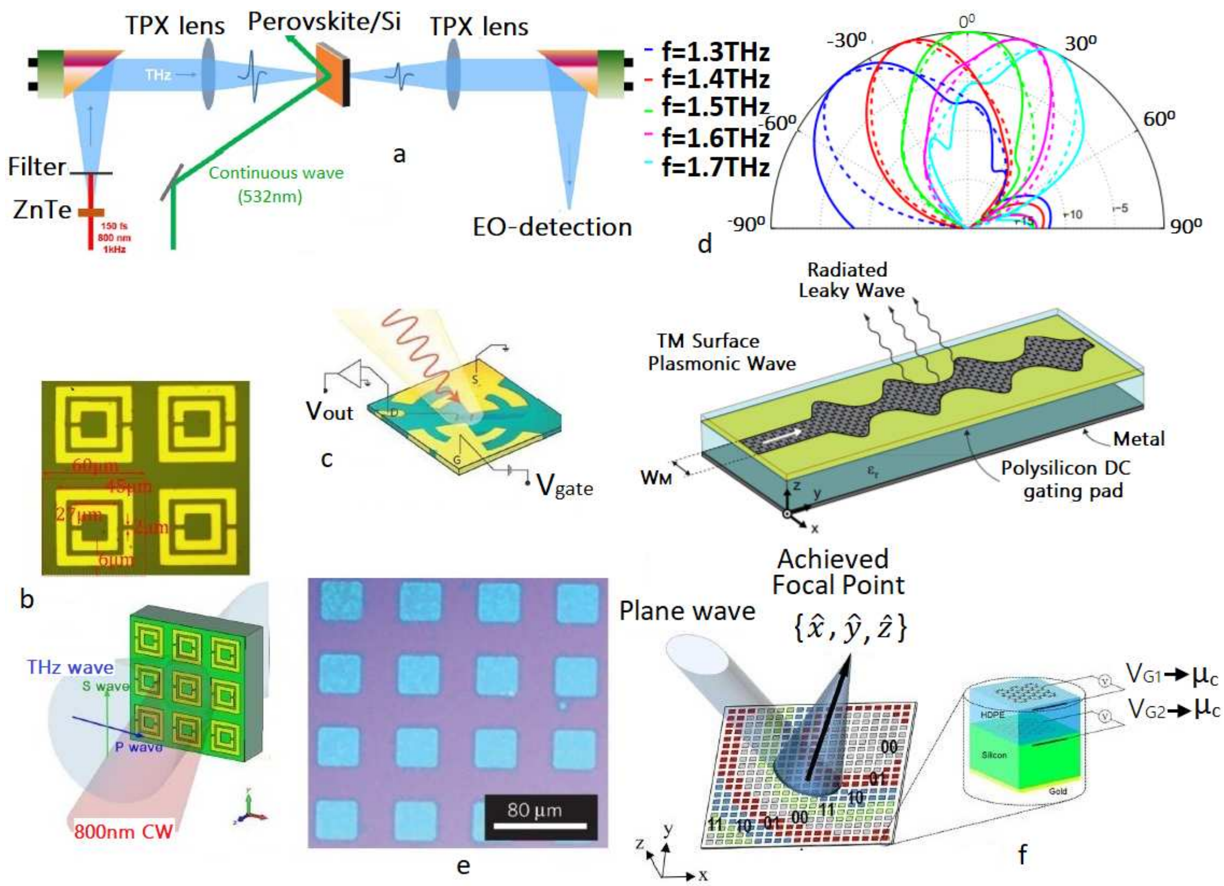

Figure 2.11: THz devices based on 2DMs. (a) Schematic of optically controllable THz modulation using perovskite and silicon [113]. (b) A MoS2 metasurface [109] (c) A three-dimensional model of Graphene field-effect transistors as room-temperature THz detectors [107]. (d) A non-reciprocal leaky-wave antenna based on a spatiotemporally variable surface impedance made of graphene [107]. (e) A $MoS2$ growth in a CVD process as seen in an optical microscope [119]. (f) A flat mirror coding metasurface with adjustable focus [106].

and MoS_2 materials offers a different research idea for THz modulator, an optically pumped THz modulator based on a MoS_2 and silicon meta surface are fabricated in [109]. It has been shown that graphene can be utilised to actively manipulate the waveguide characteristics. A simple straight waveguide coated with graphene can combine the comparatively low loss of silicon waveguides with the ultra-rapid tuning of graphene electromagnetic characteristics at THz frequencies [120]. The THz wave modulation based on MoS_2 metasurface has been demonstrated experimentally using time-domain spectroscopy and, which can reach over 90% under

the incident wave laser pumping of 4 W/cm^2 power density. A metasurface of the construction of the double split ring resonator is shown in Fig 2.11 b.
The metallic metal surface structure's resonances divide the modulation spectrum into a number of different frequency windows. By manipulating the geometric structure of the meta surface and incident polarisation, the modulation spectrum's frequency, position, and bandwidth may be altered. In terms of wireless communication, graphene has extraordinary potential for short-range THz wireless communication. This feature enables the use of THz wireless technology in integrated systems where conventional metals are incompatible. It was shown that the graphene electrical field effect may be used to efficiently tune the antenna's frequency. The suggested strategy and approaches are critical for addressing the contemporary and basic challenges of excitation detection. In Fig 2.11 (d), based on the periodic modulation of a graphene strip, researchers have converted plasmons to free space waves. Analyze the dispersion, forecast the connection efficiency and emitted field, and build strip structures capable of meeting precise coupling requirements [108]. In [107] (Fig 2.11 (c)), the study illustrates THz detectors based on antenna-coupled graphene field effect transistors. These use the nonlinear response of the gate to the radiation field, with thermoelectric and photoconductive origins, to enable large-area, rapid imaging of macroscopical materials.

Figure 2.11 b (e), a straightforward method to grow large-area MoS_2MoS2 films with controlled nucleation and promote the formation of large-area films formed by monolayer or few layers. In [119] used patterned substrates with the distribution of SiO_2 pillars for MoS_2 growth in the chemical vapour deposition (CVD) process.

The small loss in graphene plasmons at THz band is the main motivation for developing several waves tuneable devices. A flat reflective which can be programmed to concentration THz waves to a certain point in the near field is proposed in [106] Fig 2.11 (f). The reprogramming capability of the meta-mirror could be a key to improve compact THz scanning and imaging and novel reconfigurable component THz wireless communications. The device is conceived as a 2-bit coding metasurface that leverages the tunability of its graphene-based unit cells to control both the position and depth of focus.

Anisotropic optoelectronic devices have appeared as a desirable and attractive exploration subject owing to the latest developments in photonics technology involving communication and sensing. This is shown by a number of recent studies in photonics and optoelectronics, from solar cells and light-emitting devices to touch screens and photodetectors. 2DMs also cause ultrafast lasers to be on the rise. [123]. Figure 2.12. (a), illustrates a framework for ultrasensitive and THz modulation of an efficient metamaterial device by creating an anisotropic perovskite-hybridized resonator array. [114]. A periodic array of closed-ring and split-ring resonators (CRRs and SRRs) is used to customise the plasmon-induced transparency (PIT) resonance at

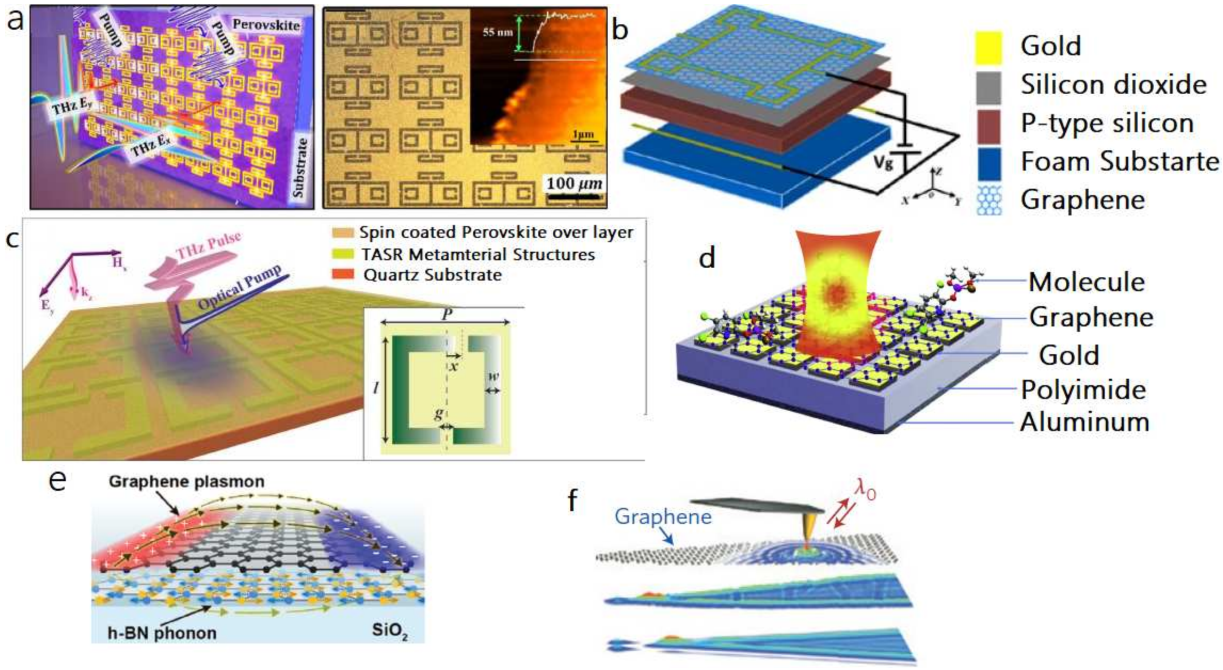

Figure 2.12: (a) Schematic diagram of the polarization-dependent metamaterial perovskite THz device. [114]. (b) An active frequency selective surface for angle beam steering based on a hybrid graphene-gold structure [121]. (c) The perovskite-coated hybrid metadevice is shown in an artistic manner, with the 2D perovskite spin-coated (thickness 60 nm) on top of THz asymmetric split ring (TASR) and photoexcited using a 400-nm optical pump beam with THz as the probe. [80]. (d) Optical microscope images of the constructed planar TASR metamaterial structure [105]. (e) H-BN monolayer sheet is used to construct graphene nanoresonators on Si wafer [115]. (f) Experimentation using a scanning near-field optical microscope tip to initiate plasmon-polariton waves in a graphene wedge [122].

different frequencies determined by incident polarizations. On the quartz wafer, a thin layer of perovskite is deposited, which acts as a photoactive layer when irradiated with 400 nm optical pump pulses. Photo-swapping of Fano resonance-based subwavelength metamaterial devices at THz band may be enabled by using a hybrid lead halide perovskite solution as an active material. In [80] (Fig. 2.12 C), Lead halide perovskites are employed to determine a hybrid perovskite metamaterial device that exploits power photo switching of the metamaterial resonances in the THz band. In terms of antennas, much research has been undertaken to optimise the installation of THz antennas within environmental constraints. At THz frequencies, however, attaining significant angle steering for reconfigurable antennas remains a challenge. In [121] Fig. 2.12(b), the use of a gold and graphene-based construction to steer a 360-degree beam-steering THz antenna is discussed. With its adjustable beam direction and strength level, this antenna might be used for reconfigurable short-range THz wireless communication.

Measurements of nanoresonators, which allow for hybridization with the phonons of the atomically thin h-BN layer to create two clearly separated new surface phonon plasmon-polariton (SPPP) modes with widths ranging from 30 to 300 nm, provide the electromagnetically coupled graphene plasmon/h-BN phonon mode frequency wavevector dispersion relations. in Fig.

2.12 (e). More studies into graphene plasmon-induced single-molecule excitation will benefit from the discovery that graphene nanoresonators may be utilised as extraordinarily sensitive probes. [115].

In [105], integrated monolayer graphene on a metamaterial absorber cavity in which sensing targets induce a considerable shift in metamaterial resonant absorption or reflection owing to their high interaction with graphene. (Fig. 2.12 (d)). Scannable near-field optical microscopy tips are another new method for igniting graphene plasmons, Fig. 2.12 (f). A THz metamaterial absorber cavity integrates monolayer graphene, where the strong interaction between graphene and the sensing targets results in a substantial shift in metamaterial resonant absorption (or reflection). Graphene plasmon polaritons are excited when an infrared beam shines on a nanoscale metallic tip. The tip provides the extra momentum needed for this process. Reflections at the graphene edges cause standing-wave patterns. [122].

THz communication literature is mostly focused on device technology. However, there is still a limited amount of research on the communication components required to construct THz communication networks with a high bandwidth. Each scenario has its own set of difficulties. Metal THz antennas encounter a number of challenges, ranging from microfabrication to nanoscale electromagnetic interaction. Two-dimensional materials are showing promise as THz wireless device materials. Similarly, unique THz signal modulation devices based on upcoming technologies such as graphene have been proposed for use in short-range indoor communication. At THz frequencies, the key difficulty is getting efficient sources. Even with significant air attenuation, QCL may be a viable THz source of communication in the upper THz range. According to the several ways reported in the literature for obtaining THz sources. Recent developments in two-dimensional material (2DM) processing and fabrication points to a bright future towards the realisation of efficient THz sensing devices. This is, without doubt, the most critical component of an adequate THz technology for applications in future wireless communication systems.

In this paper, we have reviewed various types of material properties in the THz band, and some of them can provide high conductivity, which is required in THz wireless communications. Reviewing recent work on 2DMs reveals that improved methods in terms of fabrication and measurement are required. 2DMs have a lot of advantages, including lightweight, flexibility, electrical characteristics, and environmental friendliness. 2DM can be ideal with THz wearable devices. On the contrary, a fundamental disadvantage of 2DMs is their high absorption. Finally, it is concluded that the current technology needs to be further developed in the years to come and many problems related to the THz communication system need to be solved.

2.5 Summary

A new generation of wireless communication is possible because of the fast development of 2DMs in recent years. The 2DMs family exhibits a broad range of unique mechanical and electrical characteristics, such as thermal stability, bandgap tunability, and high conductivity, among other features. In addition, the ultra-high specific surface areas of 2DMs, in sharp contrast to their bulk counterparts, make their energy architecture sensitive to voltage biassing. Light–matter interactions can be dynamically controlled thanks to graphene's exceptional electrical and optical characteristics in the THz range. A lot more research into the potential of TMDs and perovskites for THz applications is expected to lead to the discovery of numerous new and exciting THz phenomena and high-performance THz devices that are not yet possible with conventional technology. Both materials may be used to create THz modulators, detectors, polarizers, and absorbers. There are, however, a large number of 2DMs that have yet to be found. However, countless other 2DMs remain unknown. Additionally, mixing several 2DMs resulted in the formation of novel structures with distinct physical and concoction characteristics. Two-dimensional nanostructures are projected to be extremely compatible with existing microfabrication processes and to be readily integrated into metamaterials in the future. It should be mentioned that the active study and development of 2DMs are still in their early stage.

Chapter 3

THz graphene Antenna for wearable application

3.1 Graphene band structure

It has been discovered that graphene has various idiographic physical phenomena due to its unique electronic features, such as its zero bandgap, Dirac fermions behaviour of its electrons, and low density of states, which are all due to its unique electronic qualities.

It is clear that the six points at the corners of the First Brillouin Zone FBZ fall into two groups of three which are equivalent, so we need consider only two equivalent corners that labeled as K and K^l in the Fig 3.1. The two spots k and k ' in the corners of the graphene Brillouin zone,

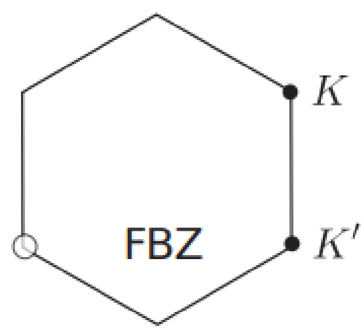

Figure 3.1: First Brillouin zone (inner hexagon)

which are of special significance for the physics of graphene, are k and $k'(BZ)$. Their locations in the space of momentum are given by,

$$K = \frac{2\pi}{3a}\left(1, \frac{1}{\sqrt{3}}\right), \qquad K' = \frac{2\pi}{3a}\left(1, -\frac{1}{\sqrt{3}}\right) \tag{3.1}$$

In the tight binding method, the band structure of graphene is represented as a triangular lattice with two atoms per unit cell on the basis of the number of atoms in the cell. The following is the representation of the derived energy band structure.

$$E\pm(k) = t\sqrt{3+f(k)} - t'f(k) \tag{3.2}$$

Where the plus sign applies to the upper π^* and the minus sign the lower π band. It is clear from Eq. 3.2 that the spectrum is symmetric around zero energy if $t' = 0$. For finite values of t' the electron-hole symmetry is broken and the π and π^* bands become asymmetric.

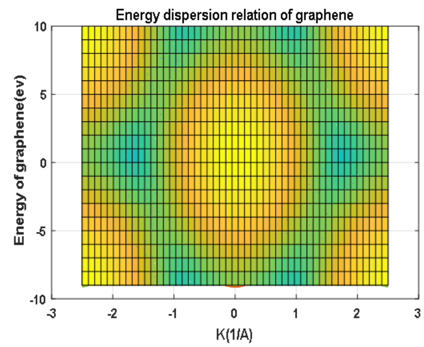

(a)

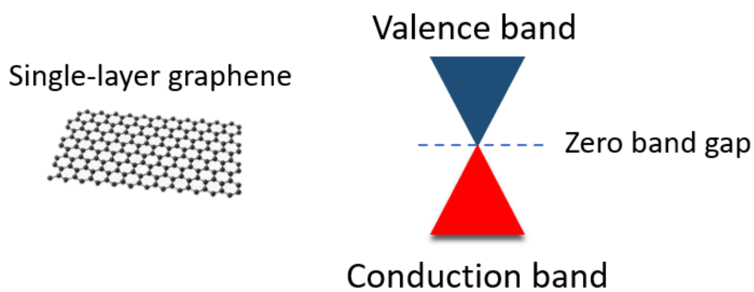

(b)

Figure 3.2: (a) 3D band structure of graphene. (b) 2D electronic band structure of graphene

3.2 Surface plasmons

Copper material is a well-known material for radio frequency (RF) and microwave antenna design. Metal antenna design has been extensively investigated in the RF and microwave frequency bands, and systematic antenna design methodologies exist. However, the copper metal antenna used in the THz band is designed totally differently from a conventional microwave metal antenna. While conventional microwave metal antennas are stimulated using a variety of feed lines including microstrip, coaxial cable, and CPW, THz antennas are excited via fibre or air. Another distinction between metal THz and microwave antennas is the bias voltage. While the THz antenna design requires bias voltage, microwave antennas need not. Additionally, the metal THz antenna is more costly and hard to fabricate than a metal microwave antenna.

Plasmonics is analogous to electronics in that it makes use of plasmons. A plasmon is a quantum in physics that describes the collective excitation of free electrons in materials. Due to the nature of the dielectric-metal interface between the medium and the particles, plasmonic nanoparticles have an electron density that can couple with electromagnetic (EM) radiation with wavelengths greater than the particle. The plasmomics idea dates all the way back to the 1950s, when researchers Ritchie, Kretschmann, and Otto [124] [125] reported their results on light incident on dielectric and metallic surfaces. demonstrates the existence of SPs at the interface between a metal ($\varepsilon < 0$) and a dielectric medium ($\varepsilon > 0$).

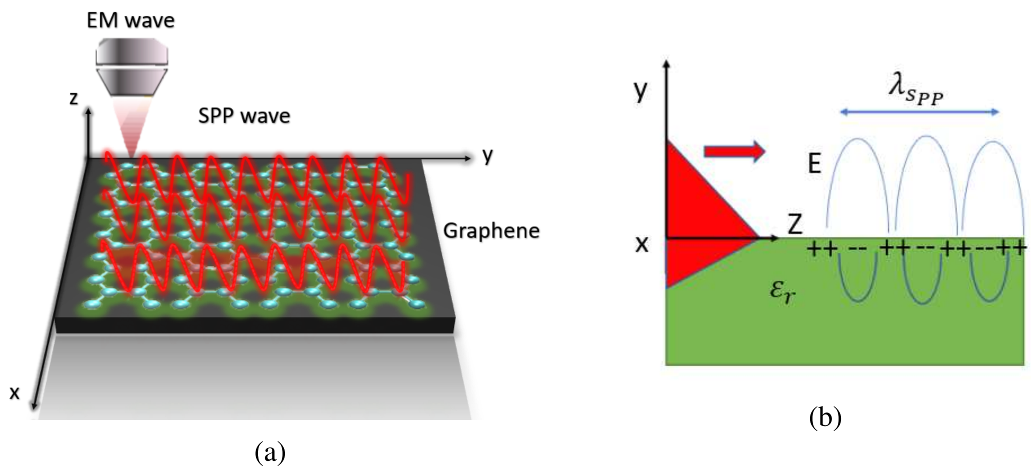

Figure 3.3: (a) and (b) schematics of the electromagnetic field of surface plasmons propagating along the interface between a metal and dielectric.

However, at the interface between a metal and a dielectric, precise matching conditions exist for the electron wave to oscillate and couple with light [126]. This mode is referred to as surface plasmons (SPs) or surface plasmon polaritons (SPPs), and it originates at the metal surface and propagates along the metal-dielectric contact. When SPs are activated, an electric field in the z-direction is amplified, resulting in an unusually high sensitivity for interfacial characterizations [127]. As a result, novel optics that exploit this resonance property have garnered interest in a variety of sectors. Successfully marketed sruface plasmon resonance (SPR) immunosensors give both qualitative and quantitative information. These phenomena may manifest themselves in a variety of ways, from freely propagating electron density waves over metal surfaces to localised electron oscillations on metal nanoparticles. Their unique properties allow a diverse variety of applications, including nanoscale manipulation, single-molecule detection of biological analytes, and amplification of molecular resonances [128] [129].

3.3 Chemical potential and relaxation time

Graphene presents excellent conditions for the propagation of SPP, electromagnetic waves guided along a metal-dielectric interface which are generated by an incident high-frequency radiation. Indeed, a free-standing graphene layer supports transverse magnetic. SPP waves with an effective mode index $n_{\text{eff given by}}$ [75].

$$n_{\text{eff}}(\omega) = \sqrt{1 - 4\frac{\mu_0}{\varepsilon_0}\frac{1}{\sigma(\omega)^2}} \tag{3.3}$$

Once the graphene conductivity has been calculated,the propagation of SPP waves in graphene can be studied. Indeed, in graphene, the edge of the graphene patch act as a mirror and the graphene behaves as a resonator for SPP modes. The coupling of the incident electromagnetic radiation with the corresponding SPP modes leads to resonances in the graphene. The resonance condition is given by [76].

$$m\frac{1}{2}\frac{\lambda}{n_{\text{eff}}} = L + 2(\delta)L \tag{3.4}$$

Where m is an integer determining the order of the resonance, λ is the wavelength of the incident radiation, L is the graphene length and δL is a measure of the field penetration outside the graphene. This equation determines a set of m resonance frequencies ω_m corresponding to m modes of the resonator. The experimentally obtained values of the relaxation time are significantly lower than the minimum required values indicated by the simulation results. Therefore, the plasmonic resonance in such structures is expected to be strongly overdamped and a negligible antenna effect will be present. Further investigated the dependency of the minimum relaxation time as a function of the chemical potential and could find a figure of merit (δ) for the functionality of graphene based antenna devices [130].

$$(\delta) = \mu_C \cdot \tau_r^2 \tag{3.5}$$

A plasmonic resonance is only present if $\delta \geq 0.1\text{ps}^2\text{eV}$. For the experimental data this would mean a necessary increase of a factor of 14 in relaxation time, by keeping μ_C constant comparing experimentally available materials and the necessary requirements of a reasonable performance graphene antenna. The carrier mobility defines the average speed at which electrons can move within the material. Since diverse carrier mobility values can be achieved by means of different graphene manufacturing processes or by using different substrates [131], [132], we will consider it as a design parameter for graphennas. For a suspended layer of graphene, the carrier mobility is obtained as,

$$\mu = \frac{1}{ne\rho_{xx}} \tag{3.6}$$

where ρ_{xx} is the sheet resistivity.

According to the result in [14] a higher carrier mobility leads to a more resonant behaviour. Fig. 3.4 shows the matrix of impulse responses, wherein each row and column correspond to a chemical potential and carrier mobility value, respectively. The time interval is fixed and ranges from 0 to 10 picoseconds in all cases, whereas the vertical axis limits are also fixed to $[-P, P]$,

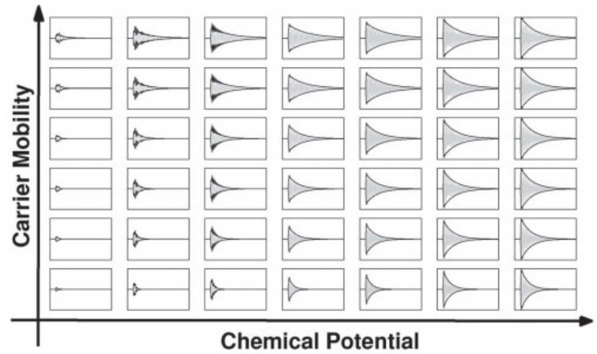

Figure 3.4: Patch antenna with a flexible substrate and graphene as the radiating element.

where P is the maximum envelope peak among all the temporal responses [14].

3.4 Graphene antenna design

A full wave 3D electromagnetic simulation tool, CST Microwave Studio was used to analyze different antenna designs based on graphene acting as the main radiating element. All simulations were done at room temperature (293 K). In the first design, a patch antenna as shown in shown in Fig. 3.5 was analyzed, which consisted of graphene as the conducting material, and a dielectric substrate. For the designing of a micro-strip THz patch antenna, we select the resonant frequency and a dielectric medium for which the antenna is to be designed, and then the parameters of the antenna can be calculated as following. The width of the patch is calculated using the following equation [133]:

$$W \approx \frac{C_0}{2f_r}\sqrt{\frac{2}{\varepsilon_r+1}} \tag{3.7}$$

Where f_0 is the Resonance Frequency W is the Width of the Patch L is the Length of the Patch h is the thickness ε_r is the relative Permittivity of the dielectric substrate c is the Speed of light: 3×10^8.The value of the effective dielectric constant. The effective refractive index value of a patch is an important parameter in the designing procedure of a microstrip patch antenna. The radiations traveling from the patch towards the ground passes through the air and some through the substrate (called as fringing). Both air and the substrates have different dielectric values. The value of the effective dielectric constant ($\varepsilon_r ff$)is calculated using the following equation,

$$\varepsilon_r ff = \frac{\varepsilon_r+1}{2}+\frac{\varepsilon_r-1}{2}[\frac{1}{\sqrt{\frac{1}{1+12\frac{h}{w}}}}] \tag{3.8}$$

Where h is the height of the substrate. Due to fringing, electrically, the size of the antenna is increased by an amount of ΔL. Therefore, the actual increase in length ΔL of the patch is to be calculated using the following equation.

$$\frac{(\Delta)L}{h} = 0.412\frac{(\varepsilon_r ff + 0.3)((\frac{W}{h}) + 0.264)}{(\varepsilon_r ff + 0.258)((\frac{W}{h}) + 0.8)} \tag{3.9}$$

The length L of the patch is now to be calculated using the below-mentioned equation.

$$L = \frac{C_0}{2f_r\sqrt{\varepsilon_e ff}} - 2(\Delta)L \tag{3.10}$$

The width and length of the microstrip transmission line (see Fig. 3.39) required to obtain 50 Ω antenna input impedance at the desired frequency are given as:

$$W_{\mathrm{T}} = \frac{1}{0.8}\left[\frac{9.5138h}{\sqrt{\lambda\left(\mathrm{L}_{3\pi} + 1.41\right)/W}} - t\right] \tag{3.11}$$

$$L_T = 2(2M+1) \times \lambda/2 \tag{3.12}$$

The first step is calculating the conductivity of the graphene CVD. The complexity of the models used to this end will depend on the frequency band of interest and the characteristics of the graphene sheet. The operating temperature, chemical potential, carrier mobility, and the relaxation time of the graphene sample also need to be provided. The effect of μ_c and τ on the radiation performance of the patch antenna was assessed by varying it in the range of 0.1 eV to 0.4 eV, 0.1 ps to 0.8 ps. The return loss of the patch antenna in the THz frequency range is shown in Fig. 3.6. It is noted that as τ is increased, the higher-order modes of the fundamental resonant frequency become prevalent.

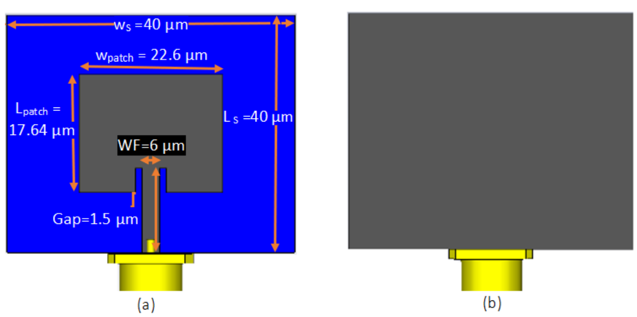

Figure 3.5: Patch antenna with a flexible substrate and graphene as the radiating element.

The strongest resonance has the smallest value of (S_{11}) is −45 dB is obtained at at a chemical potential of 0.4 eV and 0.5 ps relaxation time. The resonant frequency of the graphene also changes when the chemical potential is varied. The effect is shown in Fig. 3.6. When μ_c has a value of 0.4 eV, the resonant frequency is observed at 4.636 THz, whereas at 0.2 eV, it is 4.546 THz. Furthermore, the S_{11} started to increase from−34 dB to almost −37 dB. At 0.4 eV, S_{11} is still below −10 dB at 0.1 ps relaxation time, and get greater reflection coefficient, relaxation time must be increased, as result, S_{11} increased to −45 dB when relaxation time reaches

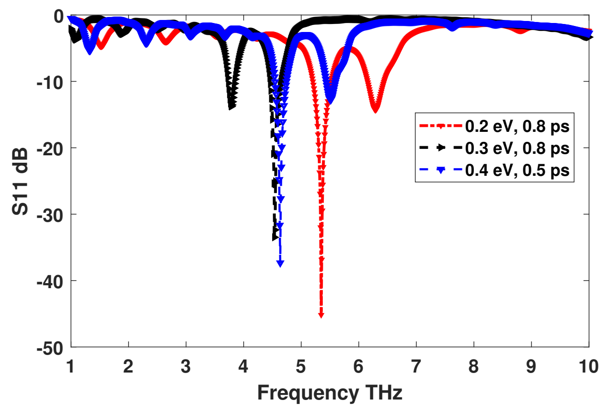

Figure 3.6: The effect of chemical potential observed on the reflection coefficient (S_{11}) in the THz frequency range. The value of μ_c was varied from, (black 0.2 eV, blue 0.3 eV to brown 0.4 eV), whereas τ varied from 0.1 ps to 0.5 ps.

0.5 ps, the resonant frequency shifted to 5.3 THz as an alternative of 4.7 THz at 0.3 eV. The antenna has three possible resonant frequencies as shown in Table 3.1. The thickness of the substrate is evaluated to optimize the antenna performance in terms of the reflection coefficient and bandwidth. From Fig. 3.6, the substrate thickness obviously affects the S_{11} value, however, the bandwidth becomes narrower with increasing substrate thickness (Table 3.2).

f (THz)	μ_c (eV)	τ (ps)	Bandwidth (GHz)
4.546	0.2	0.8	185
4.636	0.3	0.8	204
5.347	0.4	0.5	310

Table 3.1: The effect of chemical potential and relaxation time on resonant frequency and bandwidth.

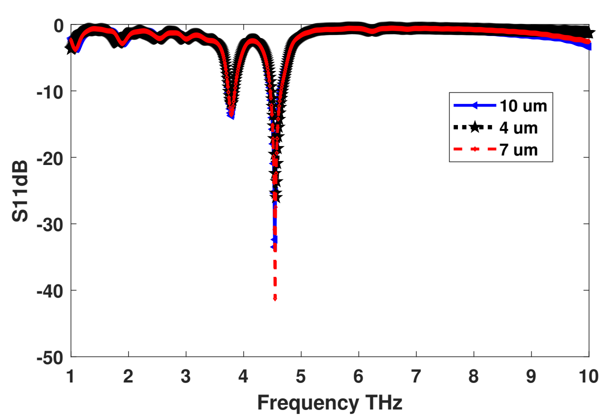

Figure 3.7: Frequency sweep of the reflection coefficient for different values of substrate thickness.

As shown by the results, substrate thickness of 7 µm generates the best resonance with S_{11} of

Substrate Thickness (μm)	f (GHz)	Bandwidth (GHz)	S_{11} (dB)
4	4.546	193.9	-26
7	4.546	192	-41
10	4.546	185	-33.3

Table 3.2: The effect of substrate thickness on the reflection coefficient and bandwidth.

-41 dB, and a bandwidth of 192 GHz. The selection of substrate thickness is therefore a critical design parameter, which strongly affects the antenna resonance. For wearable electronic applications, a substrate material having flexibility is an essential requirement. In order to compare the performance of different types of flexible substrate materials, μ_c of 0.2 eV, and τ equal to 0.8 ps are selected. From Fig. 3.8, polyamide substrate (dielectric constant, ε_r =4.5 and loss tangent, $\tan\alpha$= 0.0027) performs the best in terms of the S_{11} of -42 dB. Polyamide substrate is appropriate for applications demanding a high degree of dimensional stability in extreme environmental conditions. Moreover, polyamide offers a high flexibility and low profile making it the perfect substrate material for printed fabrication techniques. On the other hand, Rogers 3006 substrate yielded a return loss of -40.6 dB, and for polyethylene terephthalate (PET), it was -30 dB. For paper, the return loss was -30 dB.

The tunability of graphene is shown in Fig. 3.9, where the resonant frequency is changed with the help of chemical doping and applying an external voltage bias. Table 3.3 provides a comparison of the three different resonant frequencies obtained for a substrate of thickness 7 μm. All the frequencies have approximately the same S_{11} with the notable difference in bandwidth, which increases as the chemical potential increases. On the other hand, the transmission range gets lower when the electric potential is increased due to an increased absorption.

In Figure.3.10a 3.10b, the radiation patterns illustrate high main lobe magnitudes along with lower back lobes levels. The main lobe magnitude in the E-plane starts from 2.93 dB at a chemical potential of 0.2 eV, and with increased μ_c the main lobe magnitude decreases to 1.51 dB at 0.3 eV, and -1.41 dB at 0.4 eV.The proposed design suggests that the graphene-based patch antenna resonates at different frequencies in the THz band, 4.546 THz, 4.636 THz and 5.347 THz when the chemical potential and relaxation time are varied. Furthermore, changing the chemical potential leads to an increase in bandwidth from 199 GHz at0.2 eV to 314 GHz at 0.4 eV. On the other hand, chemical potential affects the radiation pattern by increasing the side lobe and reducing the directivity of the proposed antenna. Analysis has also been performed to evaluate the antenna bandwidth and reflection coefficient (S_{11}) at resonant frequencies. A comparison between different flexible substrates allows to evaluate the effect of substrate material on the antenna performance. A graphene-based antenna with polyamide substrate shows the maximum S_{11} of -42 dB.

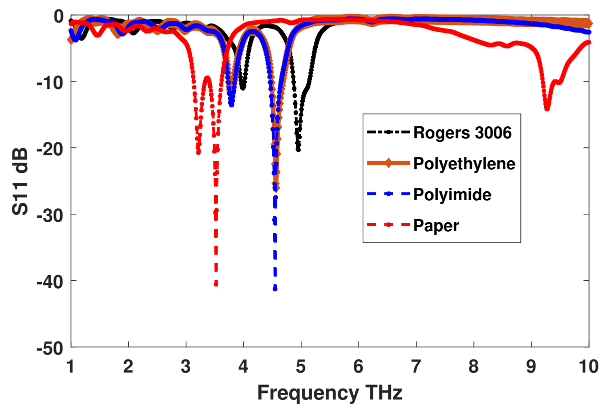

Figure 3.8: Reflection coefficient (S_{11}) of different substrate material thickness 7 µm, Rogers 3006,Polyethylene, Polyamide, Paper.

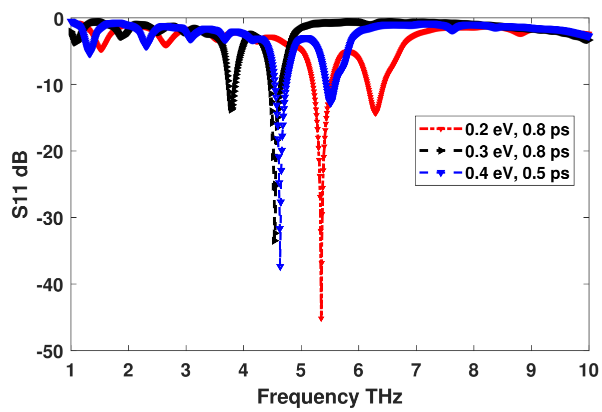

Figure 3.9: Antenna resonant frequencies at 7 µm thickness (0.2 eV and 0.8 ps red, 0.3 eV and 0.8 ps, black 0.4 eV and 0.5 ps).

f (THz)	μ_c (eV)	τ (ps)	Reflection Coefficient(S_{11})	Bandwidth (GHz)
4.546	0.2	0.8	-41.258	199
4.636	0.3	0.8	-40.187	279.9
5.347	0.4	0.5	-41.283	314

Table 3.3: A comparison between different resonant frequencies at 7 µm substrate thickness.

3.5 Body-centric THz networks

Remote real-time monitoring of a patient's vital signs offers numerous advantages over conventional health monitoring. For example, Remote Health Monitoring (RHM) systems have proven effectiveness in decreasing healthcare costs and improving quality of life by reducing mortality, morbidity, and economic costs associated with hospitalization [134]. In addition, remote monitoring in day-to-day healthcare shows great potential as it is easy to perform and is particularly beneficial in cases involving frail, elderly and housebound patients [135]. Furthermore, it provides an efficient approach for monitoring patients with chronic disease through continuous

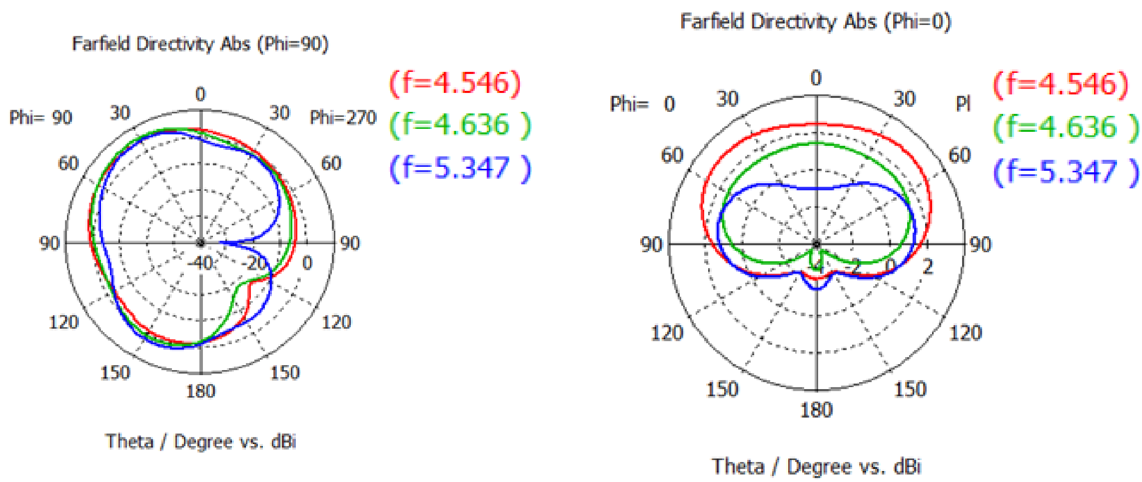

(a) H plane

(b) E plane

Figure 3.10: Simulations of the normalized field patterns in the E plane and H plane at different frequencies.

assessment of symptoms and signs of the disease [136]. RHM systems also have the potential to increase empowerment of people by enabling the public to actively manage their well-being as part of their lifestyle [137]. A Wireless Body Area Network (WBAN) is a key functional component of RHM systems. It is a network that connects a series of biological sensors placed at different locations around the human body. A coordinator node enables these sensors to communicate and transmit physiological data to a remote device, such as a smart phone or personal computer (PC), for real-time monitoring. 3.11 [138]. In recent years, WBANs have been used

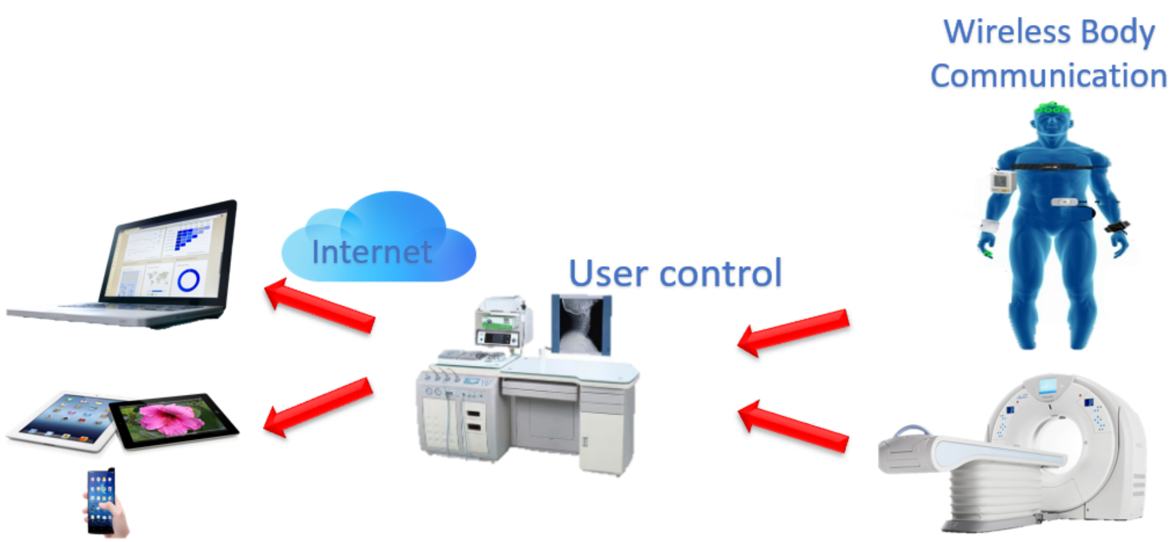

Figure 3.11: Hierarchical architecture of wireless body Centric system

for a range of applications, including physiological and biochemical sensing, motion detection, and gait analysis [139]. Smart fabrics, which is combine conductive materials with e-textiles, are of great use for WBAN applications, they provide a comfortable and user-friendly approach to remotely monitor a patient's health without having cables surround the patient [140]. For most wearable devices, it is important they work wirelessly to ensure operational flexibility [141]. Hence, wireless communication protocols are important to enable connectivity between the WBAN and other devices. There are several wireless communication protocols that support WBAN applications. For example, Bluetooth is a wireless technology protocol commonly used in the application of WBANs for remote patient monitoring. It was originally designed as a shortrange wireless communication standard that allowed a wireless device to connect with up to seven other devices. Bluetooth operates within the Industrial Scientific Medical (ISM) band at 2.4 GHz [142].

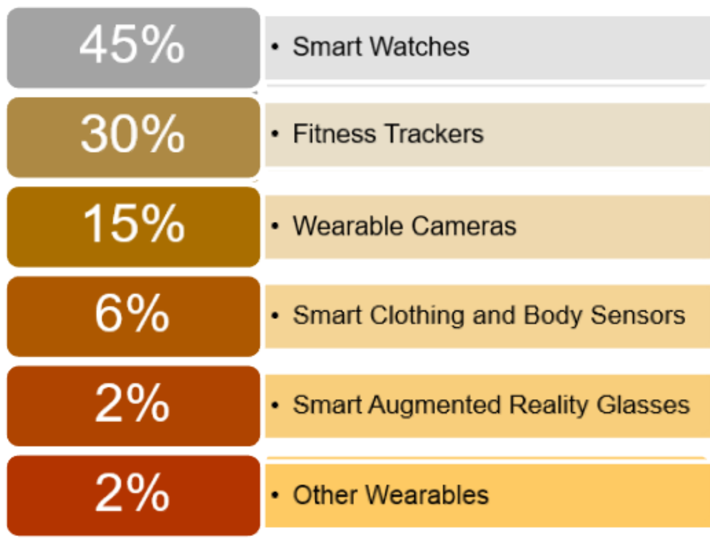

Figure 3.12: Wearable Devices Forecasting [142]

The ISM band is internationally recognised as one of the most commonly used standards in wireless communication systems and can be used without a special licence for a range of purposes. Antennas are devices that convert electrical signals into electromagnetic waves, and vice versa [143]. They play a key role in communication technology as they enable wearable devices to receive and transmit data wirelessly [144]. Compact antennas can be used to develop user4 friendly portable Radio-Frequency (RF) and microwave devices [145].

As such, small wearable antennas are being applied in a range of areas including health monitoring, physical training, navigation, medicine and military operations. For applications in RHM systems, antennas can either be attached directly to the human body or integrated into clothing. They behave as transducers, remotely receiving and transmitting physiological data from the human body to a wearable device. The integration of antennas within flexible electronic systems has driven significant technological advancements [146]. Flexible electronics has been a popular research interest in recent years due to its attractive characteristics, which include light-weight, cost efficient manufacturing, simple fabrication, and availability of low-cost flexible substrates [147]. The THz band is very promising to enable connectivity in body-centric networks (BCNs). Due to the unique THz propagation properties and sensing capabilities, and due to the THz radiation's relative safety to biological tissues [148], the THz spectrum can improve the performance of existing BCNs, thus enabling various medical applications [149].

Because of the substantially high absorption in human skin, the path loss is considered more from the molecular absorption loss than the spreading loss. More particularly, at the same frequency and distance, the exponential loss caused by the molecular absorption is approximately double the spreading loss contribution to the path loss. Furthermore, it is demonstrated that the path loss increases with both the transmission distance and frequency and that the path loss would reach 80 dB when the transmission distance increases to 2 mm for all the three different human tissues [150].

3.5.1 Perimitivity of human skin at THz band

As such, these systems would be highly suitable for integration into wearable RHM devices. The demand for wearable devices is expected to increase to 187.2 million wearable units annually by 2022 [151]. Wearable antenna requirements for all modern applications require lightweight, low-cost, and a flexible profile. For WBAN scenarios, the antenna design becomes more complicated than free-space environments, due to the absorption of the human skin. Human skin is a complex, heterogeneous and anisotropic medium, where minuscule organs such as blood vessels and pigment content are spatially distributed in depth [152]. With the complexity of human skin, it is challenging to accurately describe the material, mainly due to the shapes and function, and most importantly because of the absence of the dielectric constant measurements at high frequency [153]. Therefore, most of the latest research simulates the human skin as three layers; epidermis, dermis, and hypodermis which represent the most essential parts of the human skin [154]. Wearable antennas, therefore should be carefully designed to minimize skin absorption.

The antenna design becomes more complicated than simple free-space environments, due to the absorption of the human skin. Human skin is a complex, heterogeneous and anisotropic medium, where small parts, like blood vessels and pigment content are spatially distributed in depth [152]. With the complexity of human skin, it is challenging to accurately simulate the structure, mainly due to the shapes and functions (see Fig 3.13), and the lack of the permittivity measurements at THz frequency [153].

Layers of human skin are shown in Fig. 3.13 where the thickness of each layer varies from person to person. For the epidermis, the typical thickness ranges from 0.05 to 1.5mm and $1.5-4$mm for the dermis. The hypodermis has no typical value [155]. The epidermis contains two layers with only dead squamous cells and the living epidermis layer, where most of the skin pigmentation stay. The stratum comeum is a thin accumulation on the skin outer surface. The dermis that supports the epidermis, is thicker and mainly composed of collagen fibers and

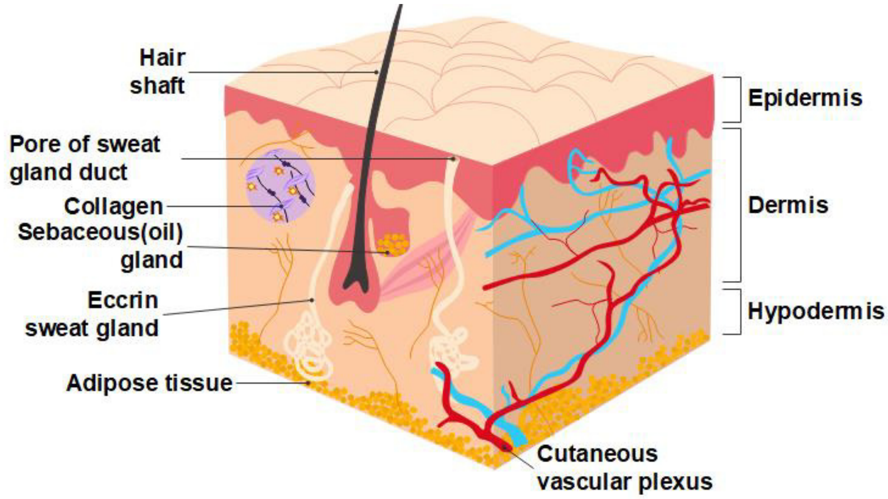

Figure 3.13: Human skin Design Drawn on Fusion

intertwined elastic fibers enmeshed in a gel-like matrix. The subcutaneous fat layer is composed of the packed cells with considerable fat, where the boundary is not well defined, thus, the thickness of this layer differs widely for various parts of the human body. The permittivity of human skin tissues can be obtained using [156].

$$\varepsilon'(\omega) = \varepsilon_\infty + \frac{\varepsilon_s - \varepsilon_2}{1+(\omega\tau_1)^2} + \frac{\varepsilon_2 - \varepsilon_\infty}{1+(\tau_2)^2} \tag{3.13}$$

$$\varepsilon''(\omega) = \frac{(\varepsilon_{s-}\varepsilon_2)(\mathrm{w}\tau_1)}{1+(\omega\tau_1)^2} + \frac{(\varepsilon_2 - \varepsilon_\infty)(\omega\tau_2)}{1+(\omega\tau_2)^2} \tag{3.14}$$

Where Here $\hat{\varepsilon}(\omega)$ is the complex permittivity as a function of angular frequency, ε is the limiting value at high frequency, ω is the angular frequency $(\omega = 2\pi f), \tau$ is the mechanical relaxation time at an intermediate frequency. ε_s is the static dielectric constant, ε_∞ is the limiting value at high frequency, and ε_2 is an intermediate frequency limit [157] [158].

Table 3.4: Parameter human skin values

Reference	Model	ε_s	ε_2	ε_∞	τ_1(ps)	τ_2(ps)
Ref [63]	Epidermis	58	3.6	3	10.0	0.20
Ref [62]	Dermis	60.0	3.6	3	9.4	0.18

Using Eq. 3.14 and 3.13 and the values in Table. 3.4 the permittivity can be calculated for frequencies between 0.1 – 1.2 THz. The real part of the dielectric constant of the two-layer human skin model can be seen in Fig 3.14 a, while the imaginary part of the dielectric constant for the same layers can be seen in fig 3.14 b. Both Figures contains the information that describes how electromagnetic waves behave in this frequency range for these three layers. Three layers of the human skin model as shown in Fig.3.15, and the hybrid antenna placed on the top.

Three layers of human skin model as shown in Fig. 3.15b, the thickness of which differ

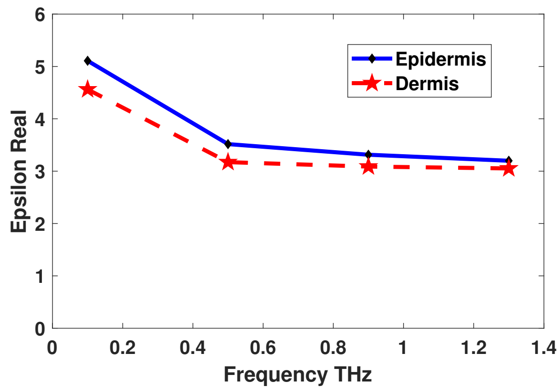

(a)

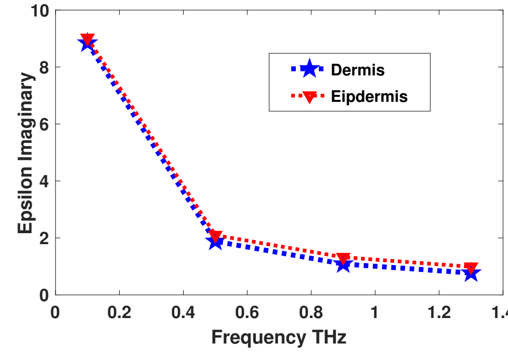

(b)

Figure 3.14: Imaginary and Real part of permittivity of human skin.

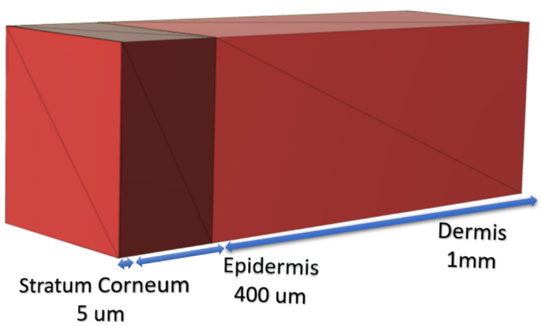

(a)

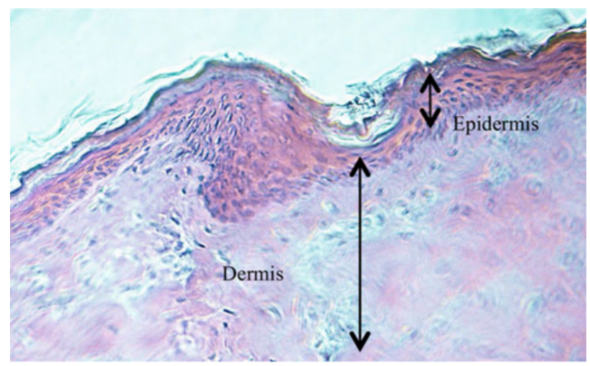

(b)

Figure 3.15: (a) Simulation of human skin in CST (b) Microscopic image of real human skin presenting the two defined layers: epidermis and dermis [159].

between various human skins. For the epidermis, the typical thickness ranges from 0.05 mm to 1.5 mm, whereas the dermis is typically 1.5×10^{-4} mm. The hypodermis, on the other hand, has no typical value [155]. The epidermis is sibdivided into two further layers, the stratum corneum with only dead squamous cells and the living epidermis layer, where most of the skin pigmentation stay [14]. The stratum corneum is a thin accumulation on the skin outer surface. The dermis that supports the epidermis, is thicker and mainly composed of collagen fibers and intertwined elastic fibers enmeshed in a gel-like matrix. The subcutaneous fat layer is composed of the packed cells with considerable fat, where the boundary is not well defined, thus, the thickness of this layer differs widely for various parts of the human body.

3.6 THz serial antenna design

In comparison to traditional vital sign monitoring equipment, non-contact detection of breathing and cardiac rate using Doppler radar is a convenient technique to examine a person vital signs [160] [161]. Remote Vital Signs Monitoring is thus required in various levels of health care, rescue services, and the military and defense sectors [162] [163]. However, the monitoring system accuracy and dependability should be managed appropriately for its practical systems [164] [163]. Three antenna arrays composed of ultra-wide patch elements were developed in this study for the accurate detection of human BR and HR at 0.8 THz band frequencies. The array antenna can be used to minimise interference from reflected signals from side objects, since the suggested antenna arrays have smaller radiation beamwidths than a single element patch antenna. The suitability of the THz band for health care monitoring has been investigated in this section.

The ultra-wide patch components provide a great trade between gain and array size. Due to the arrays low side lobe level, high gain, and narrow beamwidth, the electromagnetic (EM) wave was focused on the target, which enhanced RVSM accuracy. Additionally, the size of all arrays were large enough to allow for cost-effective production using standard Photolithography techniques. Youngs modulus of graphene is excellent, allowing for mechanical flexibility, and graphene may also be able to address the problem at hand. Flexible, stretchy, or even conformal features may be added to gadgets by using graphene-based good judgement devices because of its atomically thin thickness and super electric capabilities. Even more importantly, graphene aids in the generation of SPPs capable of showing high wave restriction and moderate loss by supporting the propagation of these SPPs via Graphene. Graphene remarkable electromagnetic, mechanical, electrical, and thermal capabilities have made it possible to conduct short-range communication in the THz frequency range. It has become the dominant platform material at THz frequencies. An essential benefit of employing graphene is the ability to create lightweight, thin, and low-cost flexible antenna devices. To make things even more flexible, stretchy, or even conformal in any application, graphene-based devices may have atomically thin profiles and amazing electrical characteristics.

3.6.1 Antenna design

The antenna community is inspired by the planar antenna's simple construction, cheap cost, and low profile to create a variety of other planar antennas to satisfy the needs of future wireless communication systems. An advantage of a single-element antenna is that it has a wide emission pattern and a low directivity coefficient. For long-distance wireless communication, antennas with high-directionality are necessary. An electrical and geometrical arrangement of single components may produce a beam with a great degree of focus and precision (gain). The term array refers to this kind of antenna with several elements.

Owing to the skin depth effect, the surface resistivity of typical conductors rises with frequency, resulting in extremely poor radiation efficiency at large sizes due to the accompanying significant ohmic losses, as explained in the preceding chapter. To improve the radiation effectiveness of THz antennas, the conductor's surface impedance should be decreased by the use of

Distance b/w patch	400um
Width feed 50 Ω (Ws)	38um
Thickness of Gold	0.5um
Thickness of graphene	0.35 nm
Cpw Gap	7um
Substrate (PEN)	1.3 mm × 1.8 mm

Table 3.5: Antenna parameters

a hybrid design using 2DMs such as graphene. The metal and graphene gold are inextricably linked in their operation and resonances.

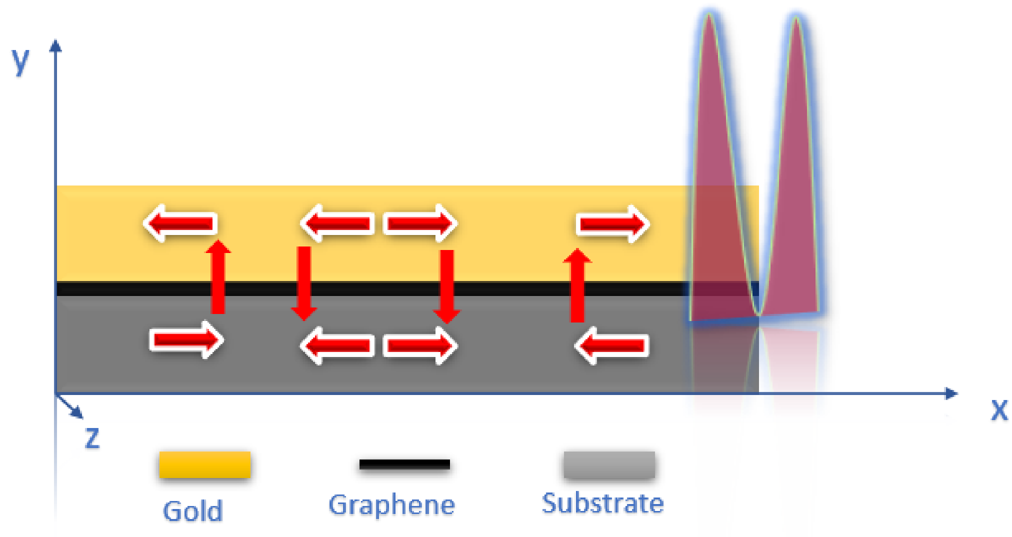

Figure 3.16: Graphene and Gold interface

There is now research underway on the potential of a three-layer hybrid THz antenna for use in wearable electronics. Graphene and gold are the two radiation elements that we are utilising in this design. As a performance-enhancing material, graphene is utilised in conjunction with conventional metals like gold, which have adequate thickness for production and measurement.

It is possible to manipulate the form and structure of these materials when they are mixed, and this may assist solve the difficulties in manufacture and measurement. It is expected that substrate material and attributes will be changed to increase the antenna bandwidth, efficiency, and overall gain. Analyses of graphene influence on antenna radiation properties near the human body are provided and discussed in here. The geometry of the proposed nano antenna array structure is shown in the Fig. 3.19. The array radiating elements have been fabricated on a flexible and bendable dielectric substrate. As shown in Fig. 3.17, the proposed antenna array uses two radiation elements, namely graphene and gold, with Ti and Aluminium as adhesive layers to the substrate.

For design convenience, the proposed antenna is fed by a 50 feed line with a voltage divider. The dimensions of the antenna are shown in the figure and table The antenna's optimised di-

(a) Gold metal antenna arrays on Flexible PEN substrate

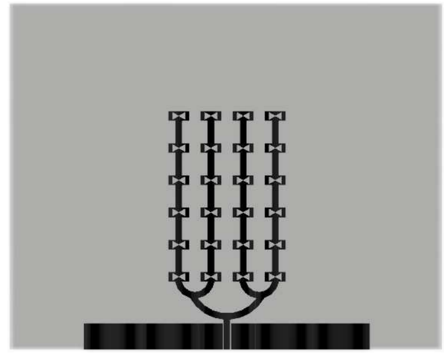

(b) Graphene material antenna arrays on Flexible PEN substrate

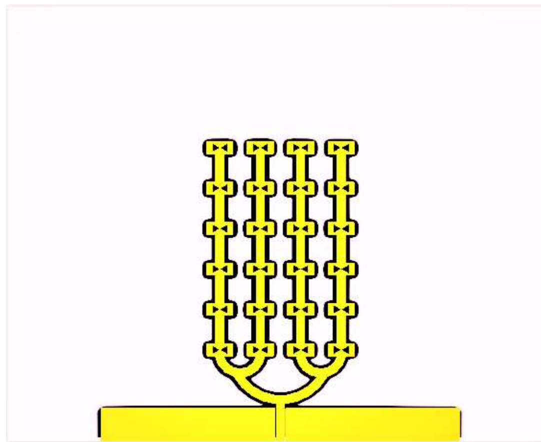

(c) Graphene and Gold interface array structure

Figure 3.17: CPW Antenna Arrays designing steps

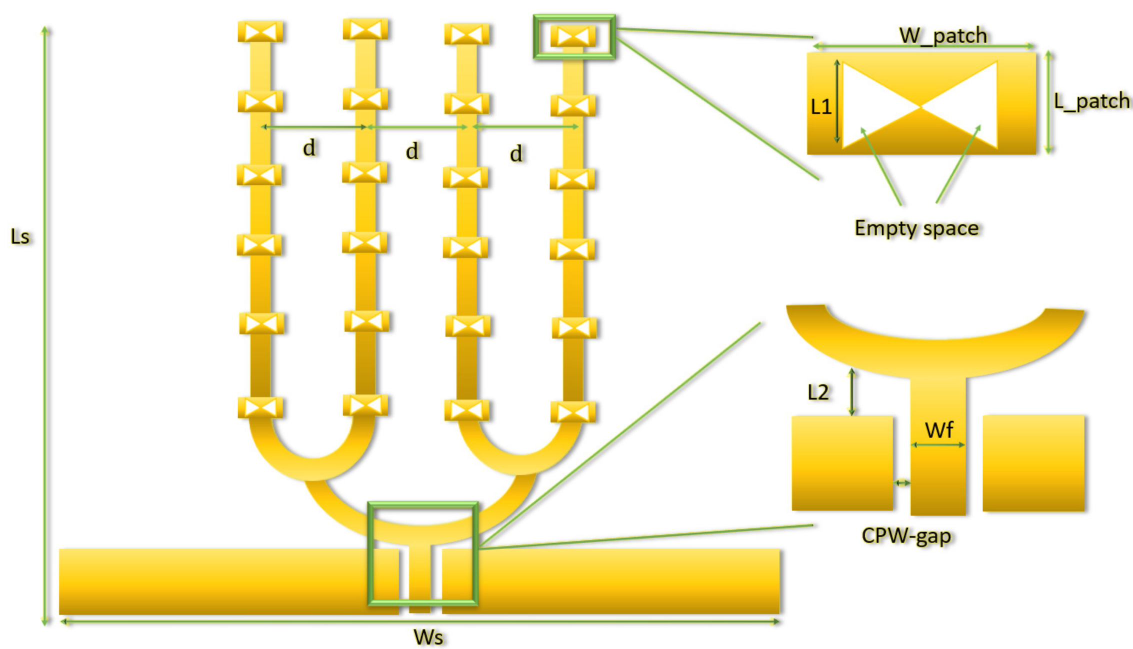

Figure 3.18: Cpw THz Antenna Arrays Dimension

mensions are given in Table 3.5 and Fig 3.18. The dielectric constant of the substrate is 2.2, and the substrate has a thickness of 125 um, which is the smallest thickness available on the market. Figure 3.19 (b) shows the antenna layout with respect to the coordinate system. An initial design has been obtained to meet the ultrawideband bandwidth requirements. The antenna is designed to meet the limitations of fabrication and measurement in the THz band. The arrays consist of 24 elements with a thickness of 500 nm.

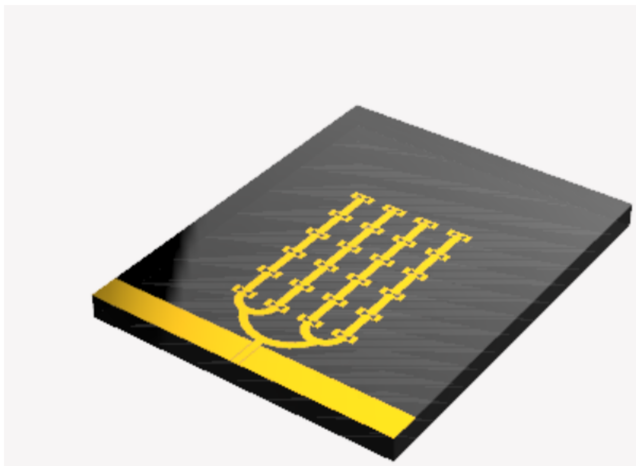

(a) Front View

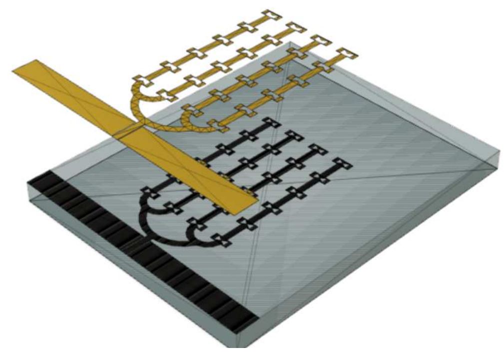

(b) Gold,Graphene,and Titanium

Figure 3.19: CPW Antenna Arrays Structure

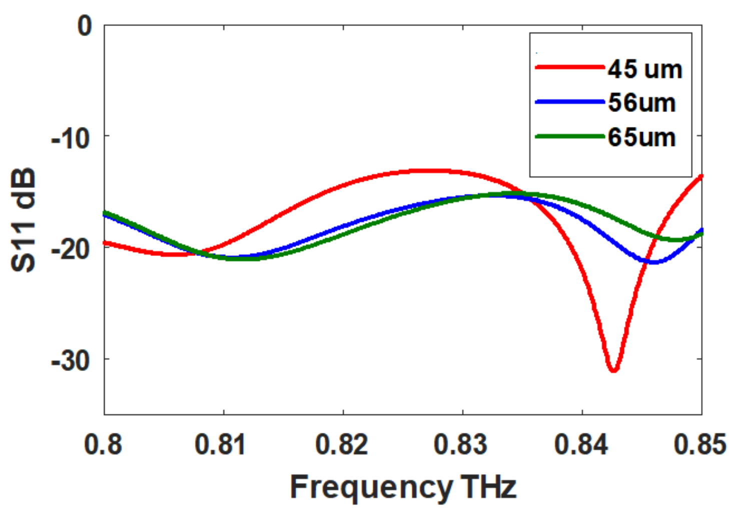

Figure 3.20: S_{11} with different patch lengths

Figure 3.20 shows S_{11} with different antenna dimensions. It can be seen that S_{11} is the lowest and equals -18 dB when the length is 65 um. To put it another way: When you have a length of 45 um, S11 is at its greatest, and it at its lowest. S_{11} , with a 45 um length and 118 um wide, has the greatest antenna performance. In this instance, the bandwidth is, on the other hand, a little less than the others demission. Antennas with a 45 um and 118 um effective width and length have been discovered.

All dimensions are calculated using the equations described in the previous section. The SEM images shown in Fig 3.24 clearly show the CPW gap and the feed line width. Human skin is a complex, heterogeneous and anisotropic medium, where minuscule organs such as blood vessels and pigment content are spatially distributed in depth [152]. With the complexity of human skin, it is challenging to accurately describe the material, mainly due to the shapes and function, and most importantly because of the absence of the dielectric constant measurements at high frequency [153]. Therefore, most of the latest research simulates the human skin as three layers; epidermis, dermis, and hypodermis which represent the most essential parts of the human skin [154]. Wearable antennas, therefore should be carefully designed to minimize skin absorption.

3.7 Photo lithography fabrication

Wafers were cleaned progressively in acetone, isopropyl alcohol, and dilute hydrochloric acid. A primer was spin coated for 20 seconds at a speed of 4800 mpm and then baked at 115C for 35 seconds. SPr resist, a positive photoresist, was spin coated at a 4800 -rpm speed and baked for 60 seconds at 900 C. Lithography was carried out using a picture mask that served as the standard mask for the first alignment marks. A 34 seconds exposure with MA 6 was used, followed by a 3 -minute development in CD26.

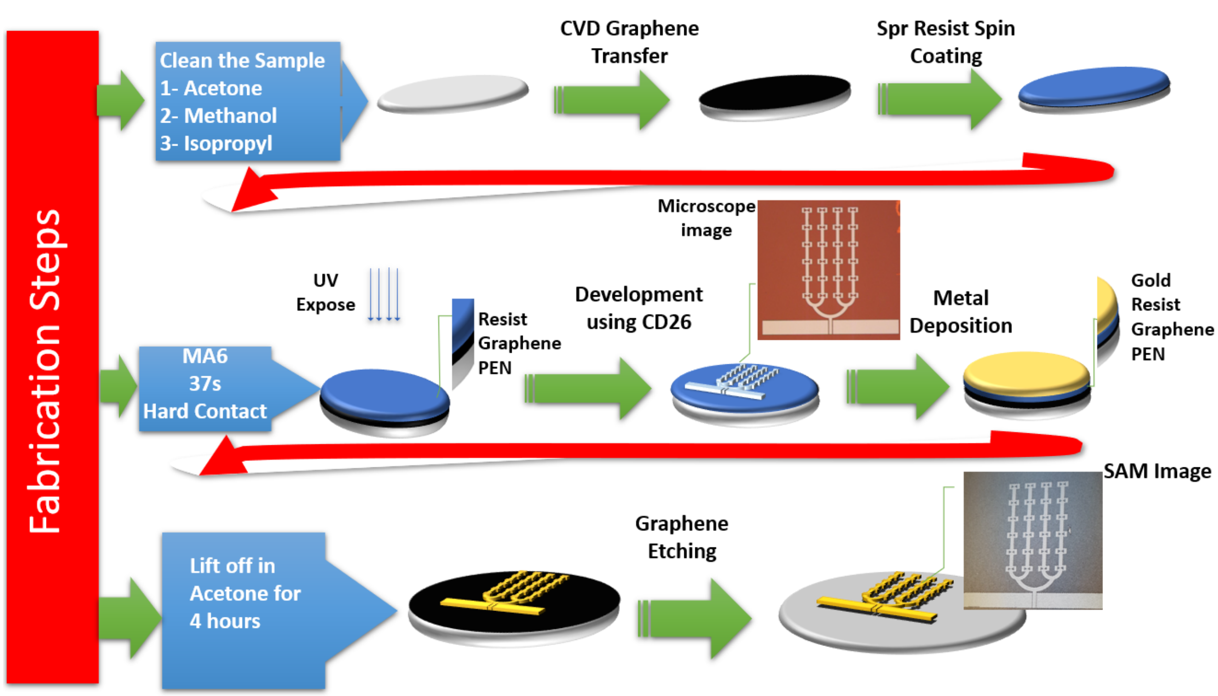

Figure 3.21: Antenna arrays fabrication steps

This was followed by a 50-second hard bake at 80C on a hot plate. Following development, the patterned portion of the pen substrate was exposed for asher. Plasma ashing is a critical and

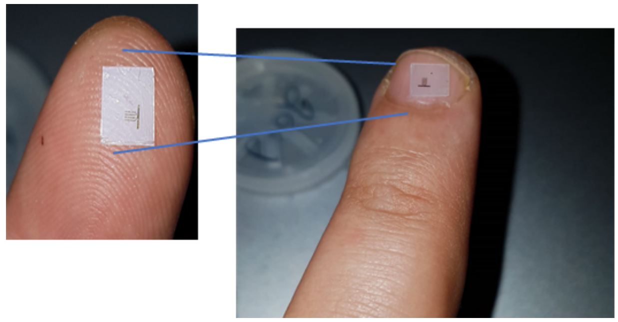

Figure 3.22: The purposed Cpw THz Antenna Array on finger

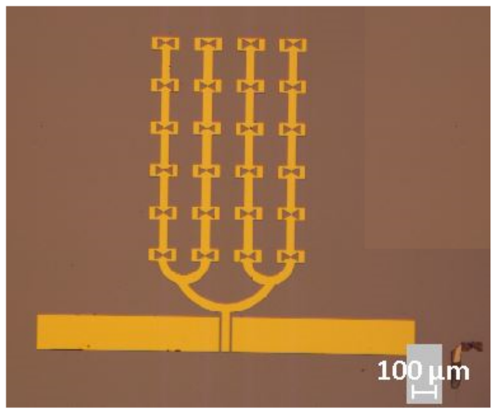

Figure 3.23: An optical micrscope image for the purposed Cpw THz Antenna Array

commonly performed technique in manufacturing.

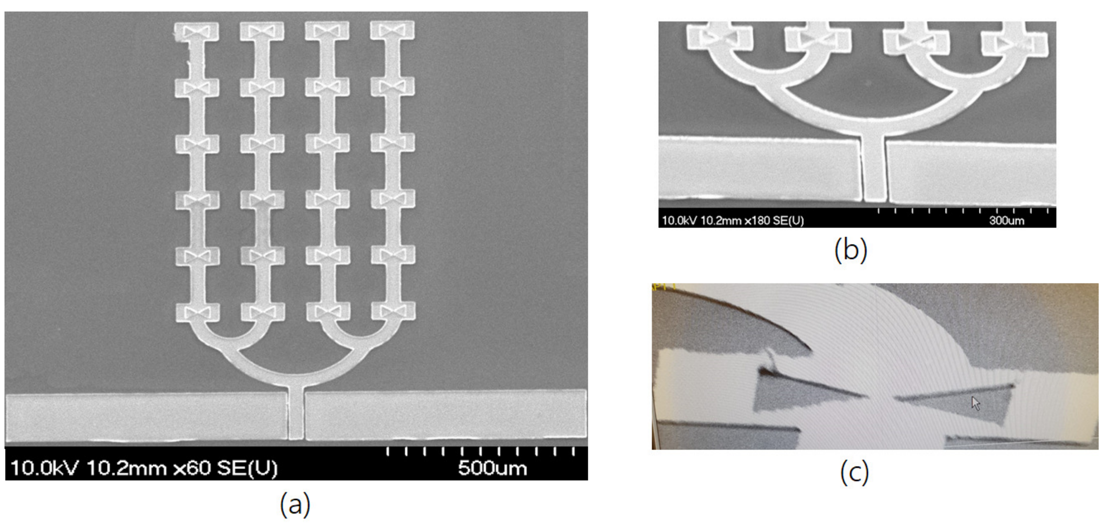

Figure 3.24: SEM image of a plasmonic THz antenna arrays prototype based on nanoscale Au contact 0.35 nm graphene material

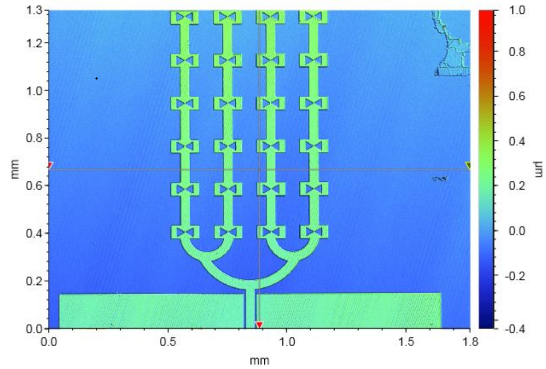

(a)

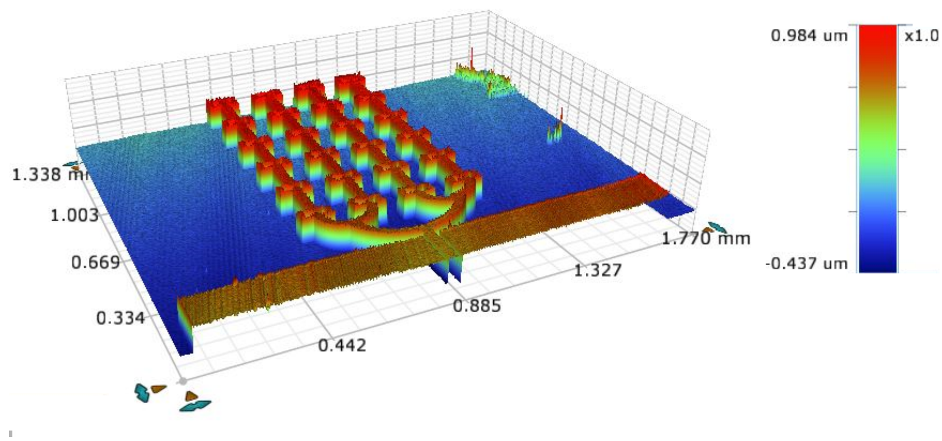

(b)

Figure 3.25: Optical counter GT image of THz antenna arrays profile

3.8 Results and discussions

In terms of graphene conductivity, chemical potential and relaxation time have a significant impact.

A broad range of frequencies may be produced by raising the chemical potential and relaxation period. Due to the increase in graphene absorption level, raising chemical potential has a negative effect on radiation efficiency. This results in a good match between the source and feedline, but a decrease in radiation efficiency since more power is absorbed by the graphene material, which results in a loss of power. It was decided to keep things simple by using a normal chemical potential value of 0 eV and a relaxation period of 0.1 ps to maximise the radiation and overall efficiency while minimising absorption inside the material itself. The simulated reflection coefficients of the 24 elements array shown in Fig. 3.26, which shows the excellent antenna performance as the whole response is below the 10 dB range. Figure 3.27 shows the surface electric current distribution of the proposed arrays at the operating frequency, and this result show that the current reaches the tip of the antenna, causing radiation of the EM waves.

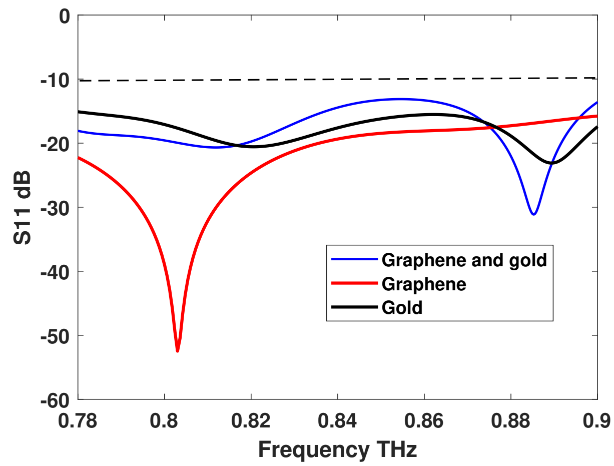

Figure 3.26: Simulated S11 profile of the designed graphene antenna, gold , and gold graphene antenna

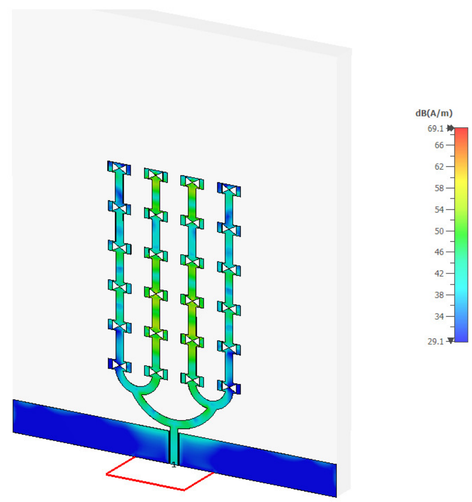

Figure 3.27: surface current distribution of purposed Cpw THz Antenna Array

3.8.1 Flexibility of the Antenna

Fabric qualities limit the machine flexibility after stretching. For flexible and stretchy electronics, materials with high strain limits and the ability to be manufactured in thin layers are required. However, a gadget that seems to be bendable does not always mean that it is flexible. Conformal electronics, surface-mounted smart sensors, and bioelectronics all need systems with a high stretch capacity. Flexible and even stretchy materials must be employed in wearable devices to keep up with the body mobility. This is because graphene, as an alternative to typical rigid materials, possesses mechanical qualities that may be used as software in a wide range of wearable devices. The implanted antenna performance is examined under two bending scenarios with varying bending radii. The impact of bending in the x-direction is investigated in this example. The antenna x-direction curved design is seen in the Fig 3.28. The simulated antenna S 11 for various bending radii is shown in Fig 3.29. The thickness of the copper sheet was taken into account while determining these radius values for the simulation. This gold sheet has a thickness of 0.5 um, and the simulation results will be impacted if the radius is set to a value that causes the gold sheet to break. A radius of 10^0, 20^0, or 30^0 degree was selected as a consequence for bending.

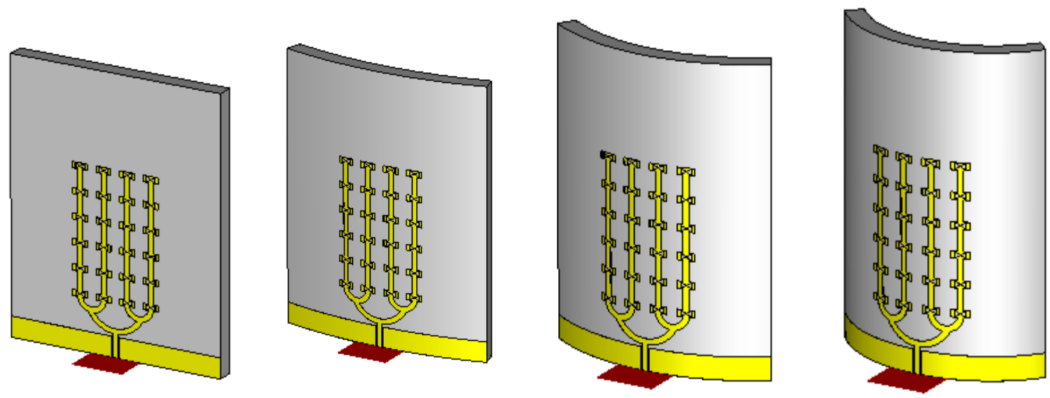

(a) 0° (b) 10° (c) 20° (d) 30°

Figure 3.28: Different bending angle for the purposed antenna

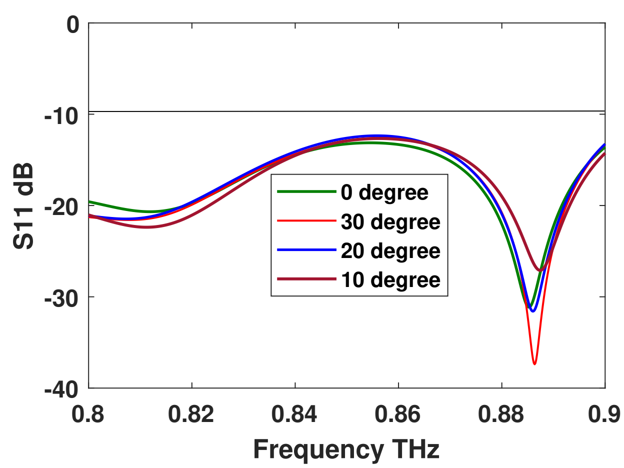

Figure 3.29: S11 magnitudes for different bending angles shown in Fig.3.28 and without bending

A nonflat antenna platform is more likely when an antenna or sensor is attached to the human body for wearable applications. Human movement may also cause the antenna to bend at various angles. As a result, a small, flexible antenna is required that can perform effectively at particular bending angles. Thus, a 0.8 THz simulation bending antenna is described to better understand the complicated antenna bending electromagnetic properties and their influence on the antenna parameters. Resultantly.

When bending the antenna to 20 and 30 degree, the resonance frequency and operating bandwidth are still the same. in all bending angle , the S11 still below - 10 dB. A noticeable change in resonance frequency and -10 dB bandwidth can be seen as the radius decreases.

3.8.2 Human skin body scenario

Models of the human skin were developed in CST to examine how they affect the antenna ability to operate. As seen in Fig.3.30, the model is composed of a skin, fat, and muscle layer. Using an average adult height and weight, the thickness of different tissue layers was selected. A consideration of the dielectric characteristics of each tissue is necessary since the human body is a heterogeneous and multilayered medium. Therefore, the dispersion properties of each tissue were determined throughout the required frequency range in order to correctly mimic the human thorax.

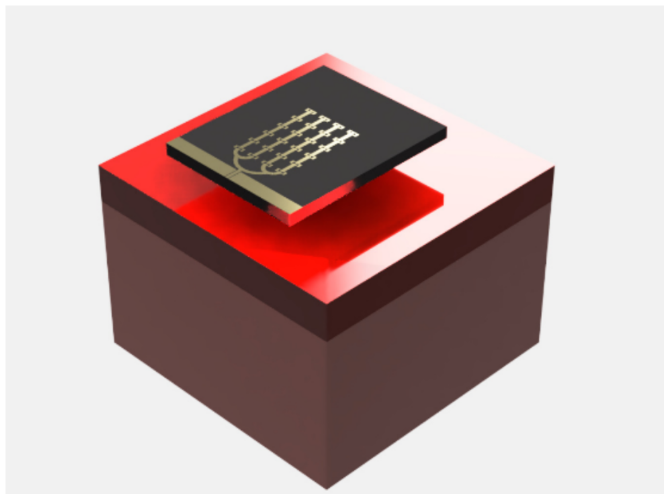

Figure 3.30: Three layers model of the human skin designed in CST

The array antenna on the body has an S11 value of -25 dB as can be seen in Fig 3.32. Three layers of the human body have a high dielectric constant, which causes frequency detuning. These property of the human body result in an even broader -10 dB bandwidth as the most of the emitted waves go through the body and dissipate as heat.

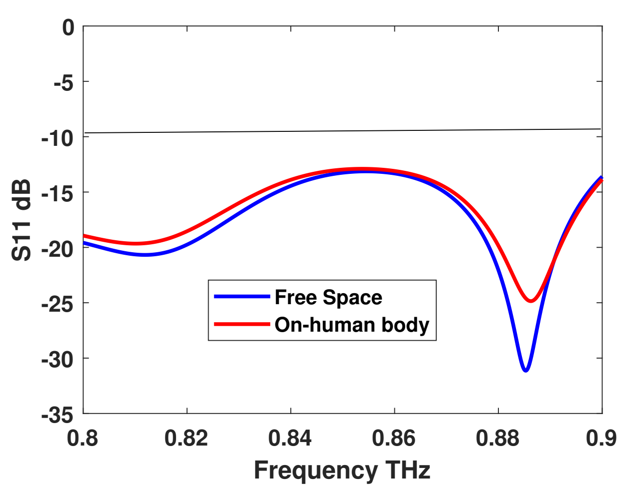

Figure 3.31: Simulated S11 profile of the designed graphene and gold antenna

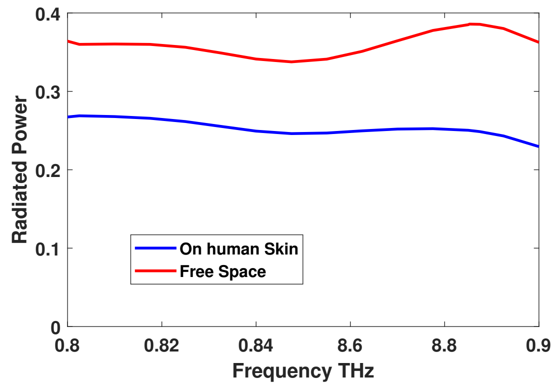

Figure 3.32: Simulated radiated Power from the array

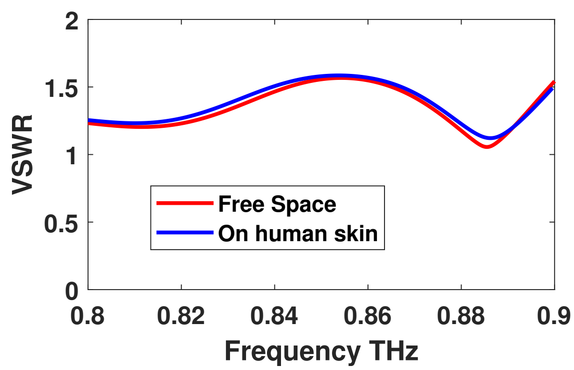

Figure 3.33: Simulated VSWR

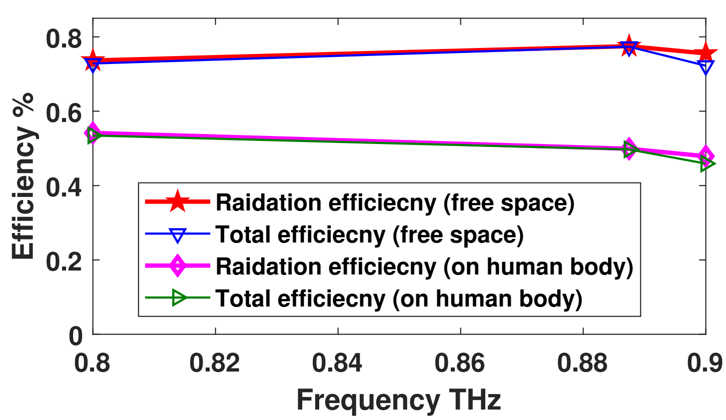

Figure 3.34: Efficiency of the antenna on free space and human body

The shift in frequency is due to the high dielectric constant property of three layers of the human body in proximity with the antenna. Because of these properties of the human body, most of the radiated waves propagate through the body and dissipate in the form of heat resulting in a wider -10 dB bandwidth. Due to the body absorption, the antenna gain decreases from -7.8 dB to -7.2 dB. The antenna gain is a figure of merit of how well the antenna converts the power supplied into radiated waves in a specific direction. For the case of the on-body condition, a

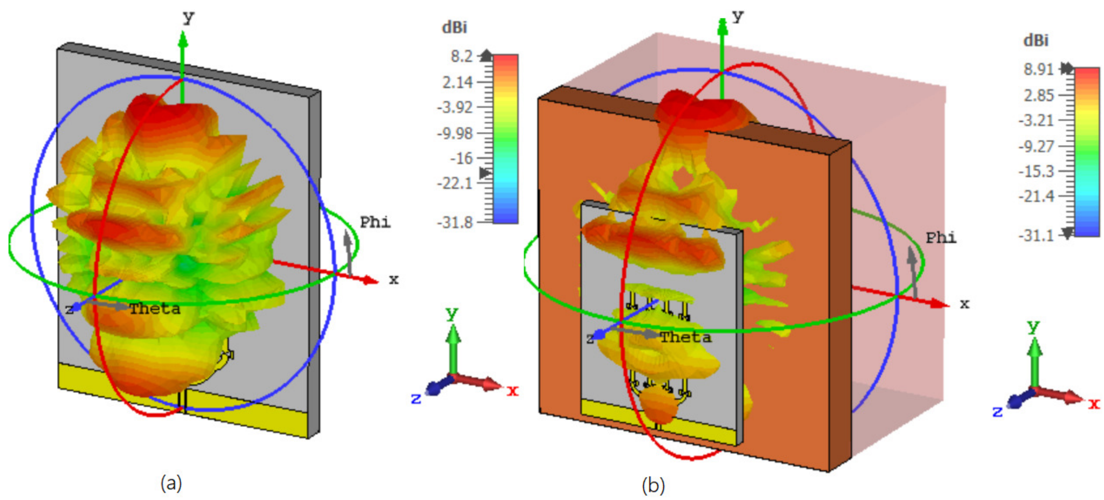

Figure 3.35: 3D radiation pattern of purposed Cpw THz Antenna Array

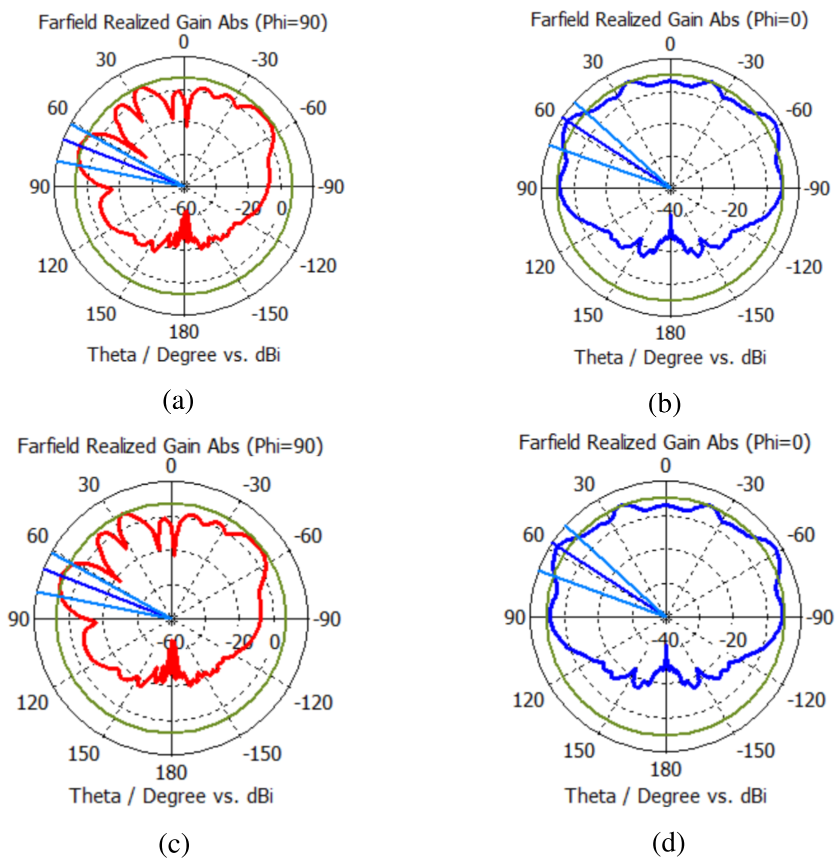

Figure 3.36: Simulations of the normalized field patterns in the E plane and H plane on human skin

lower value of the gain is obtained which is due to a decrease in the radiation efficiency, down from 96 % to almost 50 % (Fig. 3.34).

The Figure 3.35 depicts a simulated 3D radiation pattern at 0.9 THz with a maximum gain of 8.9 dB. At 0.9 GHz, three distinct antenna designs with coaxial feed produce three-dimensional (3D) radiation patterns. The results indicate that antennas in free space produce almost directed

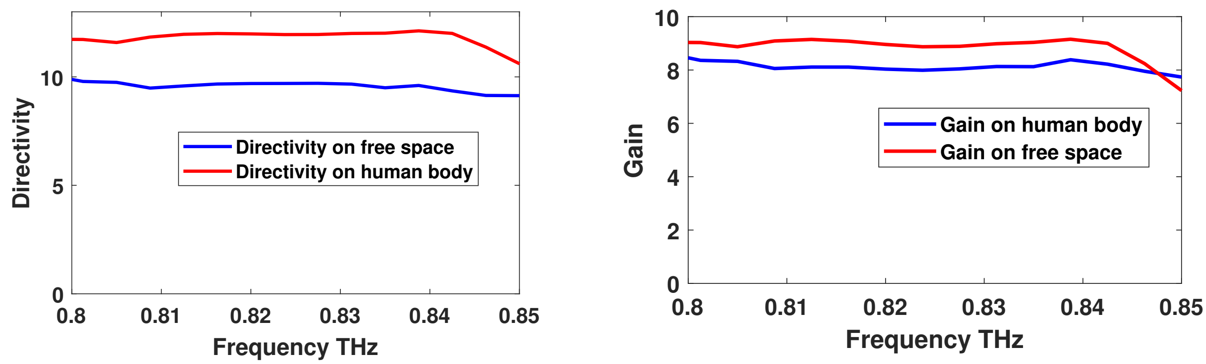

(a) (b)

Figure 3.37: Gain and directivity of the antenna arrays on free space and human body

three-dimensional radiation patterns with little distortion at various angles. When the antennas are positioned directly on the phantom (0 um), the three-dimensional radiation patterns seem more directed at certain angles. As can be seen, the antenna transmits almost the same amount of power throughout a large angular range (beam-width). On the other hand, a high gain implies that the antenna performs well in a particular direction, as seen in Fig 3.36d, which depicts the pattern at 0.95 GHz with a maximum gain of 10 dBi. That is, the intensity of the radiation is greater in the direction of greatest gain than in other directions. Additionally, it is critical to notice that the suggested antenna radiates upward (perpendicular to the substrate) toward the air side.

For the two primary planes, the modelling of the radiation pattern of the purposed antenna is shown in Fig.3.36 a b and Fig 3.36 c d (H plane and E plane). The normalised H plane shows an omnidirectional radiation pattern. High lobe magnitude and low side-lobe levels may be seen. The gain, bandwidth, and radiation patterns of the antenna array are appropriate for point to point wireless links including for giving proper coverage in point to multi-point coverage when positioned in the centre of the ceiling.

3.9 Hybrid perovskite THz antenna array

Perovskites are materials described by a chemical formula ABX_3 where A and B are cations of different sizes (A being larger than B) and X is an anion [165]. Their crystallographic stability and probable structure can be deduced by considering the tolerance factor t defined as the ratio of the distance A−X to the distance B−X in an idealised solid-sphere model and the octahedral factor χ [166]. For halide perovskites where X = F_2, Cl_2, Br_2, I_2, t generally ranges from 0.81 - 1.11 and χ between 0.44 - 0.90. If t lies in the narrower range 0.89 - 1.0, the cubic structure of Fig. 3.38 is likely, with lower t values giving less symmetric tetragonal or orthorhombic structures [167].

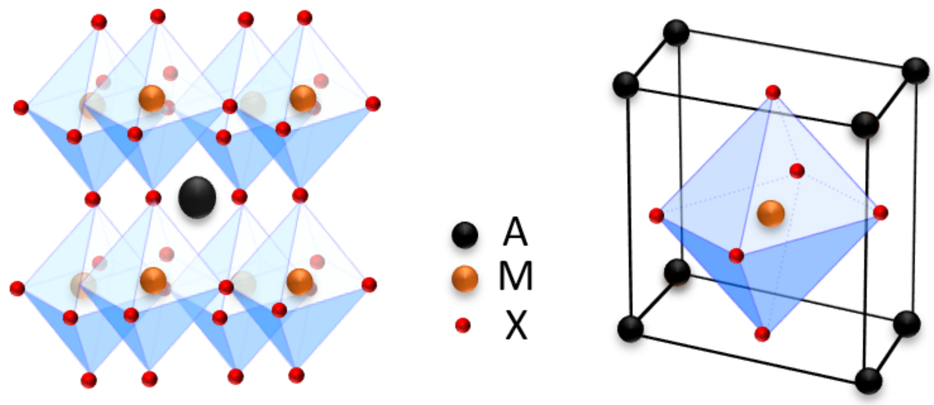

Figure 3.38: ABX 3 perovskite structure

3.10 Antenna design

The hybrid antenna design proposed in this section is simulated and analyzed using a full−wave commercial electromagnetic solver, CST Microwave Studio 2018. The perovskite material was set through the complex permittivity values by following. Figure 3.39 and Table 3.6 shows the antenna design with the dimensions $2000 \times 1000 \times 125 \mu m$, consisting of a perovskite based picat patch, a gold pica patch, and a substrate. From Fig 3.41, the antenna consists of perovskite, gold and a polyethylene napthalate (PEN) substrate. The proposed antenna has a width of $5000 \mu m$ and the length is configured as $5000 \mu m$. Thin flexible film of Polyethylene naphthalate (PEN) is used as a substrate with the dielectric constant of the PEN substrate is $\varepsilon_r = 2.5$ and loss tangent $\tan\alpha = 0.00025$), which can provide an ultrawideband (UWB) with omnidirectional coverage.

Table 3.6: Dimensions in μm of the designed antennas array

Dimension	Size extension
W_{Patch}	$70 \mu m$
L_{Patch}	$119 \mu m$
$W_s 50\Omega$	$43 \mu m$
$W_{100}\Omega$	$12 \mu m$
$W_{70}\Omega$	$4 \mu m$
L_1	$40 \mu m$
d	$350 \mu m$

Figure 3.41 illustrates the antenna consisting of $CH_3NH_3PbI_3$ perovskite, gold, and a pen substrate, which is one of the transparent and flexible substrates, commonly used in the development of flexible electronics. A PEN substrate offers a good resistance to chemical solvents and high resistivity to high temperature [168].

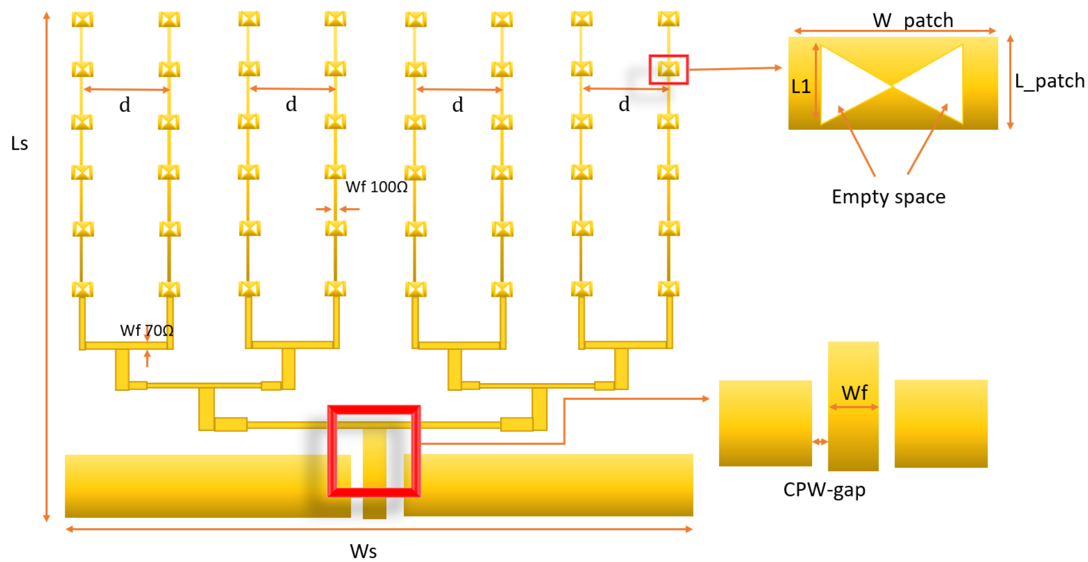

Figure 3.39: Dimensions of The Patch Antenna Arrays

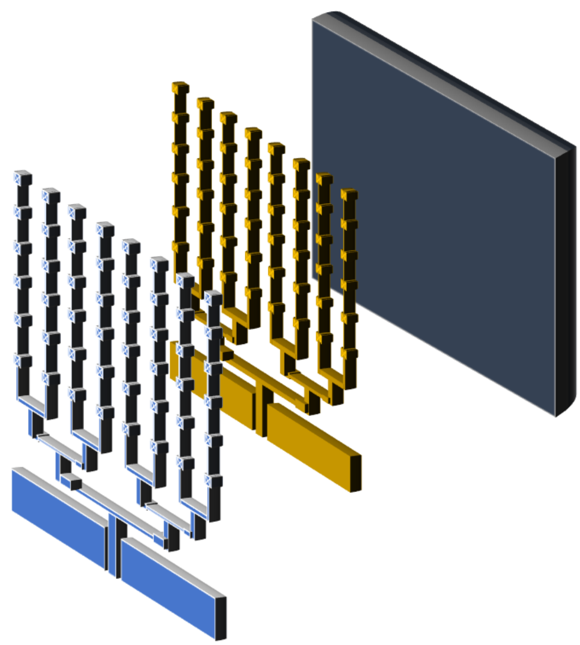

Figure 3.40: Three Layered Antenna Structure

3.11 Results and discussion

Figure 3.42 shows the simulated reflection coefficient in the frequency range of 0.9 , 1.4 THz. The perovskite material separately as well in a hybrid combination with gold provides an excellent antenna performance in the desired frequency range. From Fig 3.43, the results shown that, the value of VSWR is less than 2.5 in the frequency band of 0.9 - 1.4 THz. On the other hand, due to the skin depth effect of the conventional conductive materials at THz band, perovskite materials have significantly higher conductivity and better antenna performance.

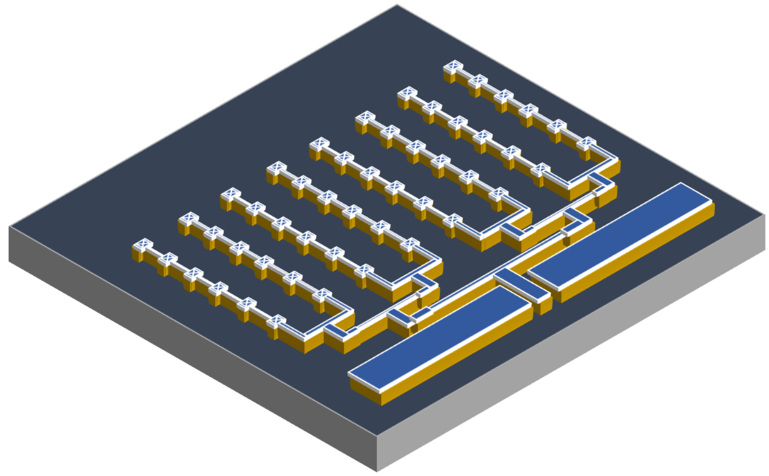

Figure 3.41: Antenna Profile

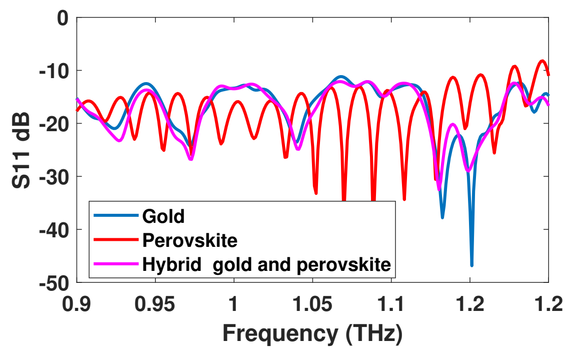

Figure 3.42: Simulated S_{11} Profile of Antenna

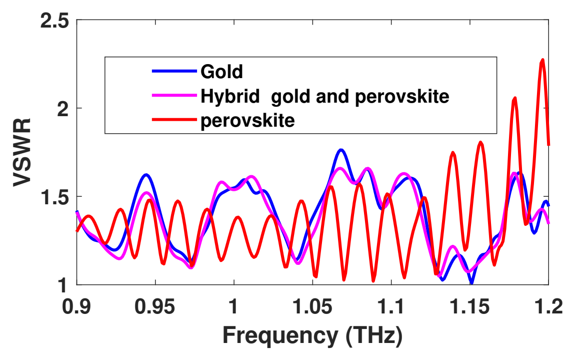

Figure 3.43: Antennas VSWR Versus Frequency.

The radiation efficiency of the antenna is shown in Fig 3.44. Although the radiation efficiency at the lower end of the desired band range decreases at a frequency of 1.05 THz, it is still achieving a high radiation efficiency above 83% for both perovskite and hybrid materials designs. As the conductivity of perovskite increases, consequently, the radiation efficiency is improved, on the other hand, the conductivity of gold declines with the frequency higher than 1.05 THz due to high surface impedance which leads to degree d of radiation efficiency, the gold antenna efficiency continues to decrease until it reaches a value of 65% at 1.2 THz. The

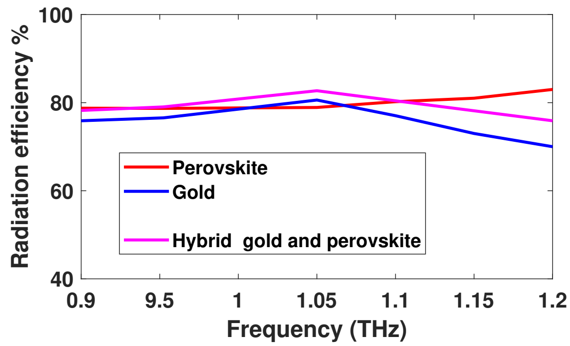

Figure 3.44: Radiation efficiency of the three materials separately

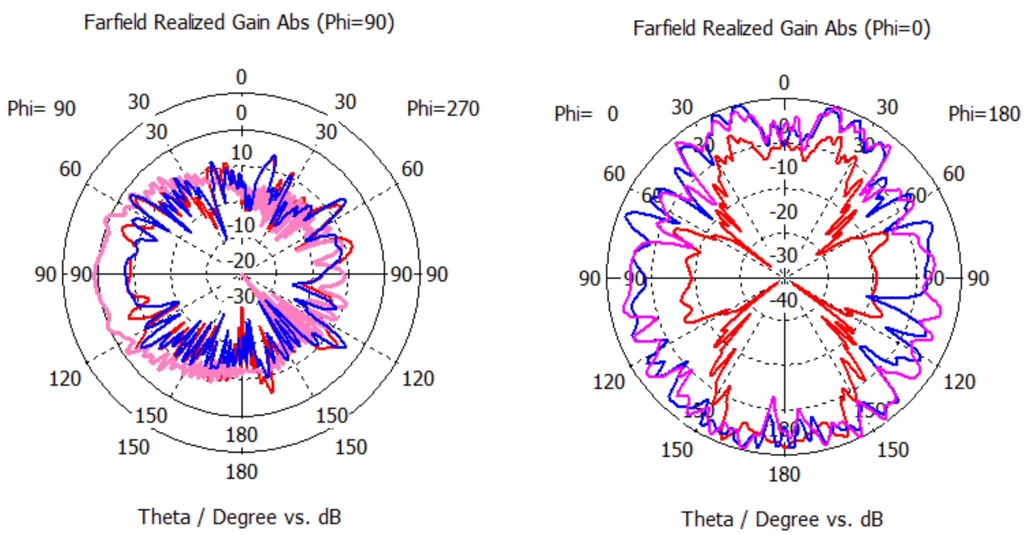

(a) E−plane

(b) H−plane

Figure 3.45: Proposed antenna design: (a) Antenna structure; (b) Front view.

radiation efficiency of the perovskite material and the hybrid material structure (gold and perovskite) maintain an excellent radiation efficiency of 85% and 80% respectively. Both structures maintain a high efficiency within the target frequency band.

Table 3.7: Compression between three antenna structures

Antenna	Gain	Dirctivity
Gold	8.942 dBi	10 dBi
Hybrid antenna	10.13 dBi	11.3 dBi
Provskite	11.4 dBi	12.05 dBi

The antenna array gain gradually increases with frequency for both perovskite and hybrid material structures (Table 3.7). A gain of 10 dBi at 1 THz operating frequency for gold antenna. Whereas for the hybrid antenna array, the gain achieve was 10.13 dBi at 1 THz. The highest gain achieved at 1 THz was 11.4 dBi with the perovskite based antenna array. Figure.3.45 shows the simulated E- and H-plane radiation patterns at representative selected frequency 1

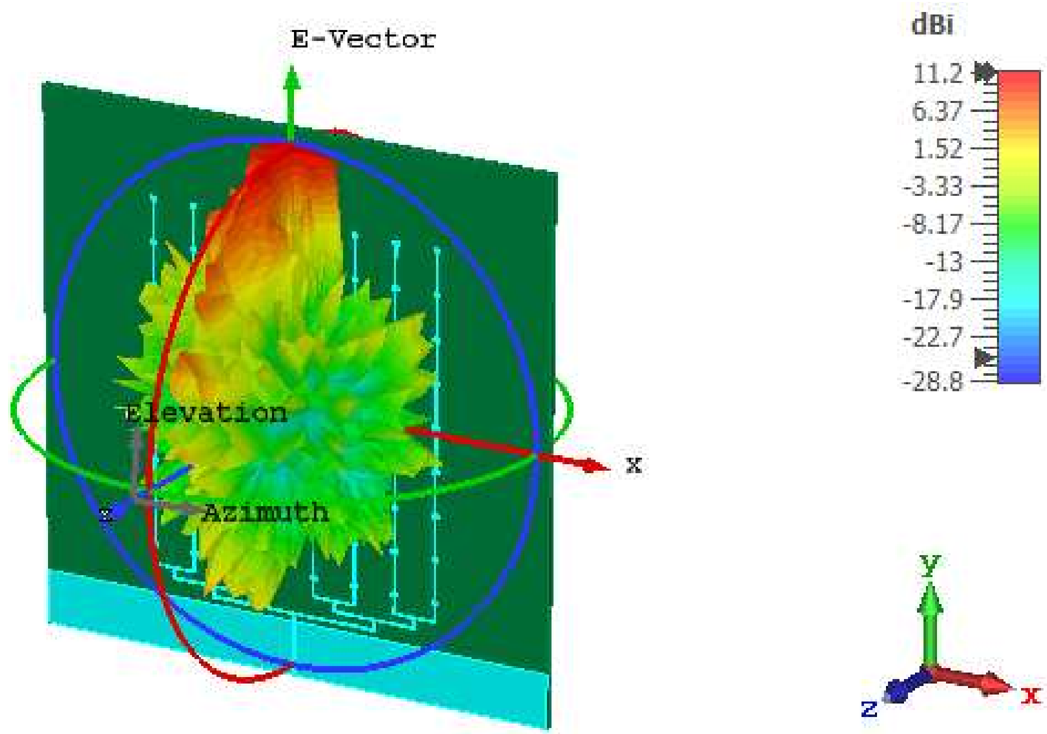

Figure 3.46: 3D radiation pattern of purposed Cpw THz Antenna Array

THz. It is seen that this antenna has nearly omnidirectional radiation characteristics, while the cross-polarisation level rises with frequency increase owing to the horizontal components of the surface. In spite of the fact that the radiation is not an ideal broadside in the total working range, yet this impact is evident when the antenna is intended to spread a wide data transmission. The high transmission capacity, high gain, and high efficiency indicate that the perovskite can be conveyed as an enhancement material in the THz patch antenna. A fundamental proof of concept has been presented for the deployment of advanced materials such as perovskite for antennas with a reasonable efficiency. Novel materials have been developed for potential deployment in modern THz systems to achieve high performance.

The results indicate that the antenna performs much better than a gold-only antenna in the frequency band of 0.9 - 1.2 THz. Additionally, the suggested work demonstrates that with the rapid advent of two-dimensional materials with electrical conductivity, the performance may be enhanced further by doping or external biasing. Due to the ultrathin nature of the suggested multilayered structure and the flexibility of the substrate, the proposed design is suitable for biomedical imaging and wearable applications.

3.12 THz antenna based on MoS_2 material

At the moment, the most extensively utilised process for creating monolayer MoS2 samples with diameters greater than a few micrometres includes different types of exfoliation [169] [170] [171]. However, we have devised a large-scale production method for monolayer-MoS2 films with diameters of several millimetres using chemical vapour deposition (CVD) [172]. Subsequent advances in the purity and quality of monolayer-MoS2 film synthesis on a variety of substrates have been made. This has been accomplished by carefully optimising the CVD growth conditions to tolerate surface corrugations [173].

Recently, monolayer molybdenum disulfides, such as monolayer MoS2, have emerged as viable SPP materials owing to their straight band gap and high spin-obit couplings, which significantly minimise SPP losses. Additionally, the MoS2 nanostructure has superior photoelectric characteristics and has been proposed for usage in field effect transistors [174]. As seen in fig 3.47, the single layer of MoS2 has an S-Mo-S structure similar to that of a sandwich.It turns out that monolayer MoS_2 has two phrases: metallic 1 T and semiconducting 2H. MoS_2 can be used as a semiconductor material with a direct (indirect) bandgap of $1.96eV(1.2eV)$. Covalent bonds link the atoms. Theoretical studies of SPPs in monolayer MoS2 nanostructures are presented in [100].

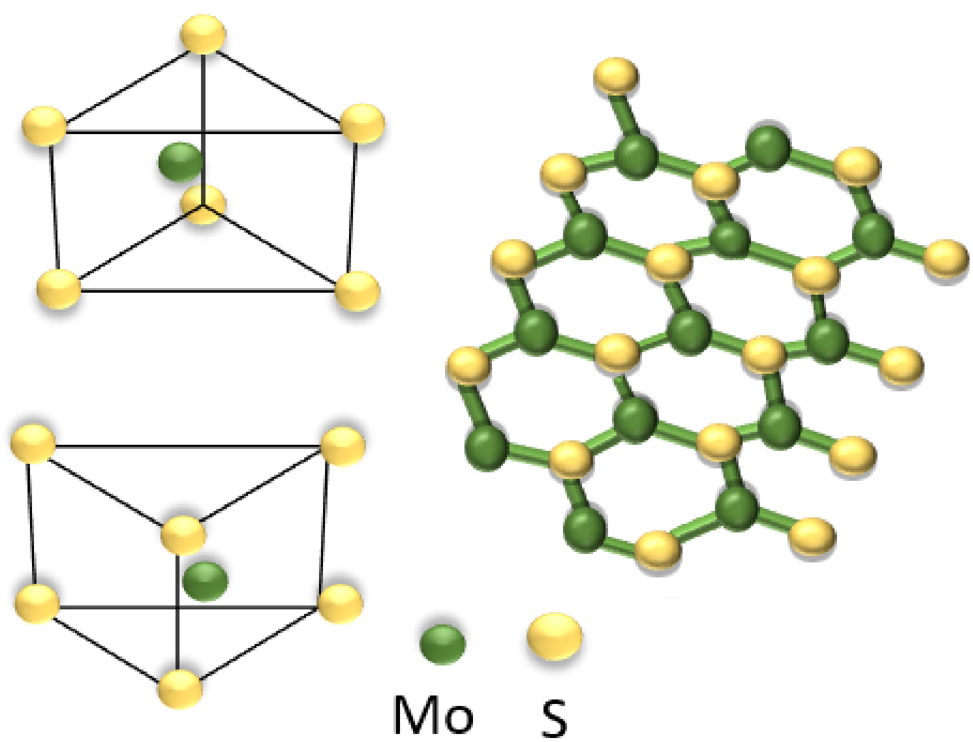

Figure 3.47: MoS2 material Structure.

In Figure 3.48, the dispersions of SPPs for the different dielectric constants ε_S of the substrates are shown at a fixed electron density $n_e = 1 \times 1011$ cm -2. It shows that the influence of the substrate to SPPs is obvious. For the small values of k_{spp}, the excitation frequency ω

of SPPs increases obviously with the increasing wave vector k_{spp} of SPPs, but the excitation frequency ω is saturated as k_{spp} increases. For the different substrates ε_S, the different SPPs and saturation frequencies are achieved. Their difference is almost unchanged at a larger k_{spp} value, which shows that the difference of SPPs for different substrates weakly depends on k_{spp} for the large values of k_{spp}. Subfigure of Fig 3.48., shows depression of SPPs for the different electron densities ne with $\varepsilon_S = 2$ of substrates. Consequently, the functions of the SPPs in MoS2 nanostructures can be controlled by varying electron density, and we can achieve GHz SPPs by changing $n_e \sim 1011\ \mathrm{cm}^{-2}$. These outcomes indicating that monolayer MoS_2 is a promising candidate for THz antenna propagation for future wireless communication.

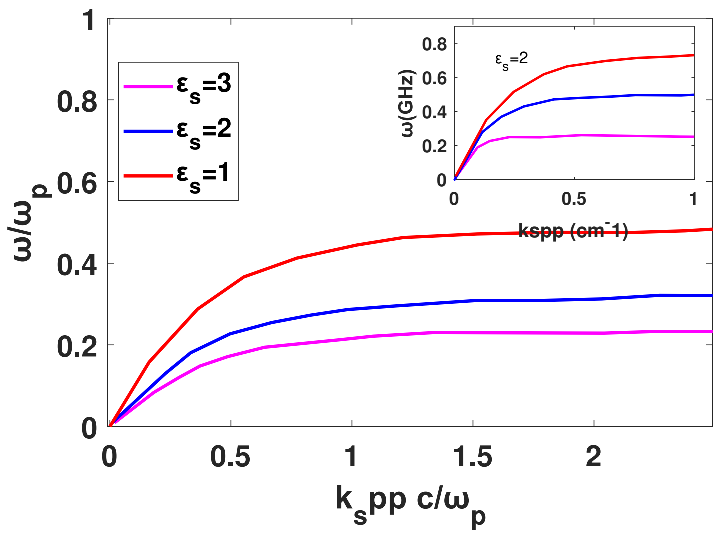

Figure 3.48: Surface plasmon polarization of MoS2 material.

3.12.1 Antenna Design

The hybrid MoS_2 / Gold antenna design is simulated and analyzed using a full-wave commercial electromagnetics solver, CST Microwave Studio. The MoS_2 material was set through the complex permittivity values. Figure 3.49 shows the antenna design with the dimensions $2400 \times 1600 \times 50\mu m$, consisting of a MoS_2 based folded, gold, and polyimide substrate. Thin flexible film of Polyethylene naphthalate (PEN) is used as a substrate with the dielectric constant $\varepsilon_r = 3.5$ and loss tangent $\tan\alpha = 0.00025$) Fig 3.50.

3.12.2 Results

Figure 3.52 shows simulated reflection coefficient S_{11} in the frequency range of 0.85 to 0.95 THz. The hybrid material design separately as well as gold provides an excellent antenna performance in the desired frequency range. Folded antenna based gold materials achieve the -10 dB at the whole frequency band. The results in 3.52a shows that, the value of VSWR is less

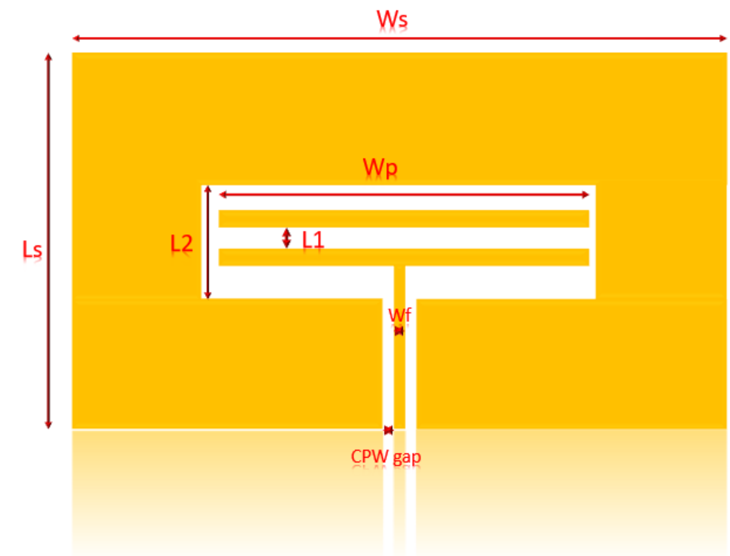

Figure 3.49: Proposed Antenna Design

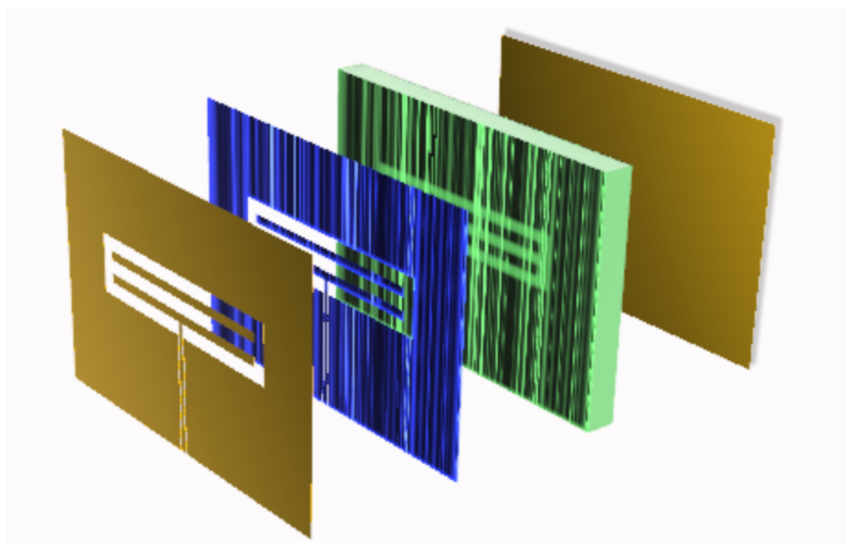

Figure 3.50: Proposed Antenna Layers Structure

than 2.5 in the frequency band of 0.85 to 0.95 THz. Compared to gold and $MoS2/gold$ designs, the $MoS2/gold$ has significantly higher conductivity which leads to better reflection coefficient performance, and this is due to the skin depth effect of the conventional conductive materials at THz band. The radiation efficiency of the antenna is shown in Fig. 3.54a. It is clear that adding MoS_2 material increases the radiation efficiency of the antenna, on the other hand, the conductivity of gold declines with the increasing in frequency due to high surface impedance. A maximum gain of 12 dBi is achieved with Mos2 hybrid structure and about 11 dBi at the high end of desire band 3.52b.

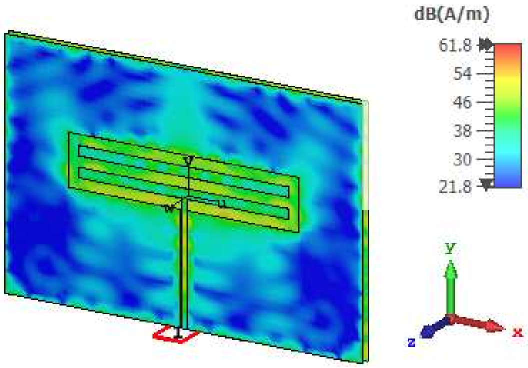

(a) Gold / MoS2

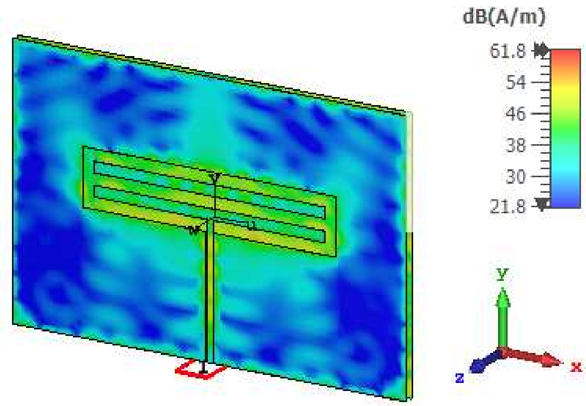

(b) Gold

Figure 3.51: Surface Current Distribution at 0.8 THz

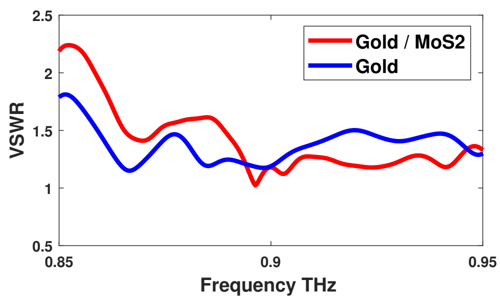

(a)

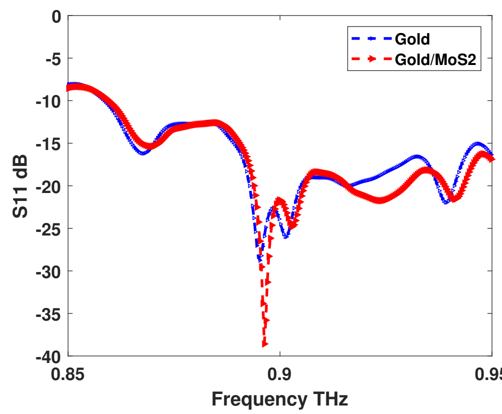

(b)

Figure 3.52: Antennas VSWR versus Frequency and Simulated S 11 profile of antenna

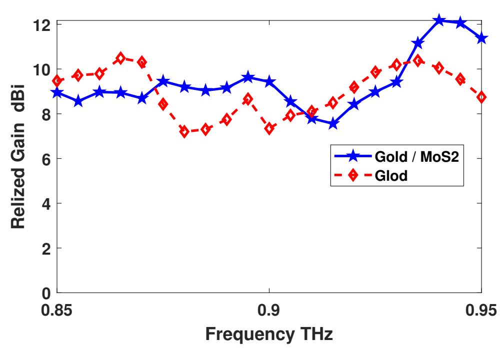

(a)

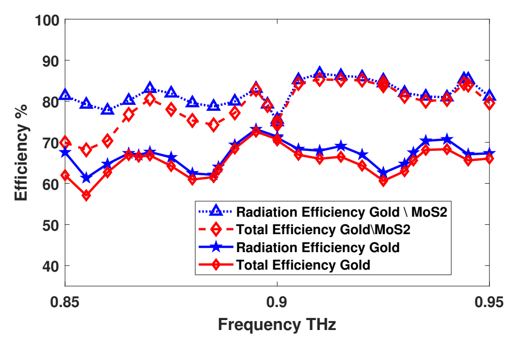

(b)

Figure 3.53: Gain and efficiency of the proposed Folded antenna.

3.13 Summary

Wearable THz antennas based on graphene have been developed and tested on three layers of human skin to meet the demands of contemporary THz systems. Because of the absorption of

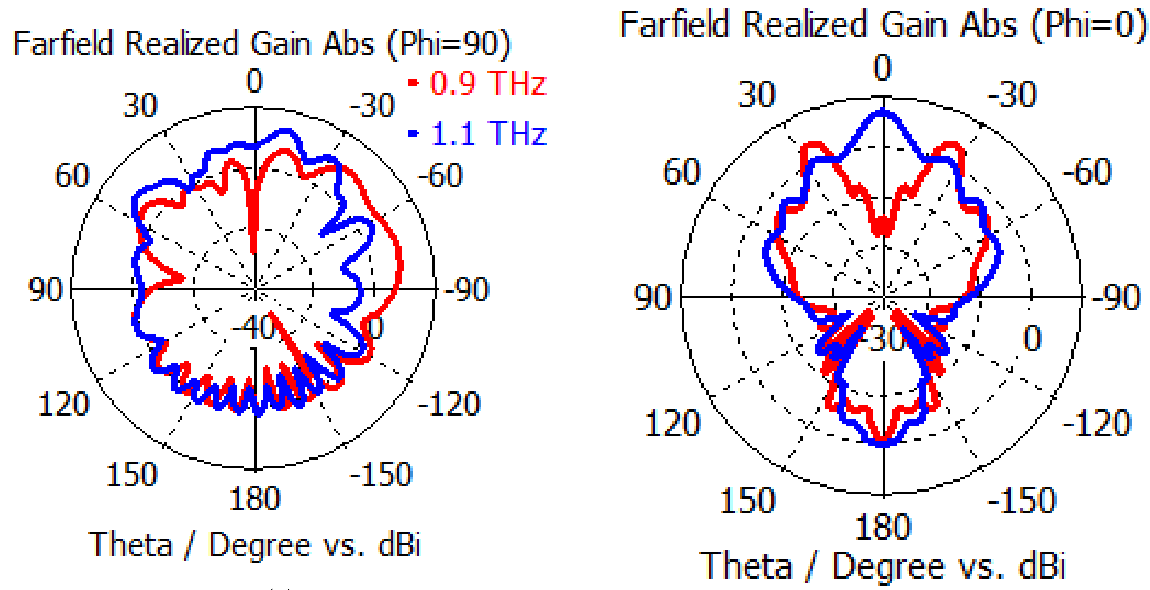

(a) (b)

Figure 3.54: H and E plane Radiation pattern of the proposed Folded antenna.

radiated energy, the antenna performance of wearable antennas will be reduced. We expect the antenna to work best at a distance of 1 or 2 millimetres from the surface of the human body. Due to human body proximity, antenna performance was impacted in terms of frequency detuning and radiation pattern distortion. The suggested design offers a number of advantages, including high radiation efficiency and simple manufacture. Poylimide film, which is widely accessible and inexpensive, was used as a flexible substrate in this study. Personal security, health and well-being monitoring, big data, and the Internet of Things (IoT) might benefit from this wearable antenna design. For short-range THz communication, graphene's exceptional electromagnetic, mechanical, electrical, and thermal capabilities have made it possible. The atomically thin profiles and exceptional electrical capabilities of graphene-based devices allow for flexible, stretchy, or even conformal features in any application. Short-range wireless body area networks (WBANs) may be a good fit for the antenna in the future.

A wearable graphene THz antenna is presented and tested on three layers of human skin to serve the wearable applications in modern THz systems to achieve high performance. Graphene has enabled the short-range communication in the THz frequency owing to its extraordinary electromagnetic, mechanical, electrical, and thermal properties. It has put itself as main platform material at THz frequency. The possibility of fabricating lightweight, thin and low-cost flexible antenna devices are the important advantages of using graphene material. Moreover, due to the atomically thin profiles and the extraordinary electronic properties, graphene-based devices are useful in designing flexible, stretchable, or even conformal aspects in any application. As wearable antennas work close to the human body, the antenna performance will be affected as a consequence, due to absorption of the radiated energy. We believe that the antenna will perform well when positioned at a distance of 1 or 2 mm from the human body surface. The antenna is regarded as a potential candidate for the future short-range wireless body area network (WBAN) Scenario.

Chapter 4

Ultra-width THz antenna arrays

The global average monthly mobile data consumption per device is expected to rise to 24 gigabytes in 2025 [175] which will lead to great strains on the mobile networks. Terahertz (THz) communications have naturally been tagged as an attractive solution to the expected bandwidth crunch as THz networks have the potential capacity in the range of several terabits per second [176–178]. However, the device technology to build sources and detectors is still in its infancy as compared to the established microwave and optical counterparts that can not be merely scaled to THz frequencies owing to numerous reasons. THz technologies have been translated into various applications that spans biomedical science and engineering [179, 180], imaging schemes [181, 182], military [183], calibration systems for microwave sensors [184], space instrumentation [185], and environmental monitoring systems [186]. Most of the aforementioned applications particularly exploit the unique interactions of water molecules with the THz waves [187]. So −called THz gap that ranges from 0.1 THz to 10 THz and this frequency range is less affected by the adverse climatic conditions like rain and fog [188].

However, with respective to the realisation of THz wireless systems, it remains a challenge to realise an ultrawideband, low−cost antenna that is scalable and easily integrated on chip [189]. In this regard, a variety of THz nano−antenna designs that are scaled versions of the microwave frequency counterparts have been recently proposed that include printed dipoles [190–192], and simple patch antennas [193]. On−chip, THz beamforming array systems that are fabricated on silicon have been also reported [194, 195]. Surface plasmon enabled enhancement of the near−field further extends the promise of dipole−type antennas for THz communications [191]. Similarly, a nanoantenna array was also developed for subwavelength focusing of the THz waves [193].

A theoretical analysis of a highly directed antenna array having 16 elements at 0.3 THz was shown in [194] with a maximum directivity of 18.1 dBi. Despite these various attractive antenna designs, the patch antenna has the advantage of low cost and relatively simple fabrication achieved through conventional semiconductor deposition techniques [189].

At THz frequencies, the substrate thickness inevitably becomes comparable to the wavelength

[196], which prevents the efficient design of the planar antenna feeding networks, due to the change in the impedance. Typically, the substrate thickness is often set in the range of two orders of magnitude below the operating frequency, so that radiation efficiency of the antenna can be improved. However, at THz frequencies, such a procedure results in extremely thin substrates which adversely affect the structural integrity of the antenna. A common practise is to place a dielectric lens, typically made of silicon below the substrate [197], which is inspired by the use of THz technology in astrophysics. However, for applications in which planar designs are preferred, such a remedial measure to enhance the substrate radiation becomes unusable. Other techniques involve the use of thin films of dielectric membranes embedded within waveguides [198]. Due to the complicated designs, such measures have not been broadly applied. The ungrounded coplanar waveguide (UCPW) feed is a viable solution to provide not only just good impedance matching with a sufficient substrate thickness, but low transmission loss, small frequency dispersion, and most importantly easy integration with the monolithic circuit designs. In addition to this, the handling of the antenna during the fabrication also becomes safer as no extra processing measures are required for the back layer of the substrate [199]. Amongst the antenna designs that yield an ultrawideband (UWB) response with an omnidirectional spatial coverage, the planar inverted cone antenna (PICA) has emerged as one of the most promising designs in the last two decades. A PICA is composed of a semicircle, which is extended into an inverted cone from the flat side. Performance−wise, the PICA is known to produce an impedance bandwidth of $20:1$ at microwave frequencies [200, 201]. Moreover, due to the flat profile, the PICA exhibits mechanical stability due to which it is increasingly being used for commercial applications that require high bandwidth in an omnidirectional way. In this work, for the first time in literature presenting a fabricated and experimentally measured, novel and simple ultrawideband omnidirectional 1×4 THz PICA array with a 37.9% bandwidth with a central frequency of 0.92 THz. The simple profile of the antenna array and excellent radiation characteristics can pave the way for realising truly UWB wireless communications in the THz frequency band.

4.1 E beam lithography

The James Watt nanofabrication facility now has a Vistec vector beam (VB) 6 ultra-high resolution (UHR) extra wide field (EWF) electron beam lithography instrument (JWNC). It is classified as a Gaussian-beam lithography tool, in which each shape is formed through a series of exposures to a focused electron beam. Schematic representation of Vistec VB6, which is primarily comprised of an electron gun, column, chamber, stage, and load lock, all of which are mounted over a vibration-isolated a plinth that houses all of the vacuum systems [202]. A cathode emission technique using a thermally assisted field emitter (TFE) source generates an electron beam using an electron gun. In EBL, an electron beam is scanned over a resist-coated surface in a preset pattern, rather than exposed via a mask [203]. The resist layer undergoes a

Nano-architecture technique	Compatible Materials	Resolution
Electron beam lithography	Silicon and conductive materials. Requires electron-sensitive resist (PMMA)	Below 10nm
Nano-imprint lithography	Silicon-based materials, metals, polymers	2-100 nm
Photolithography	Silicon-based materials, metals, polymers	Above 5 um

Table 4.1: A comparison of different fabrication techniques

chemical change as a result of the local exposure to the electron beam. The remaining stages are identical to those used in photo-lithography, except that the resist coating and developing chemicals are different. The electron cannon generates a constant stream of electrons using a thermal field emission cathode. It has a razor-sharp tungsten tip that has been coated with Zirconium Oxide. This coating creates a Schottky emitter, lowering the surface work function and facilitating electron tunnelling. The energy of the electrons is often expressed in terms of the anode accelerating voltage. Accelerating voltages of 100kV have been employed throughout this investigation [204].

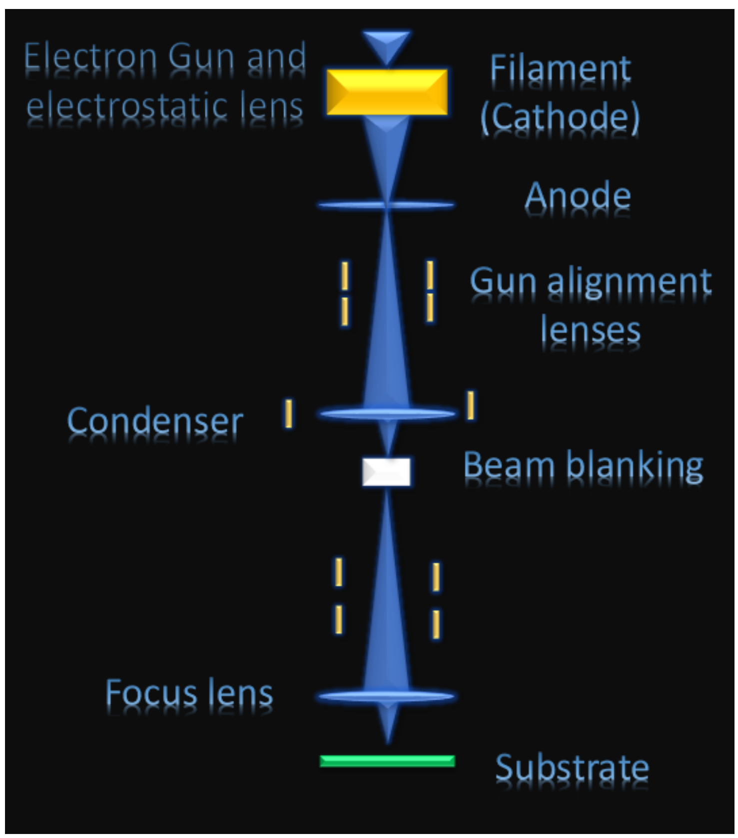

Figure 4.1: Optical system of the VB6. This entire layout is housed within the column of the tool and held at high vacuum

The beam blanker is used to turn the beam on or off selectively at a high frequency. It is composed of a series of electrostatic plates that, when triggered, significantly deflect the beam, diverting electrons away from the apertures and blocking them instead. Throughout the column, apertures are used to regulate the divergence of the beam, thereby cutting out any stray electrons. Deflection and focusing The deflection of the beam controls the angle at which electrons impact the substrate. This is accomplished with the aid of a collection of magnetic coils positioned orthogonally to the beam. The last set of coils in the optical system is the quick focus coils, which regulate the beam convergence to the substrate surface.

4.1.1 Sample submission

The L edit CAD programme is used to create patterns. Multiple configurable levels, a hierarchical cell structure, and arraying capabilities are all included. This programme enables the manipulation of features as small as nanometres and chips as large as centimetres. Table 4.2 show beam size of the ebeam lithography being used in the JWNC lab.

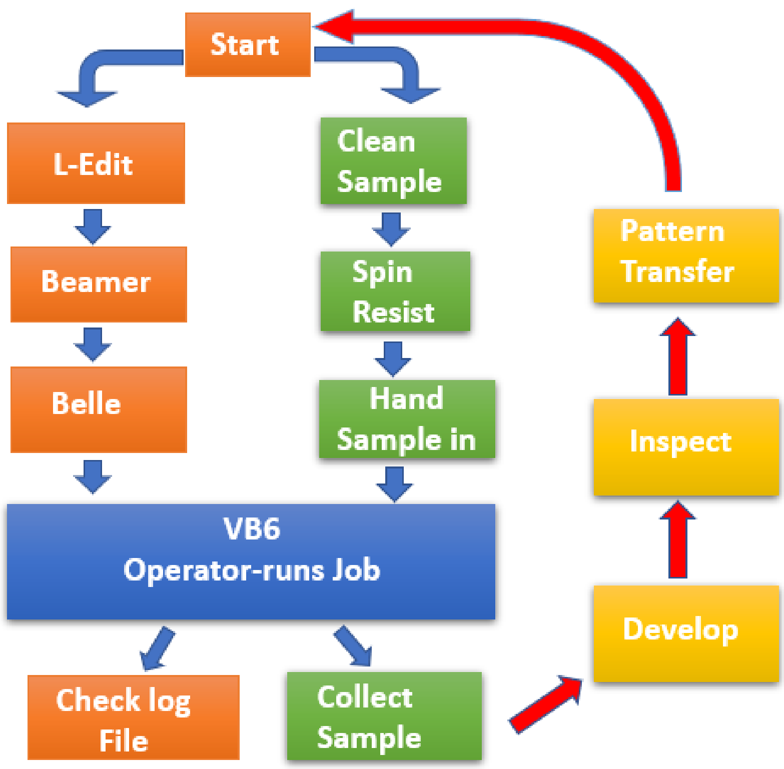

Figure 4.2: Ebeam Process Flow

4.1.2 Al wet etching

Using Al etch solution based on phosphoric acid. This etches Al in a controlled manner with approx 1um resolution. For stripping Al from the surface, eg when using it as a charge dissipation

Selected spot	Actual spot	Spot size
1nA	1.0nA	4 nm
2nA	2.1nA	6 nm
4nA	3.9nA	9 nm
8nA	8.2nA	12 nm
16nA	16.0nA	19 nm
32nA	32.0nA	24 nm
64nA	63.6nA	33 nm
100nA	131nA	45 nm

Table 4.2: The size of the Spot is governed by the beam current

layer for ebeam lithography, a weak alkaline developer is suitable, for instance CD26. Development, PMMA resist may be developed using a mixture of Methyl isobutyl ketone (MIBK) and IPA, in which the former is the active ingredient. In this work, a ratio of 1 : 1 for routine development has been used due to its speed and reasonable contrast. 2.5:1 has also been employed where higher contrast development is required.

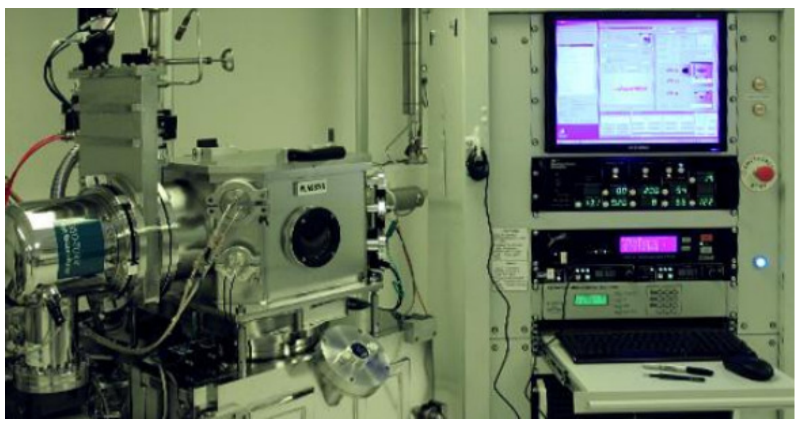

Figure 4.3: Metallization facility (Plassys 4)

4.1.3 Analysis tools

SEM Scanning Electron Microscopy has been used for the high-resolution inspection of small features. Two machines were used frequently: a Hitachi S4700 and an FEI Novasem. The former is a cold field emission microscope featuring a load-lock system for quick sample loading. The latter is capable of $ultra-high-resolution$ imaging in both high and low vacuum, and has a variety of secondary electron detectors including TLD, ETD and helix.

4.1.4 PICA antenna design

The proposed antenna design was simulated and analysed using a three$-$dimensional, full-wave commercial electromagnetics solver, dassault systemes CST Studio Suite. An array of gold-based PICAs was designed at 1 THz on a silicon substrate, having a dielectric constant, $\varepsilon_r = 11.9$ and thickness, $h = 600$um. The initial dimensions of the PICA were obtained using standard microstrip patch antenna design equations, the width and length of an equivalent patch antenna resonating at 1 THz has been calculated [205], an inverted cone was generated where the dimensions W_p and L_p were calculated using the expressions provided in [206]. In the PICA array, the antenna element spacing was set to λ at 1 THz. The resultant design was then optimised using the trust region framework (TSF) algorithm [207] included in the CST environment. The TSF algorithm searches locally for minimal points in a given region. However, based on the parameters provided to the framework, the algorithm can operate locally as well. To obtain the optimal antenna structure, a multidimensional problem in which all the physical dimensions of the PICA array were parameterised was rigorously solved using high-performance computing facilities at the University of Glasgow. The goal of the algorithm was to find the local minima for the initial values which were calculated using standard microstrip patch antenna designs [208]. The feed line dimensions, L, and W were calculated using standard microstrip transmission line based expression to obtain a characteristic impedance of 50 Ω.

Figure 4.4: One Pica Patch

The obtained calculated dimensions values were further optimised using trust region algorithm available in the CST Studio. The designed antenna structure along with the feeding network is shown in Fig. 4.5. Furthermore, the dimensions of the antenna and the feeding lines are described in Table 4.3.

The electromagnetic waves within the metallic layers can be shown by eigenmodes of the resonators. Figure 4.6 shows the surface electric current distribution of the PICA at three different operating frequencies, namely 0.75 THz, 0.925 THz, and 1.10 THz respectively, and these results show that the current reaches the tip of the PICA, causing radiation of the EM waves. At 0.75 THz, the surface electric current is strongly excited on the top surface of the gold metallic posts, whereas the current on the four side tips also contributes to the radiation of the antenna, although its magnitude is much smaller than the counterpart on the metallic posts. Besides, the electric field over the edges of the radiating aperture is also strongly excited.

In order to make the antenna resistant to corrosion and chemically stable, gold has been

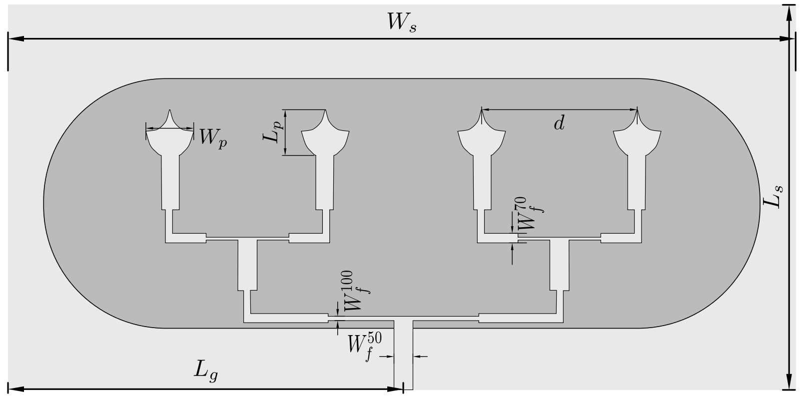

Figure 4.5: The geometry and dimensions the PICA array and the feeding network.

Dimensions	Description	Value (µm)
g	CPW feeding gap	1
L_p	Patch Length	100
W_p	Patch width	120
W_s	Substrate width	1000
L_s	Substrate length	2000
h	Substrate thickness	600
W_f^{50}	50Ω feed line width	45
W_f^{70}	70Ω feed line width	20
W_f^{100}	100Ω feed line width	9.9
d	Spacing between Antenna elements	300
L_g	Ground plane length	978

Table 4.3: The dimensions of the gold PICA array.

chosen as radiating material. In addition, at THz frequencies, gold exhibits a high electrical conductivity with a lower skin depth ($\sim$ 80 nm at 1 THz) [64]. It is easily deposited using traditional deposition techniques such as sputtering, evaporation, and electroplating with a high melting point [209]. For the fabrication of submicron structures, electron beam lithography (EBL) is utilised to transfer the pattern onto a resist layer that is precoated on the surface of a wafer. In general, a shorter wavelength is the key to achieve smaller feature sizes. With EBL nano scale THz antenna designs can be realised.

4.1.5 Antenna fabrication

The fabrication process of the proposed 1×4 PICA array was carried out at the James Watt Nanofabrication Centre (JWNC) at the University of Glasgow. The fabrication is carried out using a four-step process where the sample undergoes cleaning, after which the photoresist is spun on the wafer. After that, the design is transferred using the EBL and the last step involves the metal left off.

The unwanted gold was removed by dissolving the resist in acetone solution for 4 hours.

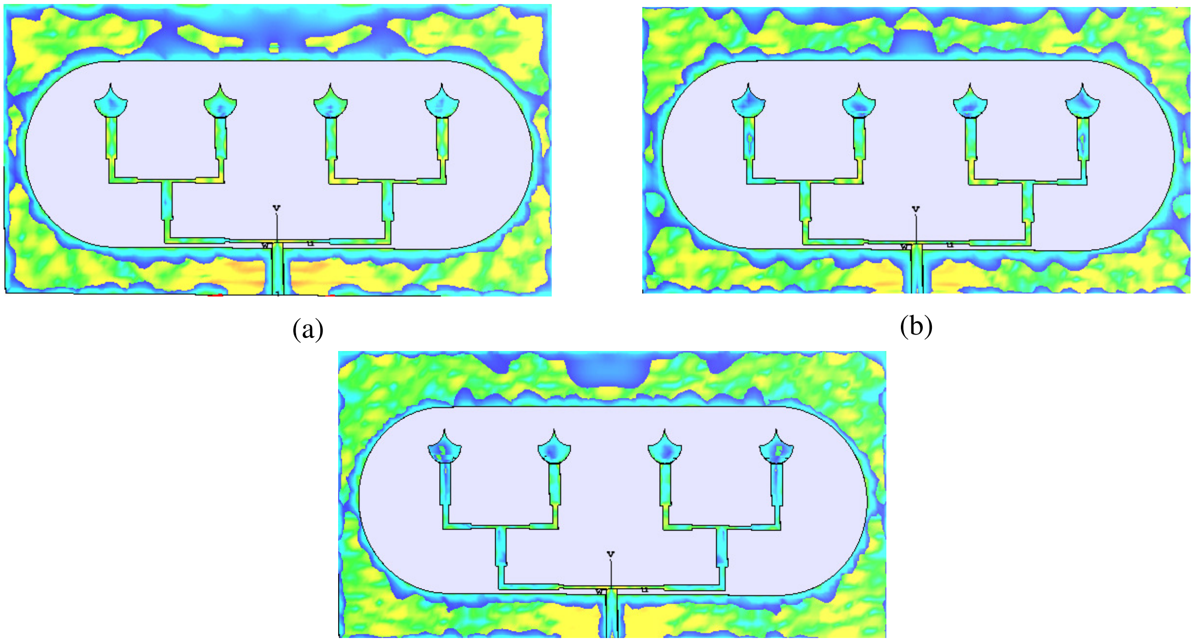

(a) (b) (c)

Figure 4.6: Visualisations of the surface electric current distribution at (a) 0.75 THz, (b) 0.925 THz, and (c) 1.10 THz.

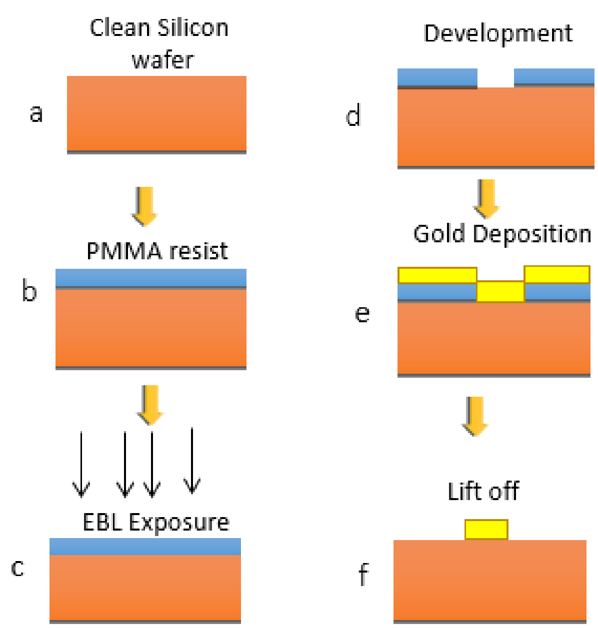

Figure 4.7: Fabrication steps

The size and geometry of the obtained fabricated structure can be ascertained from Fig. 4.7. The execution of these steps initially involved a polymethyl methacrylate (PMMA) resist which was spin coated onto the silicon substrate with a thickness of 1.2 μm. The higher sensitivity photoresist requires a lower dose which ultimately determines the exposure times. The exposure dose from the e-beam source was tested on the PMMA photoresist before the process of fabrica-

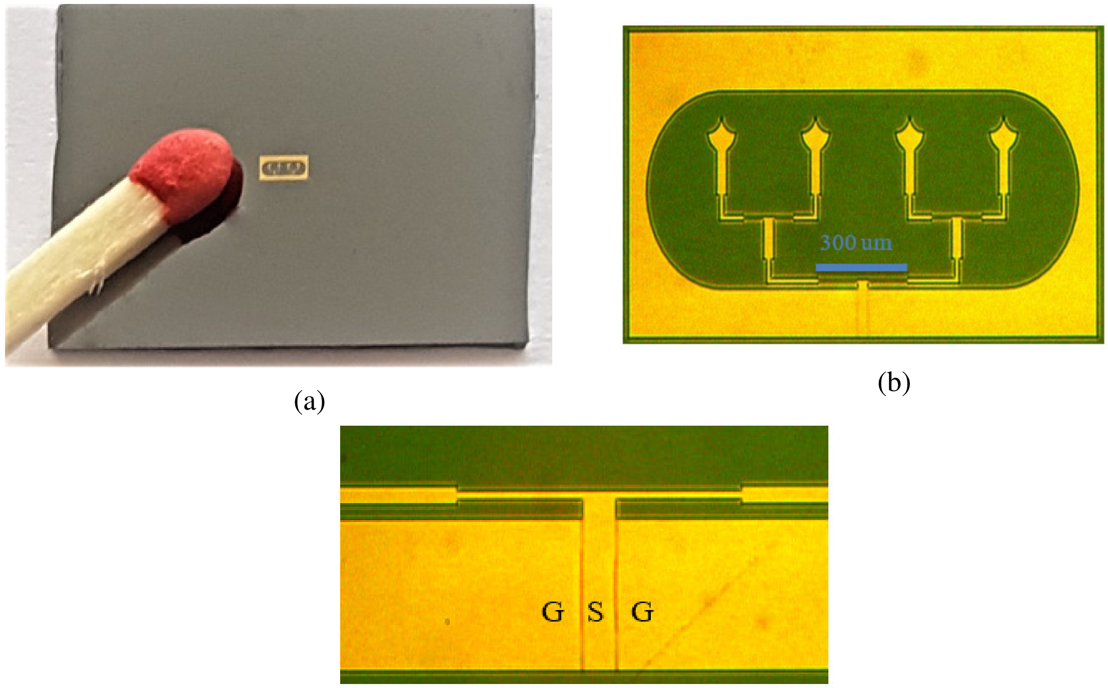

(a) (b) (c)

Figure 4.8: (a) Comparison of the size of the fabricated 1×4 PICA array with a matchstick. Photomicrographs of: (b) the array structure and, (c) the ungrounded CPW feeding network.

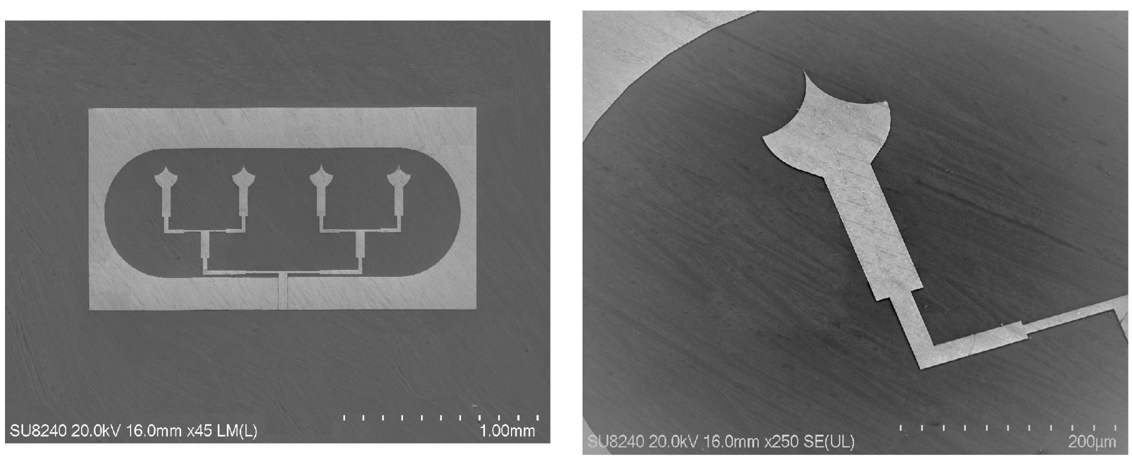

(a) (b)

Figure 4.9: High-resolution images obtained using a FESEM of: (a) Array structure and, (b) the feeding transmission line for the PICA array.

tion and it was found that 650 $\mu\text{m}/\text{cm}^2$ dose was optimum to obtain a good resolution. A 2.5 : 1 developer was used to develop the PMMA for 30 s and rinsed afterwards with isopropyl alcohol for 20 s. Lastly, a 500 nm layer of gold was deposited on the developed wafer.

4.1.6 THz on-wafer measurement

Automated or semi-automated probe stations are not simply an evolution of manual probe stations. In academic and industrial labs, manual probe stations are typically employed for entry-level characterization, but semiautomatic and completely automated probe stations alleviate the load of large volume characterization in production processes. As seen in Figure 4.10, the semiautomatic probe station has a greater mechanical complexity due to the fact that it must accommodate all the stepping motors and associated control wire necessary for automated probe station movement. Additionally, for comfortable operation, the digital microscope used to see the integrated devices on the wafer is linked to display monitors. The microscope and probe station software offer a greater degree of capability than is possible with an optical examination alone.

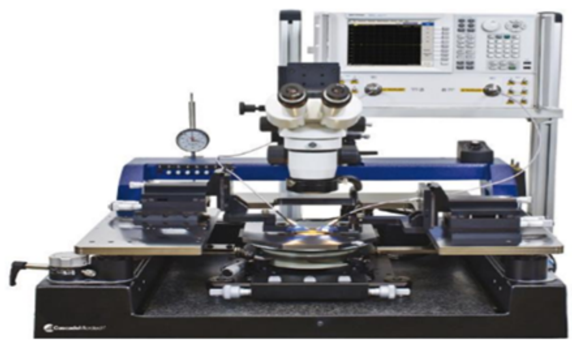

Figure 4.10: Probe Station for on Wafer Measurement

4.1.7 CPW THz probes

Probes are another critical type of equipment used for on-wafer measurements [210]. There are several probe kinds available, depending on the type of excitation signal (from DC to millimetre wave), the design of the probe tip, and the probe body shape. This discussion will concentrate on RF probes [211]. A radio frequency probe is basically the interface between the silicon wafer and the coaxial transmission lines that carry signals from the instruments to the wafer and vice versa. Screws are used to secure the probe body to the probe station positioner [212]. Once the probe is secured to the probe station, a coaxial cable is added to its connection to link it to the instruments. Between the connection and the probe tip, a precise coaxial cable is produced inside the probe body [213]. Absorber materials are used to reduce undesired electromagnetic mode propagation on various portions of the probe. The coplanar waveguide (CPW) is the most often used probe tip structure for RF probes, since it can be tailored to match the characteristic impedance of 50 throughout a wide frequency range. Due to the core signal strip being flanked by two ground planes, the symmetric CPW probe tip design is often referred to as ground-signal-ground (GSG) [214].

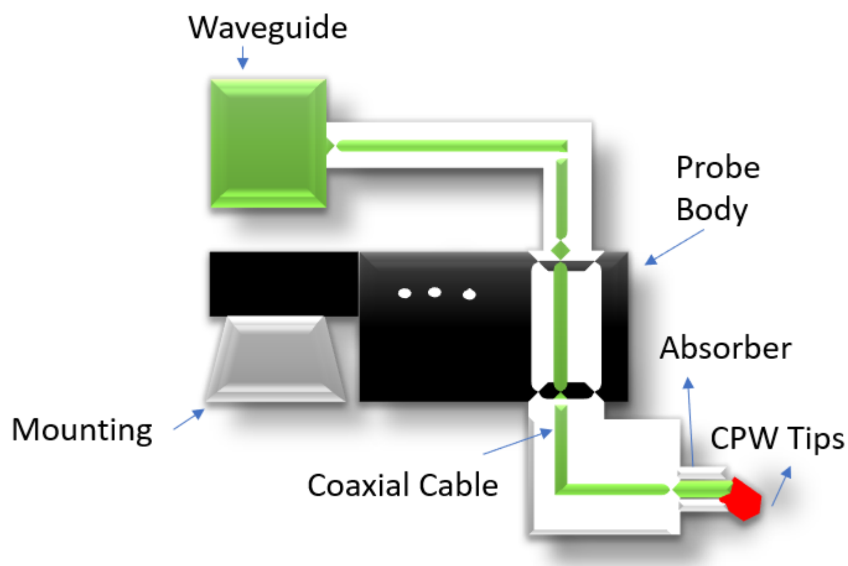

Figure 4.11: THz Probe

As per the authors knowledge, the fabricated on-chip antenna was measured in the THz frequency band, for the first time in the literature, where a Cascade Microtech THz wave vector network analyser (VNA) coupled has been used with a Virginia Diodes Inc. The Model 1100B Picoprobe sets new standards in microwave probing performance. Benefiting from coaxial techniques, which have inherent low loss and low dispersion characteristics 4.12. With its individually spring loaded, Beryllium-Copper tips, the Model 1100B Picoprobe provides reliable low resistance contacts. This reliable low resistance contact is one of the keys to providing highly repeatable measurements. The Model 1100B Picoprobe also allows direct viewing of the probe tips for accurate positioning.

It is critical to maintain the planarity of the RF probe tips in order to conduct accurate calibration and measurements. The mechanical procedure of mounting the RF probes on the positioners and connecting the coaxial wires to the probe connection puts stress on the probe body [215]. As a consequence, the probe may be mounted at an angle on the positioner, causing the probe tips to be at different heights. As a result, before calibrating an on-wafer measurement system, we must first confirm the planarity of our probes. The coplanar GSG probe is surrounded by two ground tips, which provide a current return channel for the AC signal propagation. This is a necessary assumption for accurate calibration using on-wafer standards. Inconsistent and ultimately incorrect readings will result from a misaligned probe that lacks planarity and has poor contacts for some of the probe tips on the pad metalization [216]. To prevent this, it is our responsibility to inspect the probe tips for planarity after they are installed on the positioner. Having a distinct location for the contact substrate enables us to monitor the planarity of the contact substrate between successive measurement cycles, ensuring constant probe tip planarity [213]. The planarization procedure begins by advancing to the contact substrate location and inserting the probes into the field of view of the microscope.

(a)

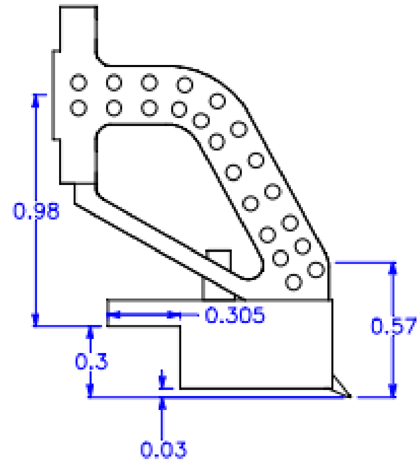

(b)

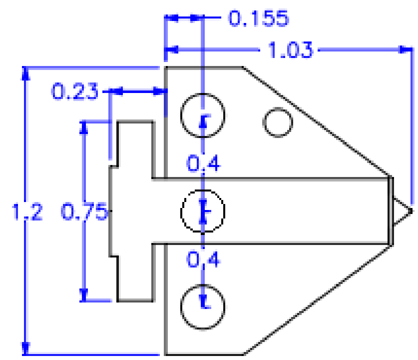

(c)

Figure 4.12: (a) Model 1100B Picoprobe GSG-25-BT. The probes also have a 3 hole mounting adaptor which will fit standard microwave probe stations. (b) and (c) Model 1100B dimensions in inches

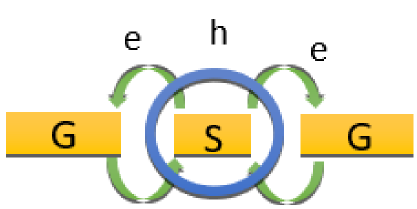

(a)

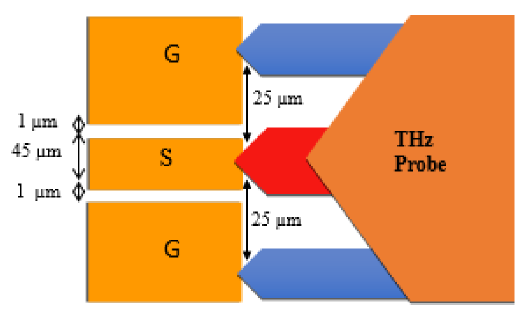

(b)

Figure 4.13: The ungrounded CPW feeding network. (a) Illustration of the electric and magnetic field distributions around the ungrounded CPW and, (b) schematic of the probe measurement contact with the central signal transmission line (S) and ground plane (G).

After elevating and securing the probes, we focus the microscope on the contact surface to get a crisp view of the metalization on the substrate. By gradually and carefully lowering the first probe, we should begin to get a better view of the probe tip region as the probe is lowered and moves into the microscope focus plane. By lowering the probe further using the positioner z-height manipulator, a first landing of the probe tips has been achieveed. Whereas the maximum reflection loss is around 20 dB.

4.1.8 Calibration substrates

For on-wafer measurements, a calibration substrate is commonly a ceramic substrate with printed metal patterns referred to as calibration standards [217]. The manufacturer has precharacterized the electrical performance of those standards, resulting in a set of electrical metrics that are employed throughout the calibration process. For optimal calibration, the arrangement of those standards must match the coplanar geometry of the probes in terms of pin configuration (e.g., GSG, GS, GSGSG) and probe pitch [218]. Calibration standards are available in a number of forms based on the design of the probe tip, its pitch, and its operating frequency [219]. The calibration standards are used as reference devices during the on-wafer calibration process, thereby relocating the electrical reference plane to the probe tips [213]. As seen in Figure 4.14, the patterns created on the calibration substrate may be classified as OPEN, SHORT, LOAD, or THRU standards. Additionally, many transmission lines are included on the calibration substrate for verification reasons, serving as post calibration verification devices.

4.2 On wafer measurement results

The complete measurement setup is illustrated in Fig. 4.14, which was configured in the Metamaterials Engineering Laboratory in the University of Birmingham. The THz probe used offers a low insertion loss, i.e., $<$ 1.5 dB with good sample visibility. The VNA was calibrated for 1-port S-parameter measurement using the short-open-load-thru (SOLT) calibration process on a cascade impedance substrate standard. The simulated reflection coefficients of the single element and the 4$-$element array as well the measurement results of the PICA array are shown in Fig. 4.15, which shows the excellent antenna performance as the whole response is below the 10 dB range. The difference between the single antenna and array response is attributed to the mutual coupling amongst the elements of the array.

Moreover, both the measurement and simulation results exhibit good agreement with each other, and the disparity is attributed to the unpredictable reflection from the surroundings of the experimental setup. In addition, the antenna was fabricated on a carrier wafer which was kept larger than the simulated substrate to ensure convenient handling of the fabricated antenna, resulting in a slight impedance mismatch with the feeding network. This can be observed by

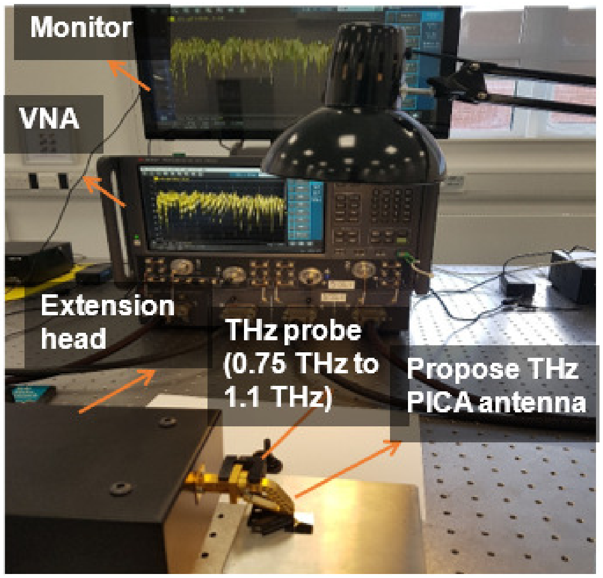

(a)

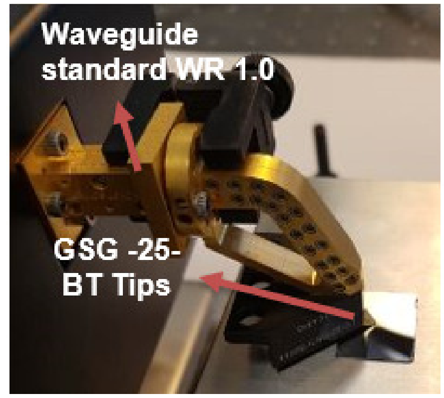

(b)

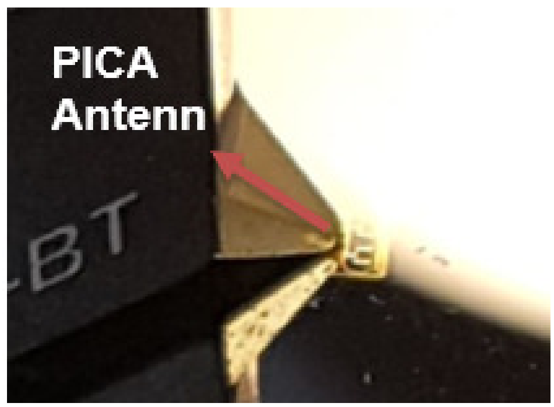

(c)

Figure 4.14: The experimental setup used to measure the scattering parameters. (a) Eye−view of the setup, (b) a GSG −25− BT THz probe (0.75 − 1.10 THz) contact location and, (c) placement of the probe on the PICA.

a series of ripples that can be seen in the measured scattering response. Figure 4.17 shows the simulated antenna performance in terms of the antenna radiation efficiency and the gain achieved by the array in the operating frequency range. It can be seen that the radiation efficiency of the antenna is maintained above 75 %. Although, this is lower as compared to antenna designs at microwave frequencies where the radiating element acts nearly as a perfect electric conductor, the conductivity of gold at THz frequencies is complex valued where the imaginary part contributes to losses.

Further investigations in which a substrate with a lower dielectric constant is used, can improve the radiation efficiency of the designed antenna. Other performance parameters such as the antenna gain and directivity are shown in Fig. 4.17, which indicates a high realised realised gain in the range of 12.5-16 dBi.

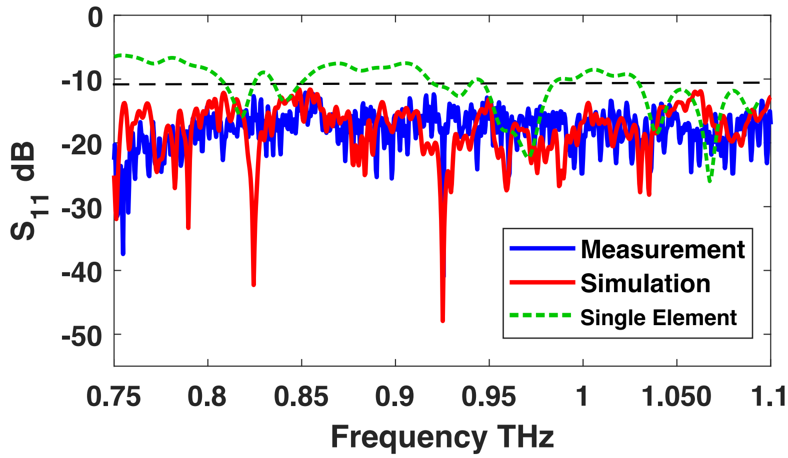

Figure 4.15: Measured and simulated reflection coefficient of the 1×4 PICA array array.

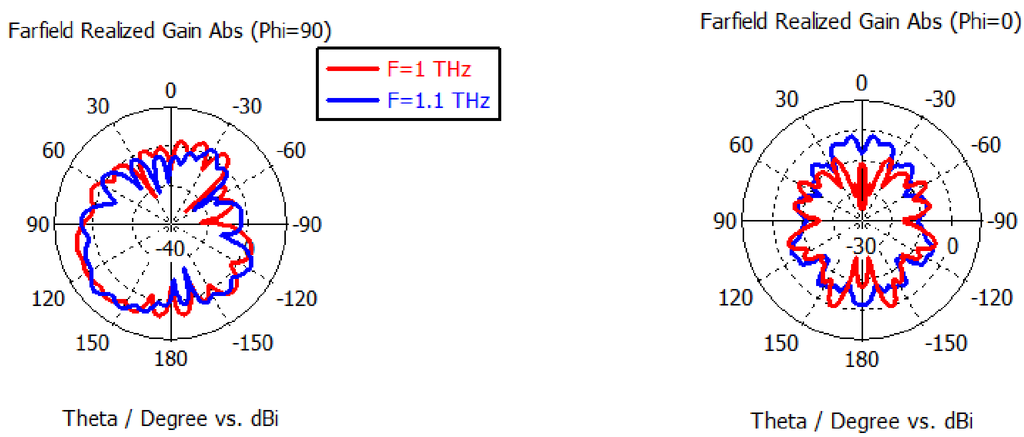

(a) (b)

Figure 4.16: Simulated radiation pattern of the proposed antenna array at different frequencies throughout the operating band. $f = 1.0$ THz, and $f = 1.10$ THz

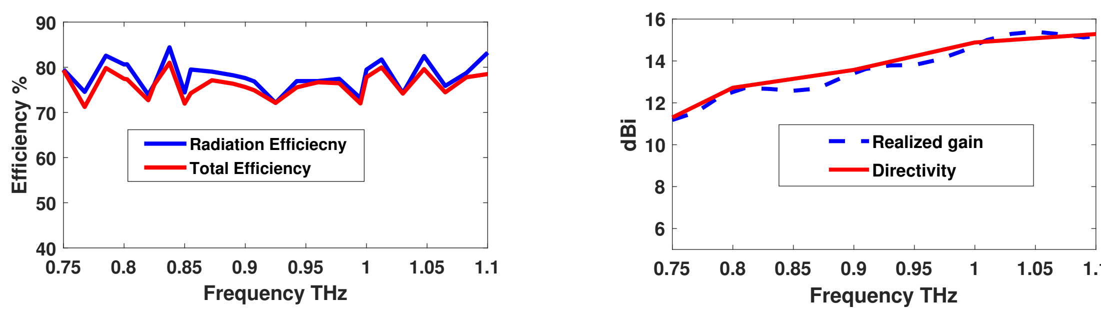

(a) (b)

Figure 4.17: Simulated results of the 1×4 PICA array, where (a) the radiation and total efficiency is shown and in, (b) the realised gain.

Figures 4.18 and 4.16 present the simulated radiation patterns of the designed antenna array at 0.75THz, 0.925THz, and at 1THz and 1.10THz respectively. The radiation patterns are pre-

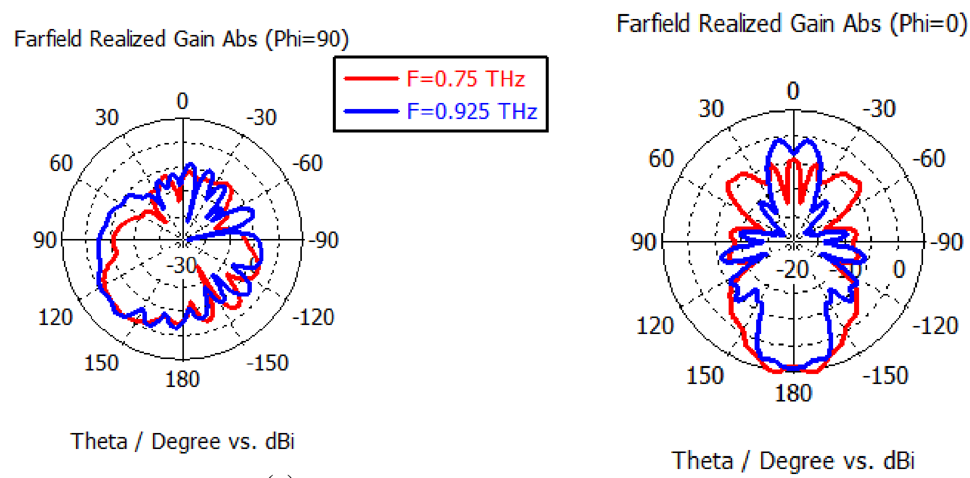

(a) (b)

Figure 4.18: Simulated radiation pattern of the proposed antenna array at two frequencies, 0.75THz, and 0.925THz.

sented at E− and H− planes. Due to the large dielectric constant of the silicon substrate, most of the radiation is directed towards the substrate. This is a common problem with antennas fabricated on high dielectric constant substrates, which at THz frequencies is often circumvented by using a hemispherical lens. The sidelobe level is increased and the maximum sidelobe is observed at 1.10 THz. Therefore, the ripples in the radiation pattern may lead to a degradation in the antenna performance which is mainly caused by metal loss and skin depth effect. In Figs. 4.16 and 4.18, the radiation patterns show high main lobe magnitudes along with lower backlobe levels.

PICA antenna has been designed and fabricated using a gold-based 1×4 planar inverted cone antenna array operating in the terahertz (THz) frequency range of 0.75 - 1.10 THz. Fabrication of the structure was accomplished by the use of basic and widely accessible metal deposition processes. It was necessary to excite the antenna using an ungrounded coplanar waveguide feeding line. The suggested THz antenna design is the first case in which the scattering response has been measured for a THz patch antenna. The design achieved a measured $-10dB$ impedance bandwidth of 400 GHz at the centre frequency of 0.925 THz. In addition, antenna performance factors such as radiation efficiency and gain are shown to be excellent. The concepts and methods outlined in this work will serve as a springboard for future research into the development of THz frequency ultrawideband antennas that will allow for faster wireless communication.

4.3 Flexible PICA antenna arrays based on Graphene

Graphene is not only the lowest thickness nanomaterial yet discovered, but additionally, graphene is the strongest nanomaterial (flexible strength $E \approx 1.01$TPa, greatest strength $\sigma \approx 130$ GPa)

[220]. Furthermore, graphene is nearly entirely transparent material, absorbing 2.3% light pass through it [221]. Graphene theoretical specific surface area is 2630 m2 g − 1 and thermal conductivity is 5300 W m − 1 K − 1, which is greater than carbon nanotube and diamond thermal conductivity. Its electron mobility is 15,000 cm2 V − 1 S − 1 at 300k, which is higher than carbon nanotubes and silicon crystal [222]. However, the resistivity of graphene is 10 − 6Ωcm, lesser than silver and copper which is make graphene the lowest resistivity material ever discovered. Graphene is supposed to be successful in developing electronic gadgets with low thickness and extreme conductive velocity, built on graphene electrical resistivity and high velocity of electrons [223]. Graphene is not only the lowest thickness nanomaterial yet discovered, but additionally, graphene is the strongest nanomaterial (flexible strength $E \approx 1.01$TPa, greatest strength $\sigma \approx 130$ GPa) [220]. Furthermore, graphene is nearly entirely transparent material, absorbing 2.3 % light pass through it [221]. Graphene theoretical specific surface area is 2630 $m^2\ g^{-1}$ and thermal conductivity is 5300 $W\ m^{-1}\ K^{-1}$, which is greater than carbon nanotube and diamond thermal conductivity. Its electron mobility is 15,000 $cm^2\ V^{-1}\ S^{-1}$ at 300 k, which is higher than carbon nanotubes and silicon crystal [222]. However, the resistivity of graphene is 10-6 Ωcm, lesser than silver and copper which is make graphene the lowest resistivity material ever discovered. Graphene is supposed to be successful in developing electronic gadgets with low thickness and extreme conductive velocity, built on graphene electrical resistivity and high velocity of electrons [223].

4.4 Graphene material in the market

While the majority of the excellent physical features of graphene have been investigated, the development of technology that links academic to industrial manufacture remains a priority. Although different research efforts on graphene have been continuing for the better part of the past century, a monolayer of graphene was extracted from bulk graphite a decade ago using mechanical cleavage [96]. Peeling adhesive tape off the bulk repeatedly until just a monolayer of graphene remains is the procedure. Although the so-called Scotch tape technique does not need specialised laboratory equipment, it has traditionally produced the finest quality graphene flakes and fueled several laboratory discoveries. However, monolayer graphene flakes have been confined to hundreds of micrometres in diameter [96], necessitating extensive identification under the microscope.

Graphene may be manufactured in continuous sheets from the bottom up using sublimation of SiC or chemical vapour deposition (CVD) with hydrocarbon precursors. For some years, it has been known that graphite may be produced by heterogeneous catalysis on transition metals. Apart from this, the first publication on CVD synthesis of few-layer graphene (FLG) appeared in 2006 [224]. CVD bottom-up synthesis has developed since then into a scalable and dependable process for producing large-area graphene. This approach has been used to show the synthesis of large-area, high-quality graphene [225] [226] [227]. At the moment, the creation and development of high-quality, large-area CVD graphene on catalytic metal substrates is of basic and technical relevance. Due to the polycrystalline nature of the large-scale graphene films produced so far, the research effort is focused on controlling the domain size, the number of graphene layers, the density of grain boundaries, and the defects [228] [229]. To achieve the promise of graphene materials as graphene-based applications, it is evident that such issues must be resolved, avoiding errors in produced devices. However, the production of high-quality continuous CVD graphene demands stringent process control. Significant efforts have been undertaken over the last decade to scale up the manufacture of high-quality CVD graphene. Numerous research groups established roll-to-roll CVD techniques for the production of graphene. Producing high-quality CVD graphene with a Raman peak intensity ratio of less than 0.065 [230] [231].

4.4.1 Graphene antenna fabrication technique using Ebeam

The fabrication process of the optimised transfer method on flexible and transparent substrate can be seen in Fig.4.19. A hybrid THz antenna design with three layers of structure ,Ti, Au, graphene, and flexible substrate is investigated here for wearable applications. In this design, two different radiation elements have been used, namely, graphene and gold. Graphene is used for efficiency enhancement and traditional metal (Gold) is used as a conducting material with sufficient thickness ($> 500\mu$m) for fabrication and measurement. Combined, these two materials give an additional degree of design freedom by manipulating the shape and structure and can help address the challenges in fabrication and measurement.

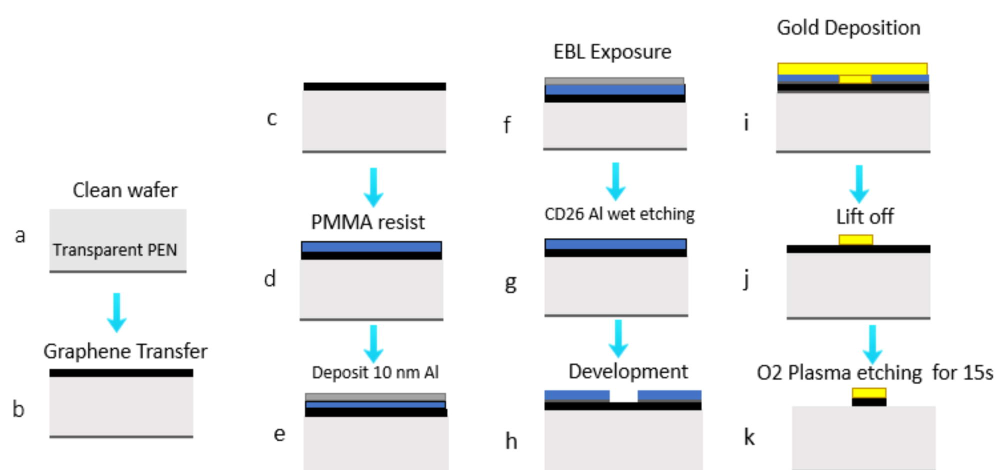

Figure 4.19: Schematic illustration of the main graphene fabrication steps in the process

The effect of graphene on the antenna radiation characteristics in the vicinity of the human body is also presented and analysed. The design procedures of hybrid antenna based on graphene/gold are schematically summarized in Fig. 4.24. The proposed antenna is designed using CST Studio 2018 and simulated at room temperature 293 K. The substrate material supervises the variation in radiation qualities of the graphene antenna. PEN is used as the substrate with thickness of 20 μm dielectric constant, $\varepsilon_r = 2.2$, loss tangent, $\tan\delta = 0.0009$. Coplanar CPW line is designed for on wafer measurements (ground - signal - ground probe). The method presented here provides the best results for transferring graphene on both flat Si wafers and PEN substrate while maintaining a minimum number of steps.

In wet etching, the ions are in liquid form during the wet etching process. In this case, etching is confined to chemical interactions and does not benefit from the additional physical effect of accelerated ions travelling perpendicular to the path of etching. Again, metal layers have picked for which the etching chemistry is well-established and readily accessible in JWNC facilities. Wet etching has a limitation in terms of the feature sizes that can be reached in contrast to dry etching. Wet etching, on the other hand, offers numerous benefits over dry etching: Affordability, Ease of usage and Extensive selection of easily etchable metals.

The primary disadvantage of this method of etching is that the chemical removal of metals is not restricted to a perpendicular direction but also includes a large parallel (or horizontal) component. This is often seen as a thinned-out appearance of the remaining features. The degree of thinning is dependent on the thickness of the metal layers, and some control over this effect may be applied during the metal deposition step. Where the aspect ratio of the features to be resolved is less than 10: 1 wet etching is a fast, efficient, and highly reliable procedure.

4.4.2 CVD graphene transformation

The typical technique of growing graphene by CVD utilises substrates that are technologically incompatible, necessitating a subsequent transfer operation. The transfer procedure is shown in Fig. 4.20 and 4.21

Release

Slowly immerse the sample in deionized water (if the sample has been kept for a while, putting the Easy transfer in the water first and then performing the release) while separating the sacrificial layer graphene from the support film. Remove the polymer sheet after the sacrificial layer graphene is floating.

Transfer

In the water, the sacrificial layer/graphene will float. To deposit it on a chosen substrate, immerse the desired substrate in deionized water and fish the sacrificial layer/graphene from underneath. Tilting the substrate 45° is another possibility.

The sacrificial layer graphene substrate can have taken out and let it dry for 30 minutes in the air. it is recommended to annealing the samples in a hot plate at 150c for 1h. Finally, before

Table 4.4: CVD Graphene Specification

Growth Method	CVD synthesis
Transfer Method	Clean transfer method
Quality Control	Optical Microscopy & Raman checked
Appearance (Color)	Transparent
Transparency	$> 97\%$
Appearance (Form)	Film
Coverage	$> 95\%$
Number of graphene layers	1
Thickness (theoretical)	0.345 nm
AFM Thickness (air RT)	< 1 nm
Electron Mobility on SiO_2/Si	$= 1500\ \mathrm{cm2/V \cdot s}$
Sheet Resistance on SiO_2/Si (Van der Pauw)	$450 \pm 40\mathrm{Ohms/sq} \cdot (1\ \mathrm{cm} \times 1\ \mathrm{cm})$
Sheet Resistance on Quartz (Van der Pauw)	$360 \pm 50\mathrm{Ohms/sq}(1\ \mathrm{cm} \times 1\ \mathrm{cm})$
Sheet Resistance on PET (Van der Pauw)	$580 \pm 50\mathrm{Ohms/sq}(1\ \mathrm{cm} \times 1\ \mathrm{cm})$
Grain size	Up to 20μm

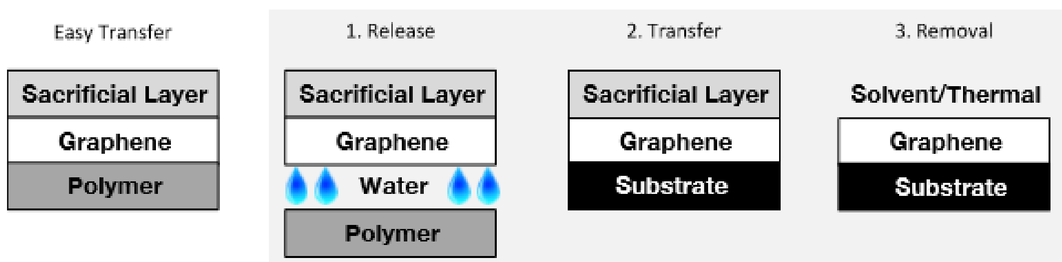

Figure 4.20: Schematic illustration of the main transfer steps in the process

Figure 4.21: Transfer steps in the process in the lab

the removal of the sacrificial layer, store it under vacuum for at least 24h to avoid detachment of the graphene from your substrate.

4.4.3 Raman spectroscopy and SEM of graphene

Raman spectroscopy data measured from a transferred graphene layer on a hydrophilic Si/Sio substrate can be seen in Fig 4.22. The 2D, G peaks are very clear and a small D peak is easily observable meaning that there is some disorder in the atomic structure of graphene. Raman spectroscopy over various areas of the transferred graphene layer showed excellent uniformity with very small variations in the measured spectra. In some areas the Raman spectrum had intensity fluctuations due to the existence of wrinkled areas which are known to cause height

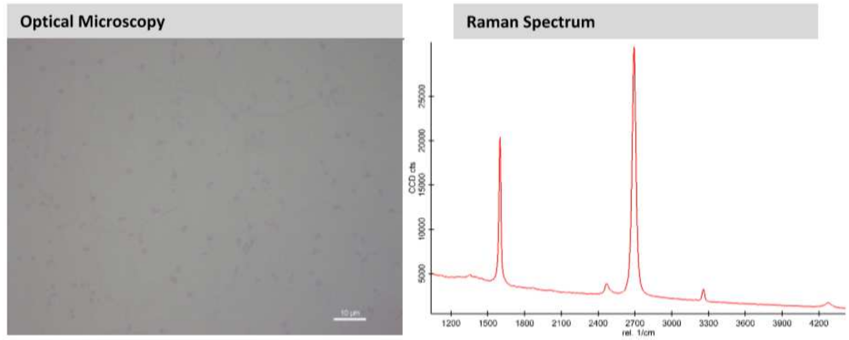

Figure 4.22: Raman spectroscopy data measured from a transferred graphene layer on a hydrophilic Si/SiO substrate

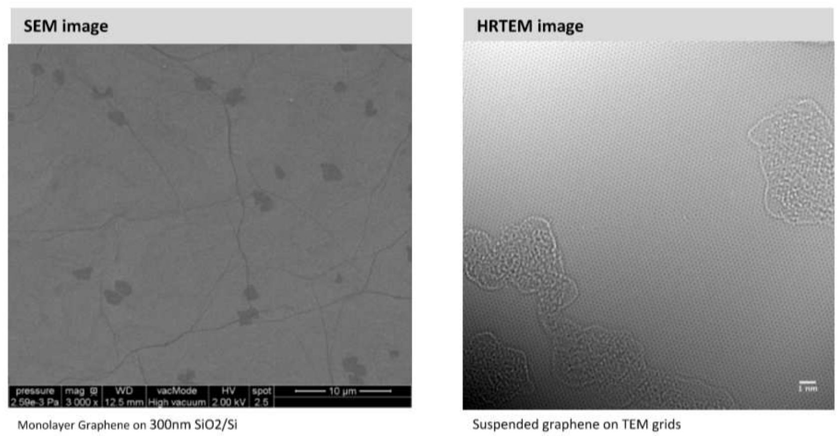

Figure 4.23: SEM and HRTEM images of the graphene sample

variations in the G and 2D bands. Not much variation was observed in terms of peak position, peak intensity, and FWHM for different areas of the sample.

4.4.4 Graphene etching

Plasma-based dry etch techniques have become a widely accepted standard within the semiconductor industry. This is due to its ability to scale up for the industrial application and its directional etching ability, thereby enabling the highly accurate direct translation of the photoresist pattern with a high aspect ratio. Reactive ion etching (RIE) is a plasma−based dry etch process. RIE system consists of the generation of plasma between two parallel plates (one biased and the other grounded) by radio frequency (RF) voltage. Plasma is generated by the dissociation of the source gas by the RF field under vacuum, resulting in the formation of ions, excited neutrals, and electrons, which play a key role in the etching process. The high mobility electrons in plasma respond rapidly to the changing potential and this results in the formation of the negative potential at the substrate surface.

Parameters	Value
Gas	O_2
Pressure (mTorr)	50
Gas flow	50
RF Power (W)	300
Temperature ($^{\circ}C$)	20
Etch time (s)	15

Table 4.5: O_2 plasma parameters for graphene etching

4.5 Serial feed antenna arrays based on graphene

The THz electromagnetic spectrum provides a number of advantages for wireless communications. Since the previous decade, the bandwidth needs for wireless communications have been constantly growing. The only option to ensure enough transmission capacity is to use transmission bands with higher carrier frequencies. THz spectrum enables higher bandwidth and data rate transmission. Wireless communications systems now available have bandwidths of a few GHz and data transfer speeds of up to 1 Gbps. Due to the small bandwidth of the microwave spectrum, achieving 10 Gbps data speeds is very challenging. The data rate is increased from 10 to 100 Gbps by increasing the carrier frequency from 100 to 500 GHz.

The potential of transmitting at a high data rate is made possible by the enormous bandwidth available in the THz band. THz communication has great promise for wireless communication systems, especially those operating in the short-range interior environment. There are many ways to feed a microstrip array, including serial feeding, parallel feeding through corporate feed, spatial combiners, reflect arrays, and lens antennas. Typically, the first two approaches are the easiest, since they can be implemented on the same layer as the array, allowing for more optimization of the antenna weight, thickness, and cost, but the others need more sophisticated three-dimensional structures. However, when the feed is coplanar to the array, resistive and radiation losses must be considered, since they restrict the gain and radiation pattern [232].

The parallel feed and the series feed are distinct in a number of ways. For example, the parallel feed gives a greater bandwidth, typically 10% of the operating frequency, while the series feed provides bandwidths between 1% and 3%. The downside of parallel feeding is that it results in increased ohmic losses due to the additional area required for parallel feeding systems. Radiation losses are also increased owing to the number of discontinuities required in the parallel design. Typically, a combination of both forms of feeding is employed to create an acceptable trade-off between bandwidth, radiation loss, ohmic loss, and available space [233].

4.5.1 Antenna design

As the most fundamental and important active device component in contemporary electronics, searial antenna arrays have been designed with an emphasis on size and power consumption reduction. Additionally, researchers are looking for substitute materials for conventional materials such as silicon, which is primarily used in the fabrication of conventional electronic devices, because fabrication constraints in order to achieve smaller physical dimensions result in low device packing densities. Due to the mechanical stiffness of typical metallic antennas, their use to flexible electronic systems is limited. As a result, flexible substrates have received much research quantity.

Figure 4.25a and b show the geometry and parameters of the proposed co-planar waveguide (CPW) fed antenna. The antenna design is simulated at room temperature (293 K). The antenna design has the dimensions of 260 µm by195 µm by 0.35 nm, with one layer of graphene, and consists of a graphene-based rectangular patch with a feedline 34 µm by 100 µm by 0.35 nm. PEN 3006, having a dielectric constant of $\varepsilon_r = 2.2$, and loss tangent, $\tan\alpha = 0.0025$ is used as substrate with a thickness of 175 µm.

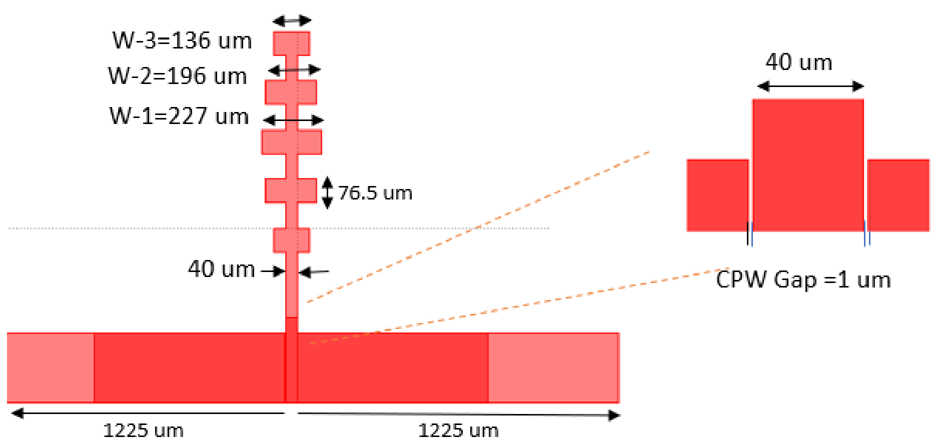

Figure 4.24: CPW Antenna dimensions

4.6 Fabrication

The antenna was then built with a tuning stub using an electron beam (e-beam) lithography method. To aid the liftoff process, an appropriate undercut was formed utilising a bi-layer e-beam resist system composed of polymethyl methacrylate (PMMA). The first layer was around 1200 nm thick. Following that, a second layer of 10% PMMA 2041 was spun at 5000rpm and baked for two minutes at 143°C. The second (top) PMMA layer was 100 nm thick. The spun PMMA layers were then exposed using the Vestec VB6 beam writer through e-beam pattern writing. A 1:1 combination of methyl isobutyl ketone (MIBK) and isopropyl alcohol was then

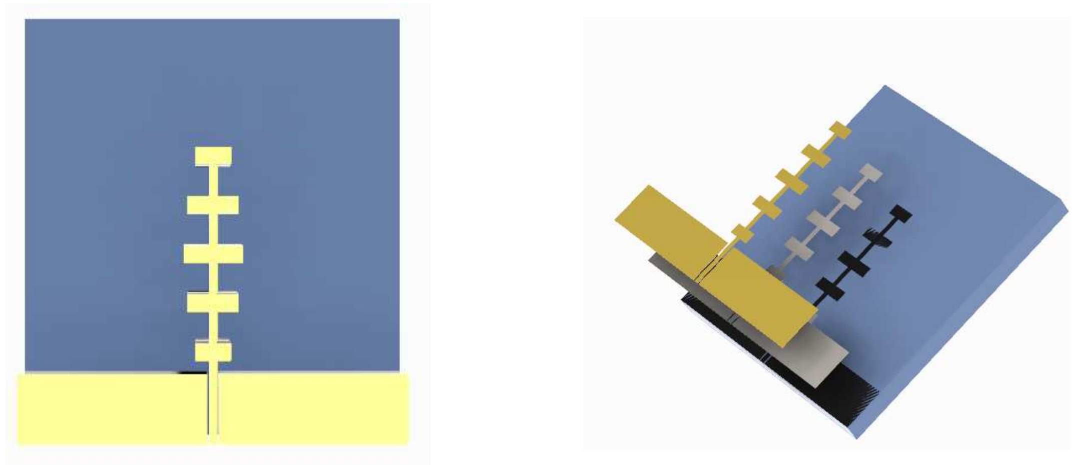

(a) (b)

Figure 4.25: Design Antenna Arrays Structure

used to develop the exposed PMMA (IPA). Due to the fact that the bottom layer is more susceptible to the ebeam dosage than the top layer, an undercut profile is generated. Finally, using an electron beam evaporator, a Ti/Au (10nm/450nm) metal scheme was deposited followed by lift-off in acetone. Ti gas been used which can provide very low specific contact resistance.

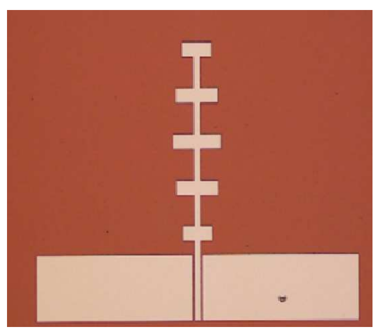

Figure 4.26: Pattern transfered on the substrate

4.7 Results ant discussion

The simulated reflection coefficients of the the 5-element array shown in Fig.4.30, which shows the excellent antenna performance as the whole response is below the -10 dB reflection range. A good efficiency of 88 % presented at targeted frequency band. In addition, the radiation efficiency of the designed antenna can further be improved by increasing the conductivity of the graphene film by applying an external voltage.

Figure 4.32 shows the surface electric current distribution of the serial arrays antenna at three different operating frequencies, namely 0.8 THz, 0.925 THz, and 1.10 THz. At 0.75 THz, the surface electric current is strongly excited on the top surface of the gold metallic posts. The

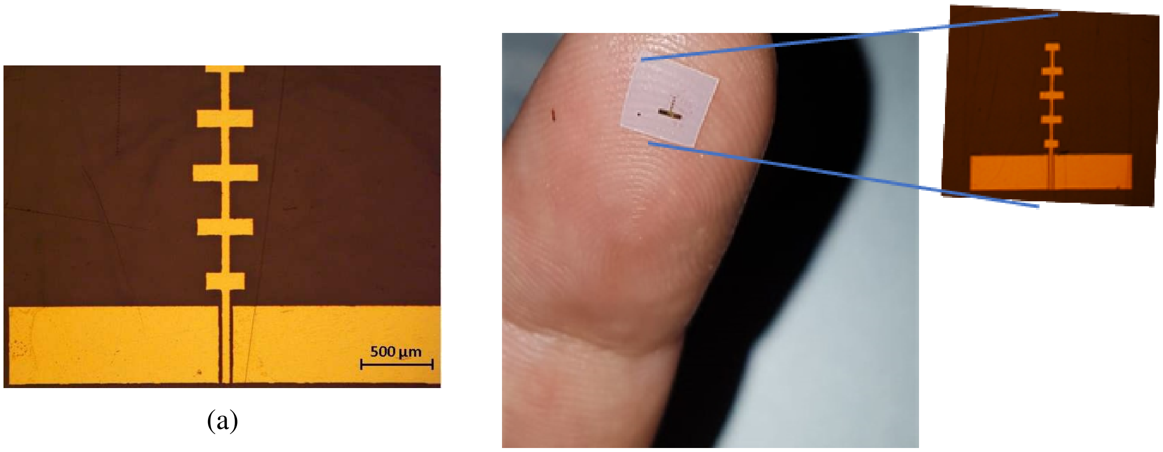

(a)

(b)

Figure 4.27: Optical image of the fabricated antenna arrays.

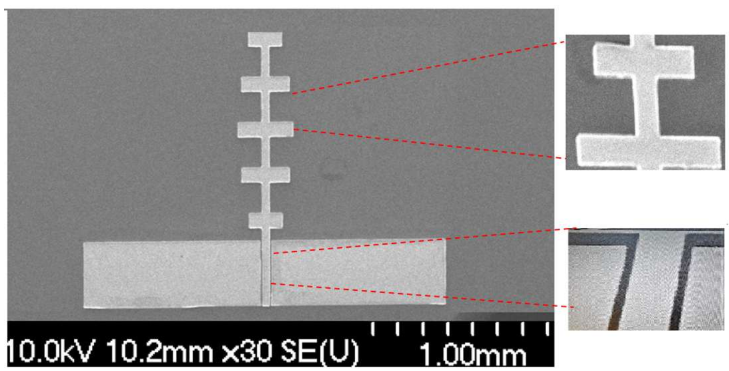

Figure 4.28: SEM image of the fabricated antenna arrays.

magnitude is much smaller at higher frequency. At 0.8 THz, the electric field over the edges of the radiating aperture is also strongly excited.

4.8 Efficiency, gain, and radiation pattern

Due to a lack of measuring capability at these very high frequencies, the antenna radiation performance was only assessed through CST modelling. The overall efficiency of the simulated antenna and the radiation efficiency of the antenna are displayed in Figure and Figures, respectively. At the lowest frequency in the band 0.9 (THz), the antenna overall effectiveness is 80%, increasing to 95 % at 1 GHz. The radiation efficiency (defined as the ratio of emitted to accepted power) is around 92 % on average over the simulated frequency spectrum.

In Figure. 4.34, the radiation patterns show high main lobe magnitudes along with lower back lobe levels. The radiation patterns are presented at E and H planes. Due to the large dielectric constant of the PEN substrate, most of the radiation is directed towards the substrate. This is a common problem with antennas fabricated on high dielectric constant substrates, which

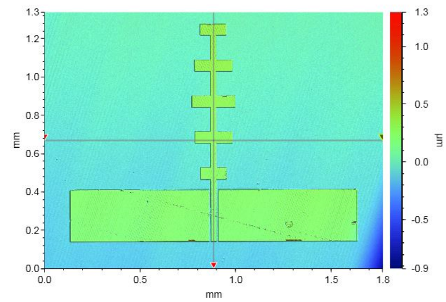

(a)

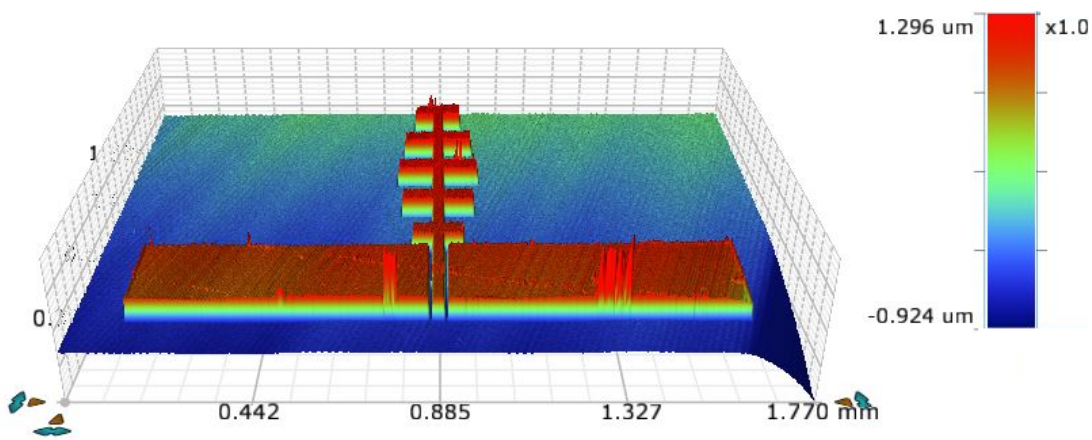

(b)

Figure 4.29: Optical counter PG image of the fabricated antenna arrays.

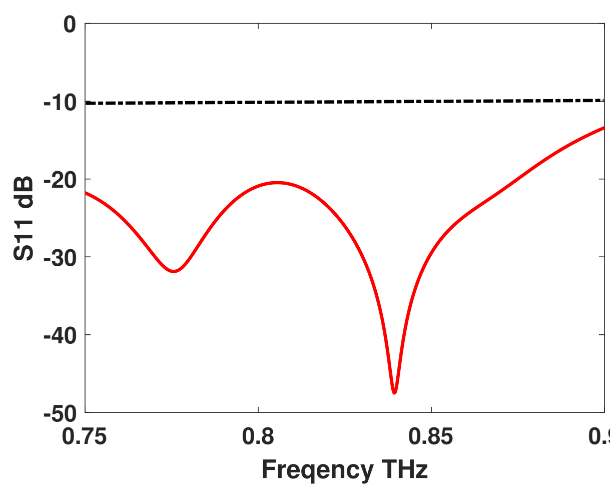

Figure 4.30: The simulated scattering response of the antenna array.

at THz frequencies is often circumvented by using a hemispherical lens. The sidelobe level is increased and the maximum side lobe is observed at 1.10THz. Therefore, the ripples in the radiation pattern may lead to a degradation in the antenna performance which is mainly caused by metal loss and skin depth effect.

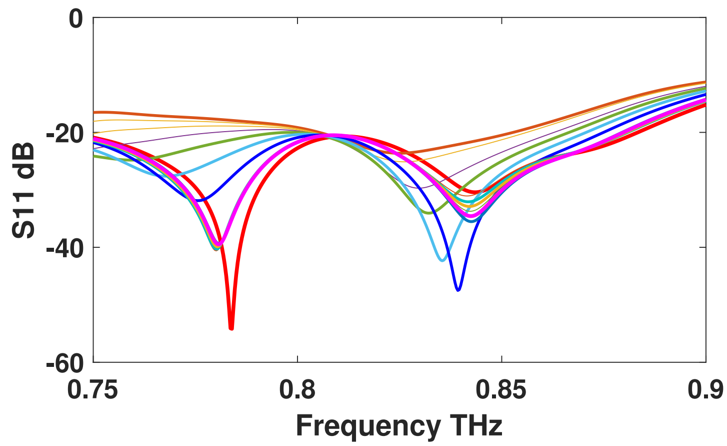

Figure 4.31: The simulated scattering response of the antenna array with different patch length.

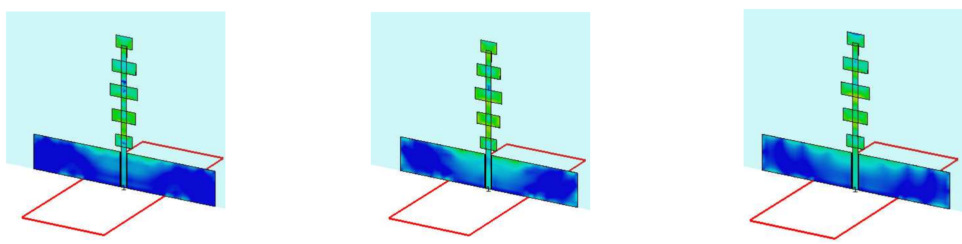

Figure 4.32: Visualisations of the surface electric current distribution at (a) 0.8 THz, (b) 0.925 THz, and (c) 1.10 THz.

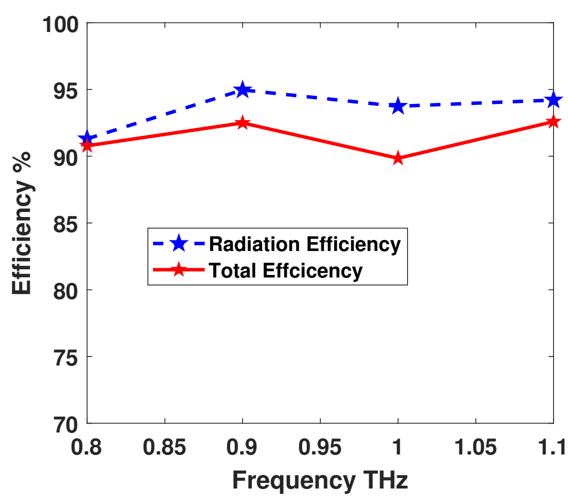

Figure 4.33: Simulated (in CST) efficiency of the proposed graphene and gold based antenna

4.9 Summary

The antenna is the most important part of any wireless communication system. Because of the considerable path loss at THz frequency and therefore improved signal-to-noise ratio, high directional antennas are a primary consideration when developing a wireless THz system. Traditional

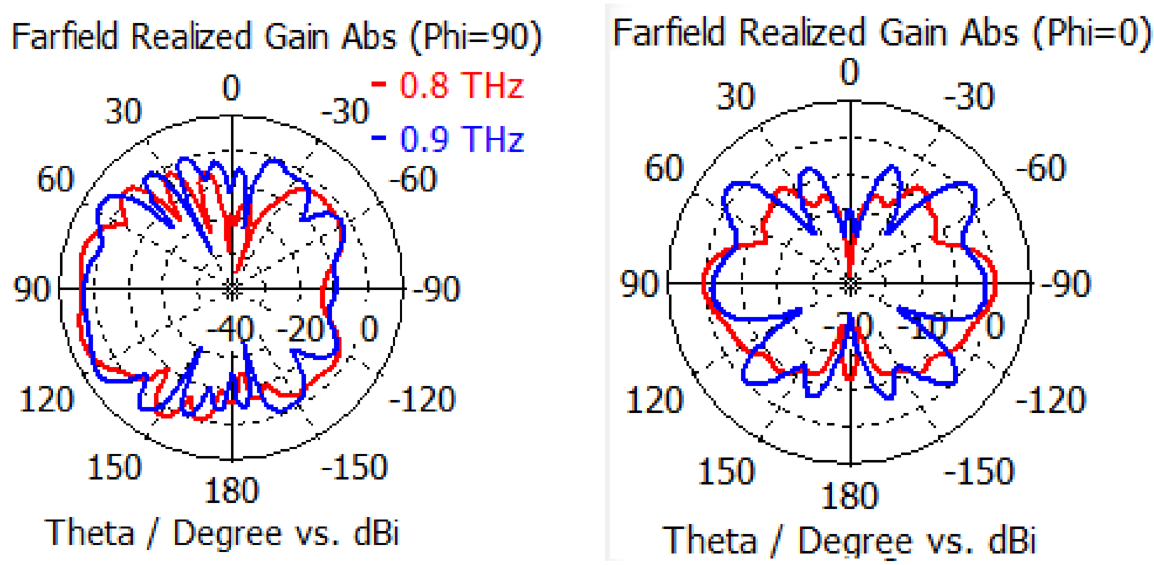

(a) (b)

Figure 4.34: Simulated radiation pattern of the proposed antenna array at two frequencies,0.8THz, 1THz and 1.1 THz

metal and carbon-based material THz antennas were described in this chapter. The well-known and widely utilised metal in the design of microwave antennas is ordinary copper. For the construction of THz antennas, carbon-based nanomaterials like as graphene have recently been studied, THz antennas made of metal and graphene were the subject of this discussion. The performance of THz antennas built of copper and graphene materials has also been compared in order to determine the optimal material for the construction of THz antenna. In terms of miniaturisation, directivity, and radiation efficiency, graphene antennas have been proven to outperform the competition. The lack of adequate THz antennas and sources kept researchers from exploring the THz spectrum for a long time. Laser and semiconductor technology advancements have led to a surge in interest in the THz frequency range, which has resulted in a rise in studies into this area.

Firstly, PICA design, a gold-based 1×4 PICA array operating in the THz frequency range of $0.75 - 1.10$THz is designed and fabricated. A simple and commonly available metal deposition technique to fabricate the structure is used. An ungrounded coplanar waveguide feeding line was used to excite the antenna. As per the authors' knowledge, the proposed design is the first instance of the THz antenna for which the scattering response was measured. Our design achieved a measured -10 dB impedance bandwidth of 400GHz at the center frequency of 0.925THz. Results also show that other antenna performance characteristics such as radiation efficiency and gain are also high.

Secondly, PICA 1×6 based on graphene and copper material was fabricated and tested. the performance of copper graphene antenna shows better result than the gold PICA antenna with high radiation efficiency 85%.

Thirdly, serial antenna arrays have been created with a focus on size and power consumption reduction as the most basic and crucial active device component in current electronics. Additionally, researchers are investigating alternative alternatives to traditional materials such as silicon, which are typically employed in the fabrication of conventional electronic devices, since fabrication limits imposed by reduced physical dimensions result in poor device packing densities. Because standard metallic antennas are mechanically rigid, their use to flexible electronic systems is restricted. As a consequence, flexible substrates have been the subject of much investigation.

The designs anticipate and techniques used in this chapter can launch a new research direction for realizing THz frequency UWB antennas for enabling high-speed wireless communications in the future.

Chapter 5

Flexible antenna for ultra-high-speed THz wireless

THz communications offer a terabit per second data rate, which enables applications not possible with mmWave technologies. THz communications, in comparison to mmWave communications, preserve better directionality, are more resistant to eavesdropping, and are less susceptible to inter-antenna interference and free-space diffraction [234]. This is mostly owing to the intrinsically shorter wavelengths associated with THz frequencies, which allows for the realisation of THz systems with much lower footprints. Additionally, unlike VLC/FSO transmissions, THz signals are less affected by elements such as cloud dust, scintillation, ambient light, and air turbulence [235].

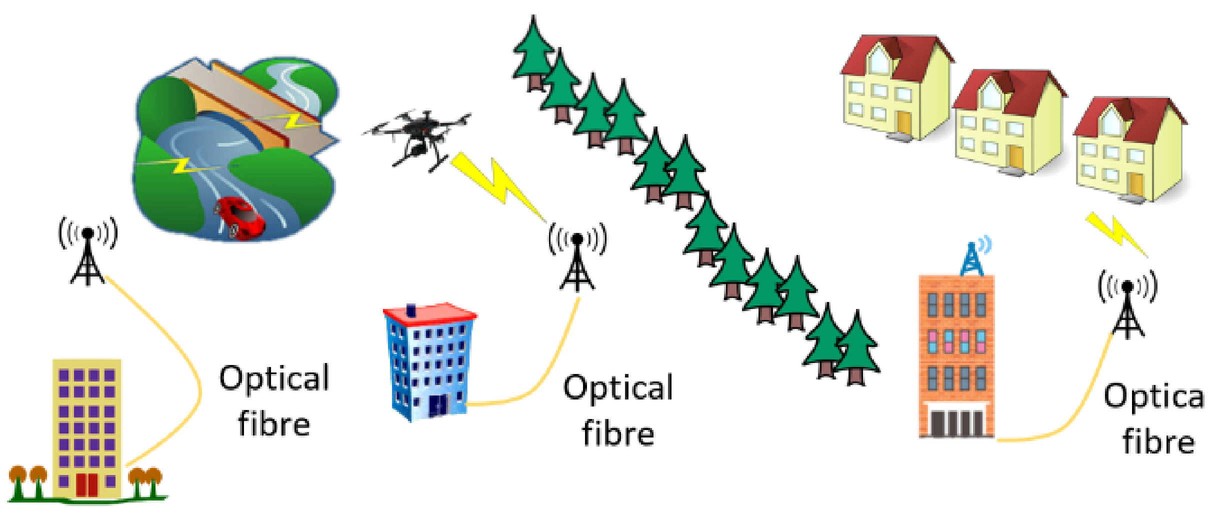

Figure 5.1: THz high Speed wireless communication applications

In a specific application, millimter and THz-band communications may significantly improve the reliability and latency of future vehicle networks [236]. Reliable and high-speed communications are important requirements for future vehicular networks, where a vehicle's ' eye view requires a latency of 50 milliseconds and a data throughput of 50 megabits per second [237]. Automatic over-take, on the other hand, needs less than 10 milliseconds of delay to achieve 99.999 percent dependability. As a result, experts believe that using the THz spectrum will enhance safety solutions and allow a variety of additional uses, including remote driving and vehicle platooning [238].

Another possible use for the THz band is high-speed communication between drones, which is another viable use case. Recently, flying ad-hoc networks (FANETs), which are made up of a number of drones, have made it possible to provide broadband communication services in rural regions and disaster-stricken areas [239]. As a result, the THz band is advantageous in such settings since it allows for large capacity while also being more flexible than FSO, which needs precise aiming and acquisition techniques. Estimating the exact position of drones is also critical for course planning and tracking, as well as for other applications. Because of the higher frequencies in the THz range, it is possible to attain superior localization accuracy in this context. [240]. For example, if a drone is communicating at 30 GHz, it will need a degree of precision in the sub-centimeter range in order to be effective. As a result, raising the frequency any higher, to the THz range, will need millimeter-level precision in localization measurements. While the THz band has a limited transmission range, it may be necessary to deploy a large number of drones in close proximity to one another, necessitating the development of multi-hop communication and localization technologies [241].

Graphene, the most recent member to the family of carbon allotropes, is often regarded as the mother of carbon allotropes. Due to its unusual features, graphene has recently garnered considerable interest in a variety of academic domains. The most notable feature is the THz propagation of SPP in graphene. SPs made of graphene feature high confinement, minimal losses, and tunability. Graphene plasmons are more amenable to manipulation by chemical or electrostatic gating in both single layer and bilayer graphene structures [242] [243] [15]. Recently, interest in realising graphene antenna designs at THz frequencies has increased. Graphene permits plasmonic antennas at THz due to SPP propagation, while metal antennas comprised of noble metals such as gold and silver exhibit plasmonic behaviour at optical frequencies. Plasmonic antennas have a large near field and a significant connection between localised sources and far-field radiation. In 2012, graphene was employed for the first time as an antenna radiator in the THz frequency band [15].

The propagation characteristics of graphene's transverse-magnetic (TM) SPP were utilised to simulate graphene patch antennas in the THz band in this study. Apart from its small size, the graphene-based THz antenna outperforms the metal antenna in terms of radiation efficiency. The graphene antenna's radiation efficiency rises as the graphene chemical potential increases. In comparison to metal antennas in the THz band, graphene plasmonic antennas provide greater miniaturisation and directivity [244].

Antennas made of graphene operate at a considerably lower frequency than conventional metallic antennas of the same size [245] [246]. Moreover, the performance of the graphene antenna at THz is enhanced by tuning the conductivity of graphene using an electric field effect [247]. Bilayer graphene enables dual-band reconfiguration while maintaining a constant impedance, obviating the requirement for a lossy and complicated reconfigurable antenna. [248].

5.1 Photolithography Fabrication Process

Photolithography use of an ultraviolet (UV) light source of wavelength between $\lambda = 200 - 400$ nm to expose the photoresist, which like that ebeam lithography in a process described in the last section. Photolithography is a low cost with a resolution capability of 0.5μm. The sample and hard mask are loaded onto the mask aligner.

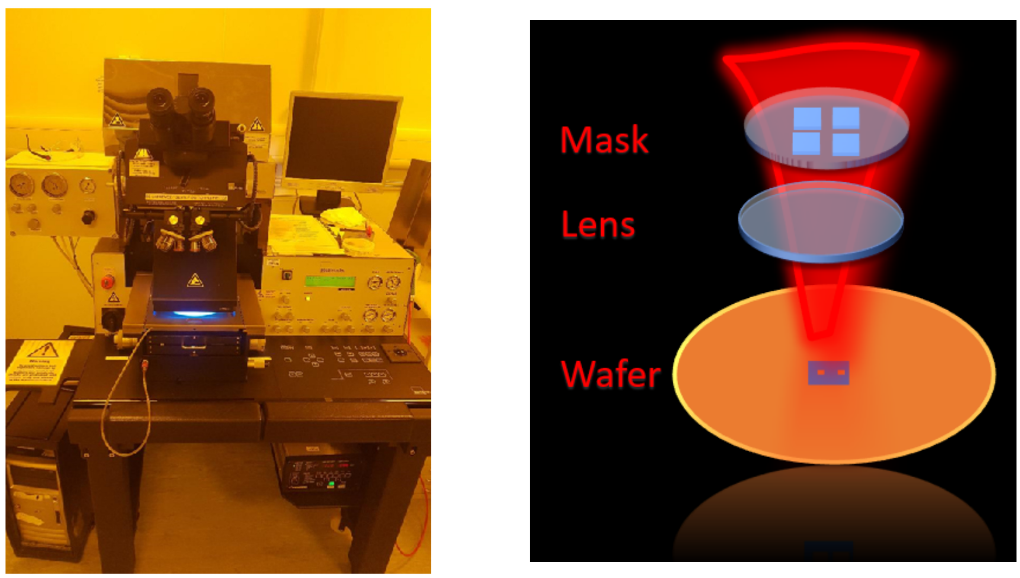

(a)

(b)

Figure 5.2: (a) Photolithography Ma6 (b) writing using photo-lithography

5.2 Mask Design

Masks for lithography were designed in L-Edit technology. When constructing a device, the critical dimension is the smallest size on a lithography level that must be precisely controlled to optimise electrical performance. It was 5μm in the designing process. The critical dimension was kept at 5μm and a set of alignment markers was developed to meet the requirements of fabrication. These are high-precision features that serve as a reference for future pattern placement and often stay constant throughout the manufacturing process.

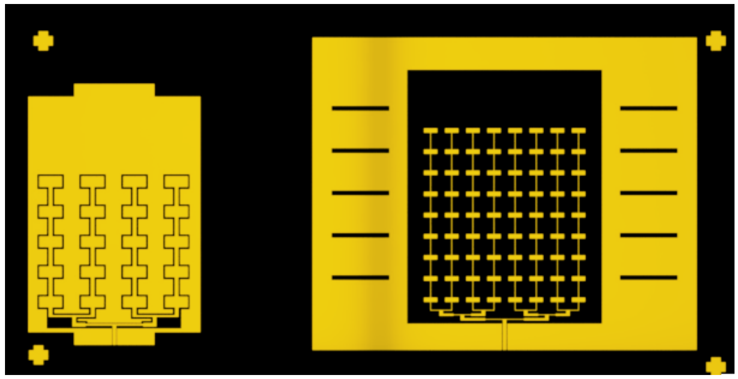

Figure 5.3: Photolithograohy Photo Mask with Cpw THz Antenna Array

5.3 Photoresist spin coating

When exposed to UV radiation, the chemical structure of the resist becomes either insoluble or soluble in the developer, depending on the kind of resist. The solvents determine the resist's viscosity, which enables it to be spun and thin layers to develop on the wafer surface. The binders regulate the resist's thermal properties. Positive and negative photoresists are available. During the developing phase of a positive resist, the exposed area dissolves while the un-exposed part stays unaltered. For the negative resist, the same rules apply.

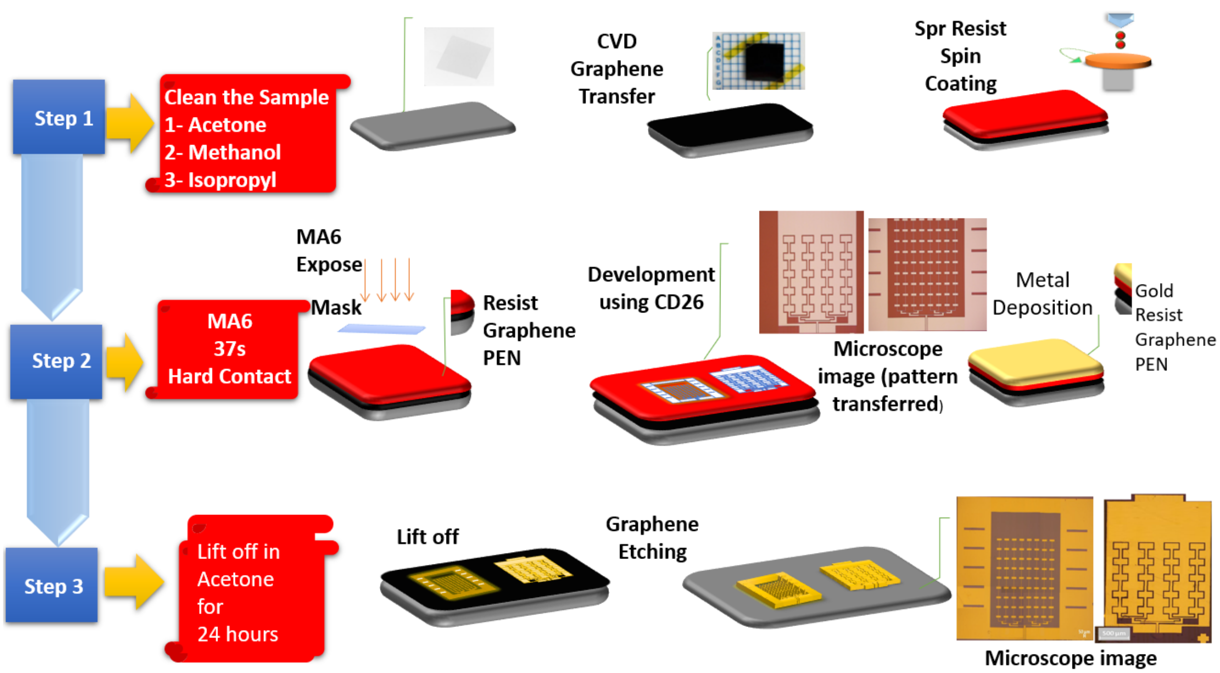

Figure 5.4: Schematic illustration of the main fabrication steps in Photolithography the process

Each kind of photoresist has a number of benefits and downsides. Although the positive photoresists exhibit high resolution and may be produced in aqueous developers, they exhibit poor adhesion and etch resistance when compared to their negative counterparts. Negative resists provide increased adhesion and resistance to etching procedures at the expense of resolution and can be created exclusively with hazardous organic developers.

Spin coating is often used to apply resist uniformly onto the substrate. The mechanics of spinning is difficult and highly dependent on the solvent's evaporation rate, which is why only a few solvent systems are utilised. The method entails spinning for a certain amount of time, often 30 seconds, at a speed determined by the required thickness..

5.4 Baking

A post-apply bake, or soft bake, is used to drive solvent from the resist. This is a critical step as failure to sufficiently remove the solvent will affect the adhesion and the resist profile, as will excessive removal, which destroys the photoactive compound and reduces sensitivity. A typical bake is 1 minute on a $90^\circ - 115^\circ C$ vacuum hot plate or 30 minutes in a $90^\circ - 115^\circ C$ convection oven. Thick resists often require longer bake times.

5.5 Developers

The developers utilised have varying concentrations, and some may need additional time for development. Developers are often advised while working with photoresists. While they are mostly interchangeable, altering the developer utilised in the process often results in a difference in the dosage necessary to obtain the same feature sizes.

5.6 Metallisation

There are many ways to deposit metal on samples, for example, physical vapour deposition (PVD), sputtering or electroplating. The technique used to deposit thin metal films in this project was electron-beam physical vapor deposition (EBPVD), a variation of PVD. Here in nanofabrication center at Glasgow university , a Plassys MEB 550S (Plassys II and Plassys IV) system are in use to deposit different types of metal such as the titanium (Ti), palladium (Pd), molybdenum (Mo), gold (Au) and nickel – chromium (NiCr). Once the sample is loaded into the evaporator, the main chamber is pumped to a base pressure of 2×10^{-6} Torr and the desired metal scheme is selected via control software.

5.7 Ti, and Al for better substrate attachment.

The design depends on an ungrounded cpw feed which does not have a ground plane at the back. Using Ungrounded CPW is one of the solutions to have better impedance matching with a sufficient substrate thickness which can save the sample from being broken during the fabrication process. Graphene layer we used as a radiation element with gold. Graphene has conductivity at terahertz band which will enhance the radiation from copper as well. On the other hand, we can not use graphene only as the the thickness of the graphene is not fit to probe measurement which has limitation of 500nm in order to be connected to any material.

Here, in the antenna arrays, the antenna element spacing was set to $\lambda/2$ at 0.8 THz. The resultant design was then optimised using the trust region framework (TSF) algorithm [207] included in the CST environment. The TSF algorithm searches locally for minimal points in a given region. However, based on the parameters provided to the framework, the algorithm can operate locally as well. To obtain the optimal antenna structure, a multidimensional problem in which all the physical dimensions of the array were parameterised was rigorously solved using high performance computing facilities at the University of Glasgow. The goal of the algorithm was to find the local minima for the initial values which were calculated using standard microstrip patch antenna designs [208]. Additionally, several researchers have developed a variety of antennas in the THz frequency region for a variety of uses. Their suggested antenna is either too big or has a restricted bandwidth. As a result, further research is necessary to enable high-speed data transfer in the THz frequency band in wireless communication. This study proposes and presents an effective rectangular microstrip patch antenna for medical imaging, homeland defence systems, explosive detection, and material characterisation, among other applications.

5.8 Anatenna Arrays Design

The first studies on the propagation of terahertz waves over graphene sheets sparked a flood of suggestions that, in essence, consist of a number of graphene layers of limited size (radiating components) installed over a dielectric material and a feed to feed the signals to the antenna. These antennas have been researched from a variety of angles, including the following: **Antenna dimensions**: the antenna arrays antenna arrays shown in Fig 5.6. The dimensions value in Fig 5.5 and table 5.1, the cpw gap is $= 7\mu$m, the substrate is PEN with permittivity εr $= 2.2$, whereas $\tau = 0.1$ps and eV $= 0$ eV. The length L is variable. Optimization of length shown in Fig.5.5 shows how longer dimensions lead to lower resonance points, as one would expect. Note, however, that metallics of the same length could theoretically resonate at much higher frequencies. The use of graphene does not change the radiation pattern at resonance as proved in other works [14].

Chemical potential: The increase of chemical potential leads to a significant shift of the resonant frequency and to an enhancement of the antenna response with changes in the radiation pattern and efficiency.

Distance b/w patch	1000um
Width feed 50	38um
Thickness of Gold	0.5um
Thickness of graphene	0.35 nm
Cpw Gap	5um
Substrate (PEN)	6 mm $\times$ 7.7 mm

Table 5.1: The Antenna Arrays Dimensions

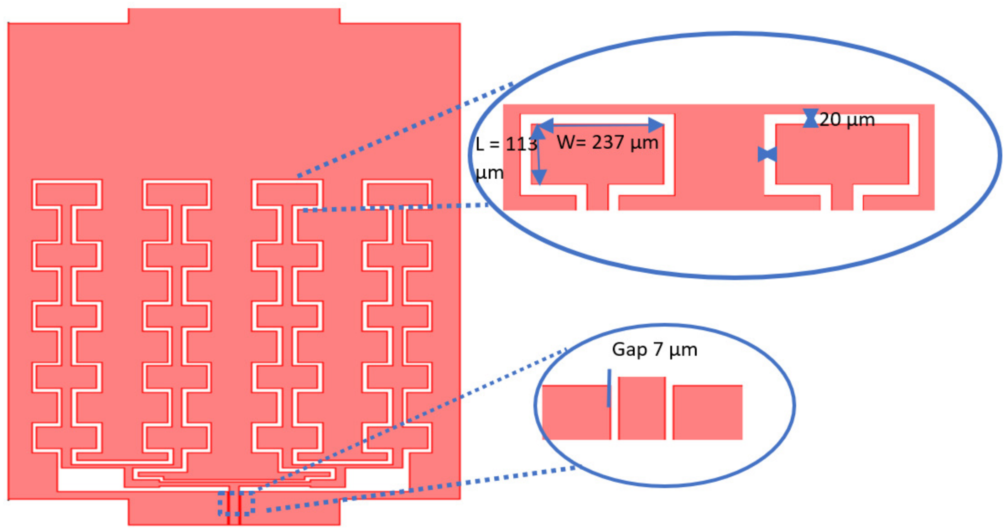

Figure 5.5: Cpw THz Antenna Arrays Dimensions

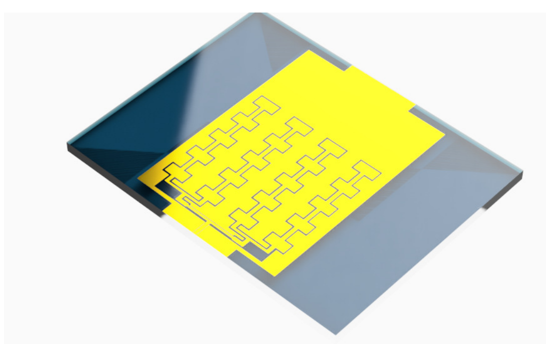

(a) Front view

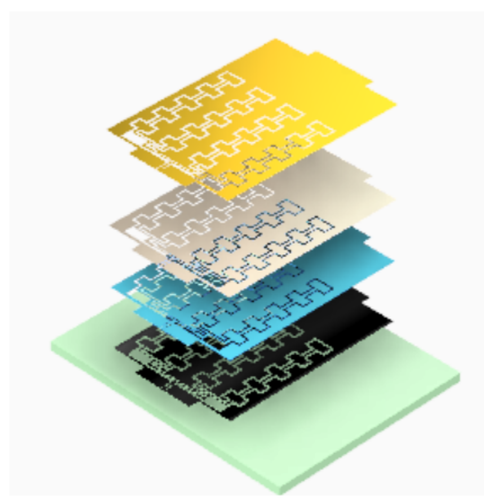

(b) Gold, Titanium, Aluminium, and Graphene

Figure 5.6: Design Antenna Arrays Structure

Relaxation time: antenna maintains the same resonant frequency as the relaxation time is increased but exhibiting a stronger resonant behaviour. PEN material exhibits better electrical performance at THz frequencies as compared to PEN material and also it is commercially available with very small substrate thickness of 125μm which is theoretically applicable for THz application.

5.9 Fabrication

Wafers were cleaned progressively in acetone, isopropyl alcohol, and dilute hydrochloric acid. fabrication process flow on PEN substrate is shown in Fig. 5.4 . After cleaning, the Graphene was transferred from copper foil onto Pen substrate using technologically incompatible, necessitating a subsequent transfer operation. Next, a primer was spin coated for 20 seconds at a speed of 4800 rpm and then baked at 115C for 35 seconds. SPr resist, a positive photoresist, was spin coated at a 4800 rpm speed and baked for 60 seconds at 900C. Lithography was carried out using a picture mask that served as the standard mask for the first alignment marks. A 34 second exposure with MA6 was used, followed by a 3 minutes development in CD26. This was followed by a 50 second hard bake at 80C on a hot plate. Following development, the patterned portion of the pen substrate was exposed for asher. Plasma ashing is a critical and commonly performed technique in manufacturing. The ashing method removes the resist by using ions and radicals created by a plasma. While ions physically dissolve the photoresist, radicals chemically react with it to form volatile molecules such as H20 and co2. Plasma ashing is a result of the interaction of these two processes. Then 10-nm aluminium film was deposited at room temperature by RF magnetron. The purpose of this coating is to encapsulate the graphene and protect it from aggressive chemicals and keep the chamical potential at 0 eV, as well as to improve adhesion to the substrate. Next, we deposited a 400-nm-thick Gold film and, a layer consisting of Titanium was deposited to improve the attachment of Gold on Al.

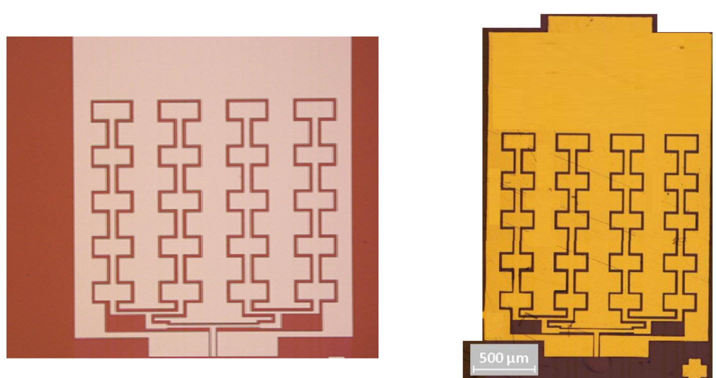

(a)

(b)

Figure 5.7: (a) Resist patterned resist on PEN substrate. (b) An optical micrscope image for the purposed Cpw THz Antenna Array

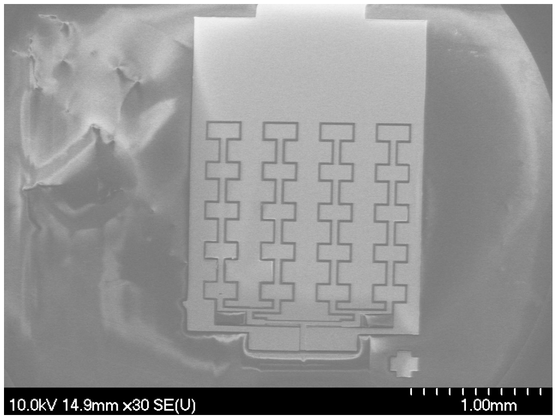

(a) Front view

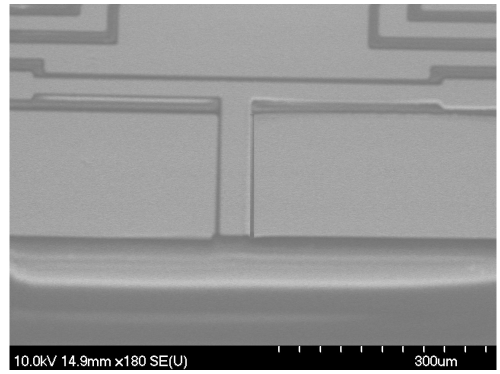

(b) Voltage divider Feed network

Figure 5.8: An SEM image for the purposed Cpw THz Antenna Array

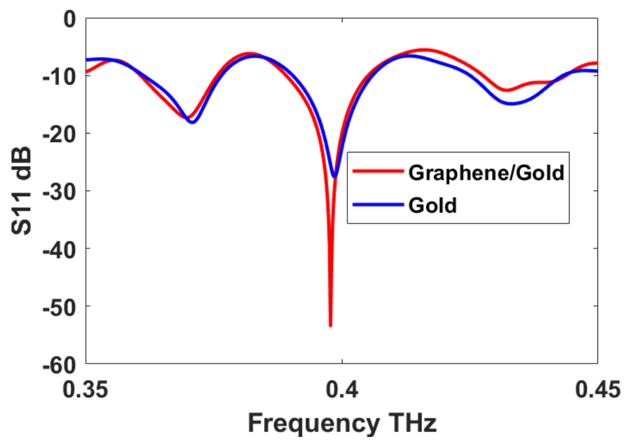

Figure 5.9: Simulated reflection coefficient of the antenna array

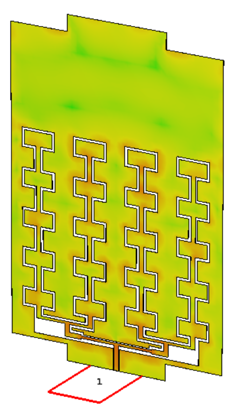

Figure 5.10: Surface current distribution of purposed Cpw THz Antenna Array

5.10 Results and Discussions

The antenna is fed by CPW, which allows for potential ease of integration into any active circuitry The antenna was simulated using CST Microwave studio's electromagnetic modelling

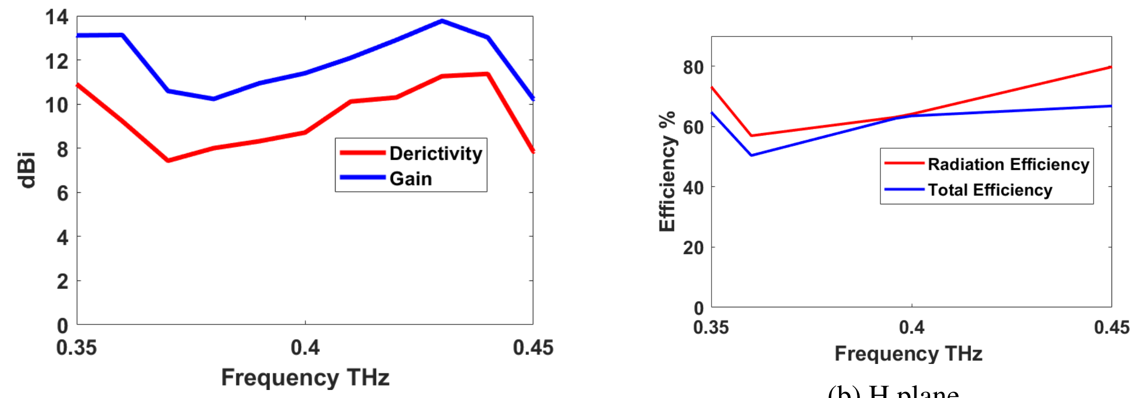

(a) E plane

(b) H plane

Figure 5.11: Simulated (in CST) Gain, Derctivity and efficiency of the proposed graphene and gold based antenna

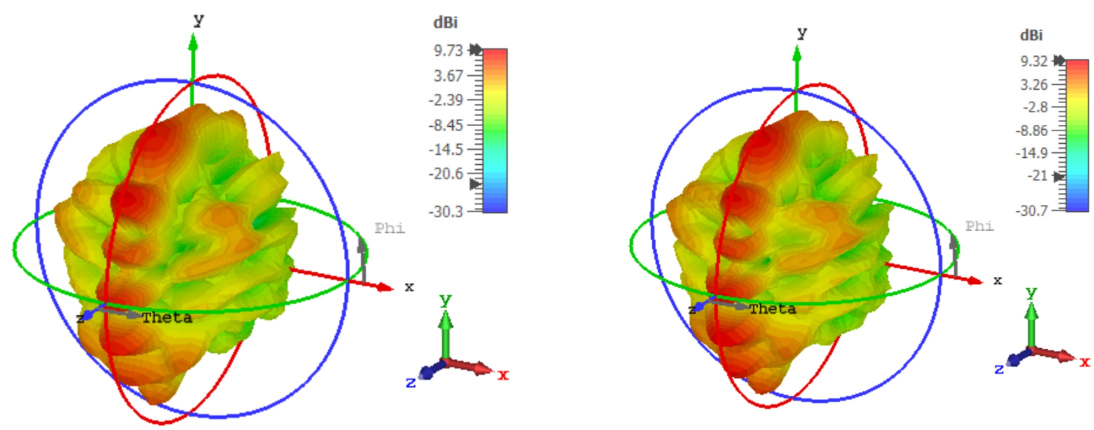

(a)

(b)

Figure 5.12: 3D radiation pattern of purposed Cpw THz Antenna Array

programme. The suggested antenna's radiation properties are constructed and examined in terms of return loss, VSWR, input impedance, directivity, and radiation pattern in the E- and H-planes. The reflection coefficient or return loss of an antenna is defined as the ratio of incident to reflected power, expressed in decibels (dB). It is indicated by s11 (dB), which should be less than or equal to -10 dB for an effective antenna. Due to the large bandwidth available in the terahertz range, it is an excellent contender for future high-speed wireless communication. Comparing the suggested antenna with the current terahertz antenna model reveals that it offers superior performance characteristics, compact size, and a wide impedance bandwidth.The antenna's impedance bandwidth is 37.50 percent, spanning the frequency range of 0.3 to 0.45 THz. The impedance match between the transmission line and the antenna is critical when assessing the performance of the antenna. The voltage standing wave ratio (VSWR) indicates how much signal is reflected back to the source as a result of an impedance mismatch between the source and the antenna. At the complete target frequency rabge, the VSWR is less than 1.5.

Figure 5.9 shows the S11 parameter comparison for the gold only and gold with graphene as

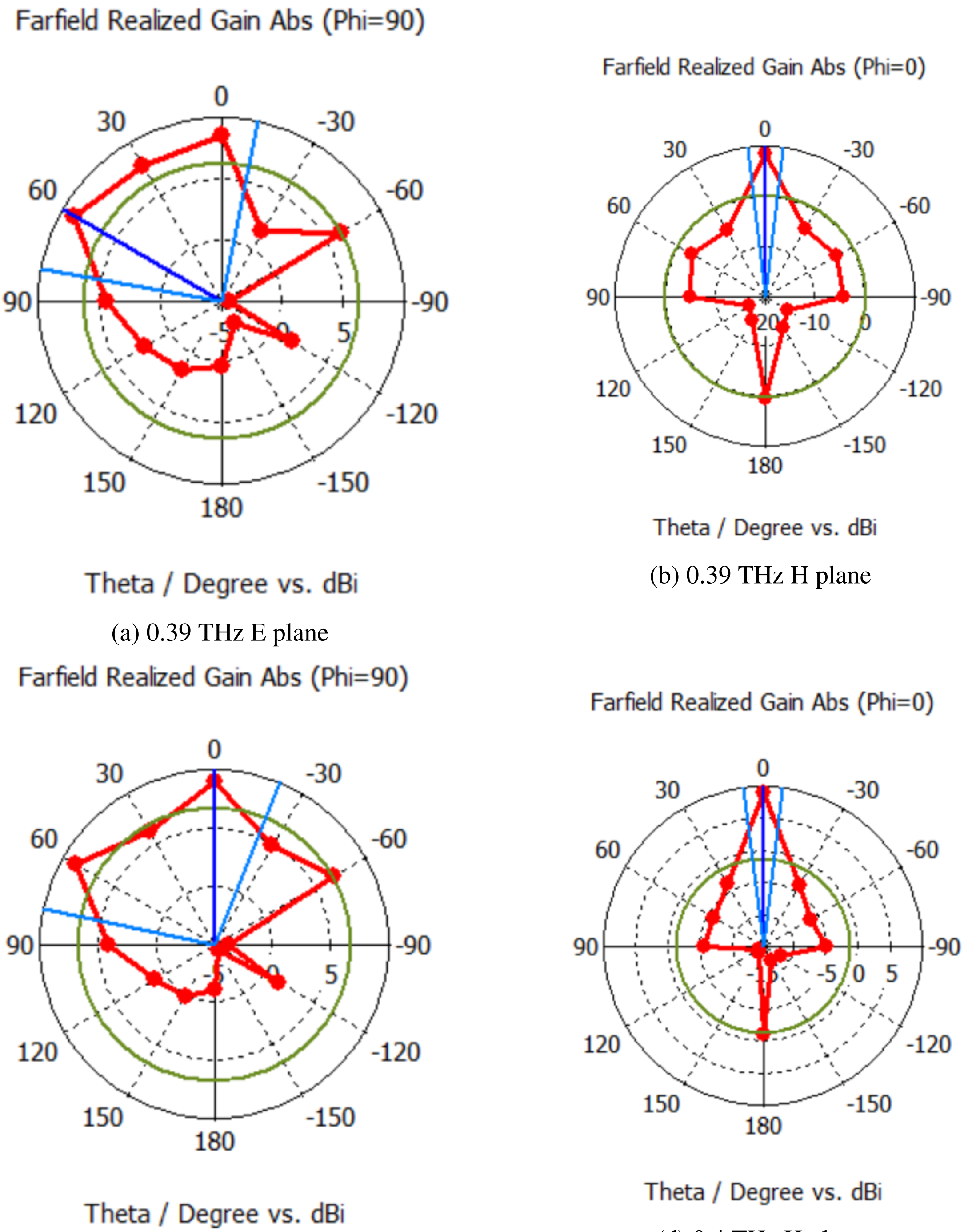

(a) 0.39 THz E plane

(b) 0.39 THz H plane

(c) 0.4 THz E plane

(d) 0.4 THz H plane

Figure 5.13: Simulated radiation pattern of the proposed antenna array

enhancement material. The simulated reflection coefficient of the the 20 elements array shows the excellent antenna performance as the whole response is below the -10dB reflection range. The reflection coefficient was reduced using Graphene material with gold compared to a standalone gold antenna array which shows that the resonant nature of the antenna is enhanced. It has been observed that resonant frequency was shifted slightly towards the lower frequency range with adding Graphene material. The S11 of the gold antenna array scenario is -23 dB at 0.4THz. The antenna has a wide bandwidth of 29.2 GHz. Whereas, the hybrid combination between gold and graphene provides an excellent antenna performance in the desired frequency range 0.4 THz with -55 dB reflection coefficient.

Figure 5.11 shows the simulated antenna performance in terms of the antenna radiation efficiency and the gain achieved by the array in the operating frequency range. It can be seen that the gain of the antenna is maintained above 8.3%. Although, this is lower as compared to antenna designs at microwave frequencies where the radiating element acts nearly as a perfect electric conductor, the conductivity of gold at THz frequencies is complex valued where the imaginary part contributes to losses. however adding graphene has improved the performance

Further investigations in which a substrate with a lower dielectric constant is used improve the radiation efficiency of the designed antenna. other substrate materials like silicon with high dielectric constant will degrade the radiation of the antenna and absorb some the radiation . Other performance parameters such as the antenna directivity and radiation efficiency are shown in Fig. 5.11, which indicates a high realised gain in the range of $0.35-0.45$ THz. the antenna has a radiation efficiency of 75%.

The co-polar and cross-polar radiation pattern in both E-plane ($\phi = 0°$) and H-plane ($\phi = 90°$) of the proposed antenna graphene array is displayed in Fig.5.13. By adjusting theta, the antenna is oriented such that the bore-sight direction is toward the vertical. (θ) from 0° to 360° for a fixed value of phi (ϕ). The main lobe magnitude is around 7dBi, main lobe direction is 0°, and angular width (3 dB)146.4° has been obtained for E-plane. For the H-plane, the main lobe magnitude, main lobe direction, sidelobe level, and angular width (3 dB) are 5.9dBi, 30°, -8.9 dB, and 79.4°, respectively, obtained at resonant frequency 0.4THz.

Terahertz research has seen a surge in interest in recent years, owing partly to the introduction of novel RF components and fast-pulse optical time domain spectroscopic methods. The two traditional development groups on each side of the terahertz spectrum – optical and microwave – are starting to merge as terahertz devices become more widely used. Both of these groups stand to profit from the design and execution of novel terahertz antennas and beam forming networks. Both frequency domain and optical time domain systems use terahertz antennas that are single mode, wide band. However, the majority of extant instruments use very simplistic architectures acquired from the microwave domain. The very specific requirements of newly proposed terahertz devices, particularly very broad band-width spectroscopy and high resolution imagers, need the development of novel antenna ideas and methods for implementing existing antenna designs. Traditional terahertz applications, such as radio astronomy, remote sensing, and radar, often demand large diameter, high surface accuracy antenna dishes that benefit from active surface correction, innovative lightweight materials, and compact designs.

5.11 THz antenna arrays with 74 elements.

Broadcasting dynamic beamsteering at very high speeds would need an ideal relay method that takes into account the behaviour of THz band channels in very large arrays in addition to synchronisation requirements. The available bandwidths are substantially larger, and since the transmission speed is related to the available bandwidth, THz becomes excellent for ultra-high speeds. The architecture will be incorporated into wireless communication equipment in the future, enabling the next generation of "6G" communications to operate at extraordinary terabytes-per-second speeds (10 to 100 times faster than 5G). The proposed CPW fed transmit array antenna is shown in Fig 5.15, which comprises a thin gold on a single graphene layer on a transparent and flexible Polyethylene Terephthalate (PEN). A single layer metallization is used to keep the radiation pattern intact with high gain characteristic, which may degrade. The design procedure involves the realization of a single CPW microstrip patch antenna and then replicates of a single antenna at a centre-to-centre distance of $\lambda/2$ to form a 72 elements array, fed by a corporate feed network.

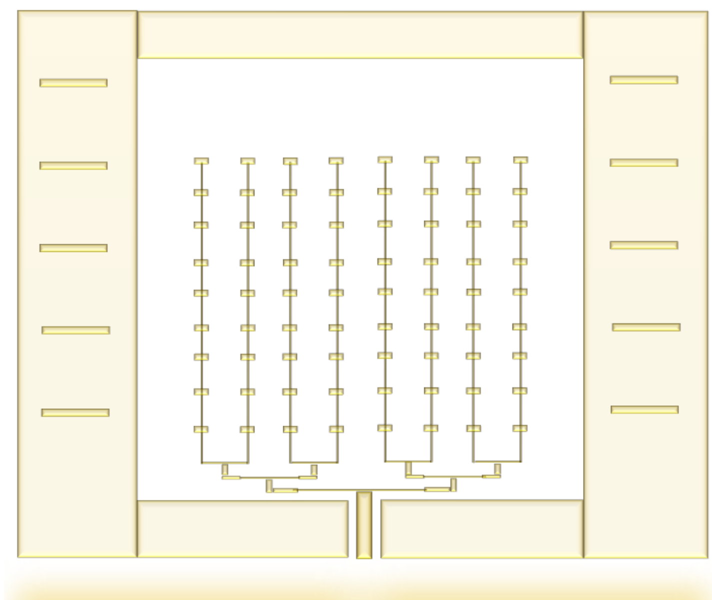

Figure 5.14: Cpw THz Antenna Array Dimensions.pdf

Fig.5.15 shows the four layers patch antennas structure, gold, Ti, Al and graphene fed by a 50Ω feed line, whose length and width are optimized to achieve the maximum impedance match between the feed and the radiating patch. The length and width are calculated by experimentally verified formulas. The proposed CPW microstrip transmit array antenna is simulated in a full-wave 3D CST Method based electromagnetic simulator.

Following development, the patterned portion of the pen substrate was exposed for asher. Plasma ashing is a critical and commonly performed technique in manufacturing. The ashing method removes the resist by using ions and radicals created by a plasma. While ions physically

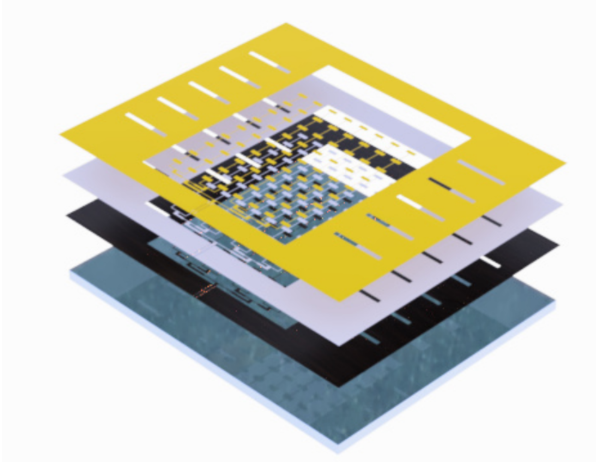

(a) Gold,Graphene, and Titanium

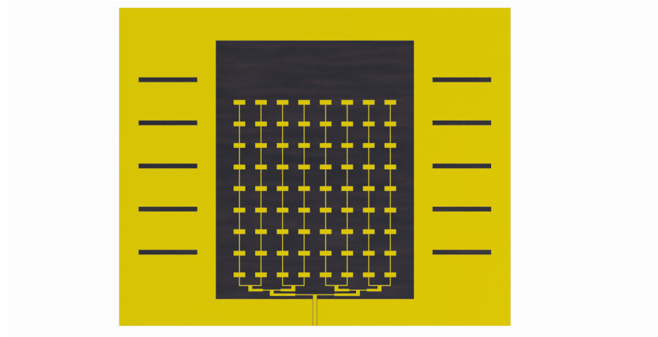

(b) Front View

Figure 5.15: Antenna Arrays Structure

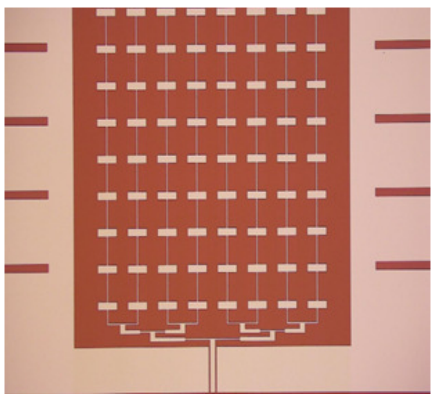

(a)

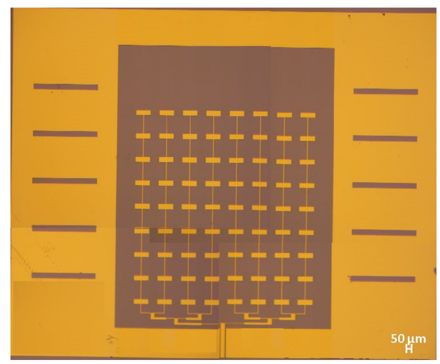

(b)

Figure 5.16: (a) Developed Resist of THz Antenna Array . (b) An optical micrscope image for the purposed Cpw THz Antenna Array

dissolve the photoresist, radicals chemically react with it to form volatile molecules such as H20 and co2. Plasma ashing is a result of the interaction of these two processes.

5.12 Fabrication

One of the most challenging issues with flexible substrates, regardless of the materials employed, is the substrate's dimensional fluctuation during device fabrication. Flexible substrates intended to be used in place of solid glass substrates must fulfil a number of requirements:

Surface roughness: as the device films get thinner, their electrical functionalities become increasingly sensitive to surface roughness. Short-distance asperity and roughness must be avoided, although roughness over extended distances is acceptable. Thermal and thermomechanical properties: the substrate's operating temperature, for example, the polymer's glass transition temperature, must be compatible with the manufacturing process's maximum tem-

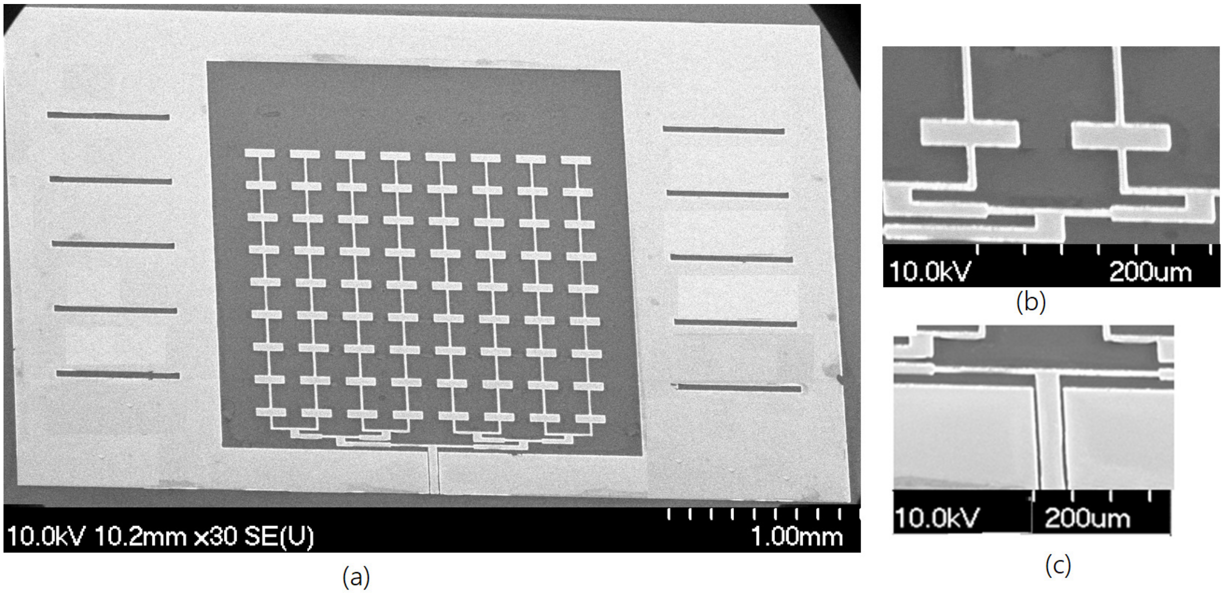

Figure 5.17: SEM image of a plasmonic terahertz antenna arrays prototype based on nanoscale Au contact 0.35 nm graphene material

perature. Thermal mismatches between device films and substrates may result in film failure during the fabrication's thermal cycling. On Flexible substrates, dimension stability during processing is a challenge. Chemical characteristics. The substrate should be contaminant-free and inert to process chemicals. Advantageous are substrates that act as effective barriers to ambient gas penetration. A substrate with a high elastic modulus provides stiffness, while a hard surface protects the device layer from impact. Conductive substrates may serve as both a common node and a barrier against electromagnetic interference. Coupling capacitances are minimised on electrically insulating substrates. Magnetic substrates may be used to temporarily mount the substrate during fabrication or to permanently attach the completed product. Wafers were cleaned progressively in acetone, isopropyl alcohol, and diluted hydrochloric acid. A primer was spin coated for 20 seconds at a speed of 4800 rpm and then baked at 115C for 35 seconds. SPr resist, a positive photoresist, was spin coated at a 4800 -rpm speed and baked for 60 seconds at 900C. Lithography was carried out using a picture mask that served as the standard mask for the first alignment marks. A 34 second exposure with MA 6 was used, followed by a 3 -minute development in CD26. This was followed by a 50-second hard bake at 80C on a hot plate.

5.13 Results and discussions

Figure 5.18a shows the reflection coefficient results of the parameter sweeps. The reflection coefficient S11 was 34 dB at the resonant frequency 0.85 THz. The antenna arrays achieved good reflection coefficient from 0.83 to 0.86 THz with wide bandwidth of around 20 GHz The simulated surface current distribution of the antenna for different frequencies within the UWB is indicated in Fig 5.18b.The current vectors indicate the formation of a closed loop between the patch and the ground plane and hence an efficient antenna radiation.

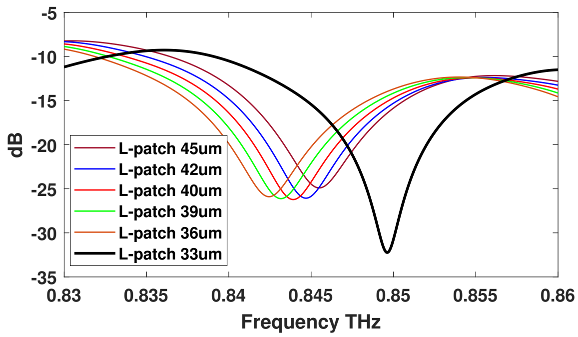

(a)

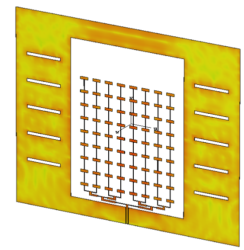

(b)

Figure 5.18: (a) Simulated reflection coefficient of the antenna array. (b) Surface Radiation pattern.

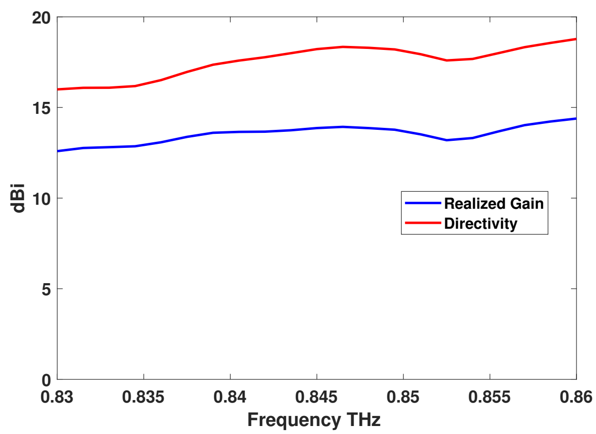

Figure 5.19: Realized gain and dierctivity of proposed antenna arrays on free space

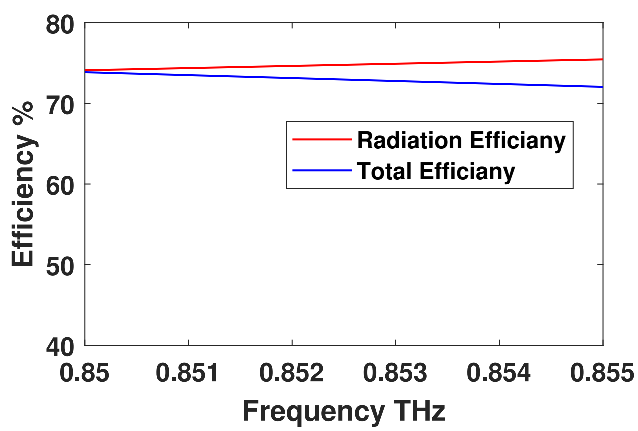

Figure 5.20: Total and Radiation efficiency of proposed antenna arrays on free space

5.13.1 Efficiency, gain, and radiation pattern

Although the Total efficiency at the lower end of the desired band range decreases at a frequency of 0.855 THz, it is still achieving a high radiation efficiency above 76% for the hybrid graphene and gold materials combination (Fig 5.20). As the conductivity of graphene increases with frequency, consequently, the radiation efficiency is improved and supporting conductivity of gold which declines with frequency due to high surface impedance which leads to degreed of radiation efficiency. The radiation efficiency of the hybrid material structure (gold and graphene) maintained an excellent radiation efficiency of 78% and around 80% at the end of desired band. The antenna array gain gradually increases with frequency Fig 5.19. A gain of 13.5 dBi at 0.85 THz. Whereas for the hybrid antenna array the directivity achieved was 17.13 dBi at 0.85 THz.

The 2-D radiation pattern is also a parameter of output performance that modulates the radiation properties. By studying the radiation pattern at resonant frequencies, the angle of radiation can be determined. The two-dimensional radiation pattern reflects a range of resonance frequencies, i.e. 0.85, 0.855, 0.84 and 1.56 THz are simulated as presented in Fig 5.22. The whole overall pattern in Fig 5.12 represents the total gain of the proposed antenna at various resonance frequencies. Elevation pattern $E(\theta)$ and azimuthal pattern $E(\varphi)$ of Fig 5.22. represents the gain radiated in elevation plane ($Y-Z$ planes) and azimuthal plane ($X-Y$ plane). The examination of radiation characteristics reveals that the proposed antenna radiates more in the phi ($X-Y$ planes) direction and less in the theta ($Y-Z$ plane) direction. Radiation characteristics are normally calculated in the far field area as a function of co-ordinates, but they may also be classified in terms of power pattern or field pattern.

Furthermore, it is obvious from the total patterns of all resonant frequencies that the major lobe is stronger than the back lobe and it is analysed that this proposed THz antenna is radiating at an angle of 80° in the Phi direction and 90° in the Theta direction (3D figure). This antenna exhibits a miniaturized structure as size of the antenna is proportional to the wavelength, hence, it is confirmed that the proposed antenna will consume very less power while functioning as transmitter or receiver. If wireless devices like sensors are developed to function in the terahertz frequency region, then issues of high data rate and less power consumption can easily be resolved.

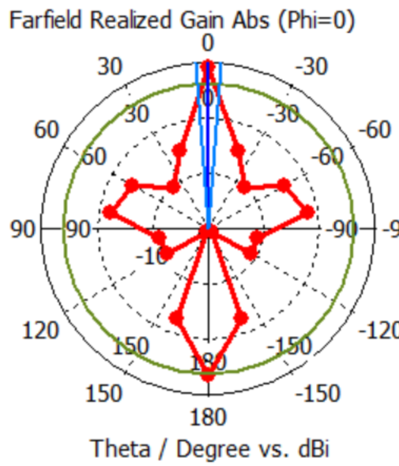

(a) E plane 0.85 THz

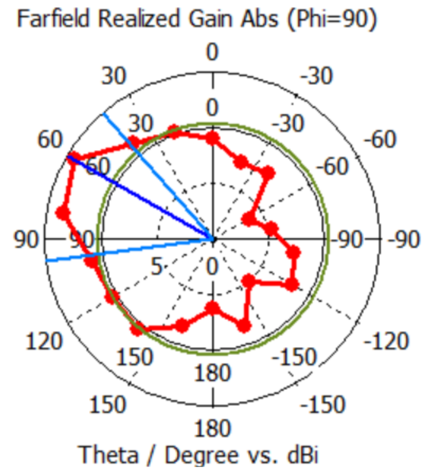

(b) H plane 0.85 THz

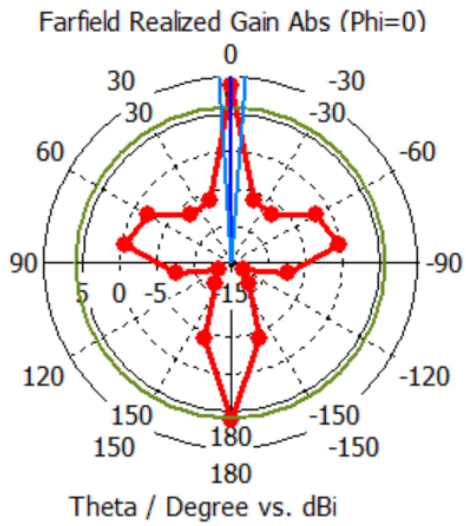

(c) 0.855 THz E plane

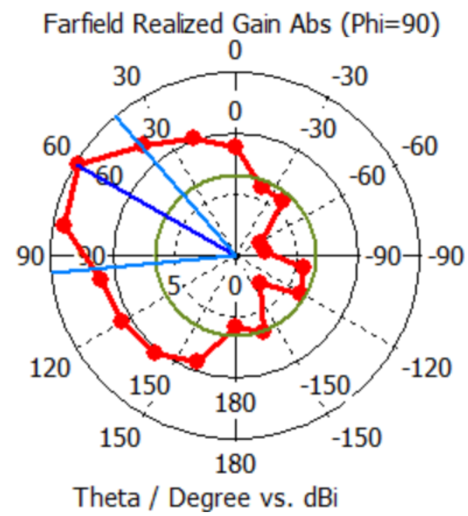

(d) 0.855 THz H plane

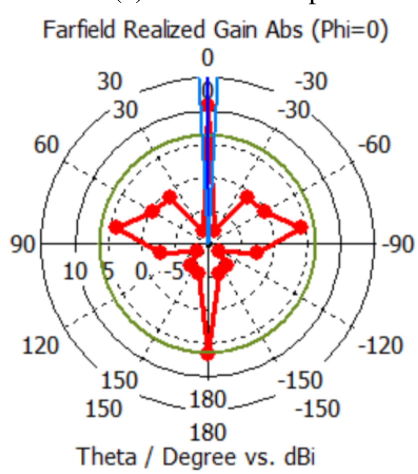

(e) 0.86 THz E plane

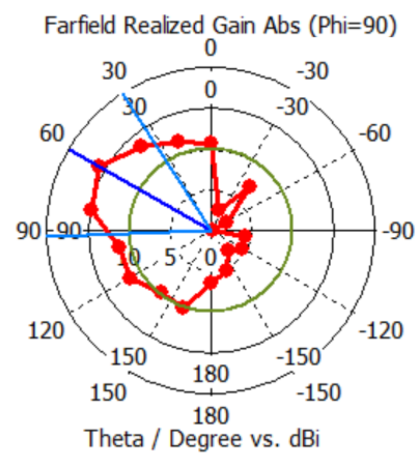

(f) 0.86 THz H plane

Figure 5.21: Simulated radiation pattern of the proposed antenna array

5.14 Summery

The terahertz spectrum has the potential to significantly increase the present data speeds in wireless networks. We can reduce the frequency by two orders of magnitude and the power

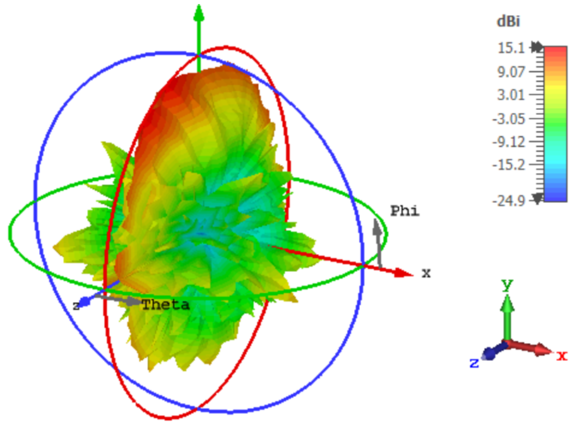

(a) 0.85 THz

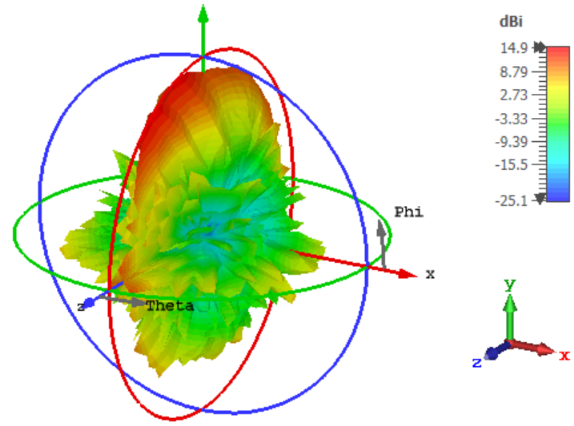

(b) 0.855 THz

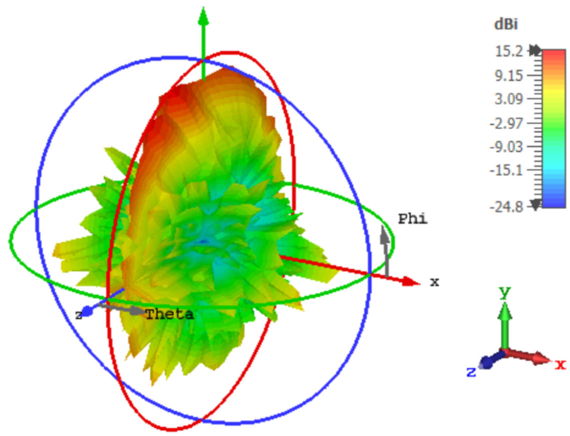

(c) 0.86 THz

Figure 5.22: 3D radiation pattern of purposed Cpw THz Antenna Array

needed by four orders of magnitude with this antenna. Current cellular systems provide data transfer speeds of up to one gigabit per second in LTE advanced networks and up to ten gigabits per second in so-called millimetre wave or 60 gigahertz systems. We anticipate data speeds in the terahertz region on the order of terabits per second.

The communication problem is that metallic antennas at the nano size would have to function at hundreds of terahertz. While certain frequencies may provide benefits in terms of communication speed, their range would be restricted to a few micrometres due to propagation losses. Additionally, they would need a great deal of power more than nanomachines are expected to have. Gold, silver, and other noble metals can also enable SPP wave propagation, but only at considerably higher frequencies than graphene. Waves are not supported by conventional materials such as copper.

When activated by an incoming electromagnetic wave, for example, electrons in graphene begin to oscillate. Due to the graphene's unique features, this global oscillation of electrical charge produces a restricted electromagnetic wave on top of the graphene sheet. The action, which is officially referred to as a surface plasmon polariton (SPP) wave, enables the nano-antennas to function in the low end of the terahertz frequency range, between 0.1 and 10 terahertz. SPP waves may be generated for transmission by injecting electrons into the dielectric layer underlying the graphene sheet.

The work presented in this chapter demonstrates that the notion of graphene-based nano-antennas is possible, even more so when very precise models of electron transport in graphene are used. While other hurdles remain, this is an important first step toward developing sophisticated nanomachines with numerous uses in medicinal, environmental, industrial, and military domains.

Chapter 6

Conclusion and Future Work

For a long time, researchers ignored the THz band due to a lack of adequate THz antennas and sources. Due to developments in laser and semiconductor technology, the availability of THz sources in the THz band has raised research interest in the THz frequency range. A Terahertz (THz) antenna with a size of a few micrometres cannot be accomplished by just reducing the extent of a traditional metallic antenna down to a couple of micrometres. This approach has several downsides. For example, the low mobility of electrons in nanoscale metallic structures would result in high channel attenuation. Thus, using traditional micrometre metallic antennas for THz wireless communication becomes unfeasible. As opposed to their visible-spectrum features, metals such as gold and silver, which typically exhibit SPPs, have completely different THz physical properties. 2DMs, for example, graphene, perovskite, and MoS2 (TMDs), provide a ground-breaking stage to control the propagation, modulation, and detection of THz waves. This thesis proves that 2DMs can enable the propagation of SPP waves in the THz band. These materials offer a promise of a future technological revolution. Combined with other profound advantages in lightweight, mechanical flexibility, and environmental friendliness, 2DMs can be used to fabricate low-cost wearable devices.

This thesis explored several THz sources and manufacturing procedures for THz antennas in order to facilitate the actual implementation of THz wireless communication systems. A wearable graphene THz antenna is presented and tested on three layers of human skin to serve the wearable applications in modern THz systems to achieve high performance.

Wearable THz antennas based on graphene have been developed and tested on three layers of human skin to meet the demands of contemporary THz systems. Because of the absorption of radiated energy, the antenna performance of wearable antennas will be reduced. We expect the antenna to work best at a distance of 1 or 2 millimetres from the surface of the human body. Due to human body proximity, antenna performance was impacted in terms of frequency detuning and radiation pattern distortion. The suggested design offers a number of advantages, including high radiation efficiency and simple manufacture. PEN film, which is widely accessible and inexpensive, was used as a flexible substrate in this study. Personal security, health and well-being monitoring, big data, and the Internet of Things (IoT) might benefit from this wearable antenna design. For short-range THz communication, graphene's exceptional electromagnetic, mechanical, electrical, and thermal capabilities have made it possible. The atomically thin profiles and exceptional electrical capabilities of graphene-based devices allow for flexible, stretchy, or even conformal features in any application. Short-range wireless body area networks (WBANs) may be a good fit for the antenna in the future. This study also reported $CH_3NH_3PbI_3$ perovskite as a promising material for THz antennas for wearable applications. $CH_3NH_3PbI_3$ has a high charge carrier mobility and diffusion length, indicating that this material is a potential candidate for antenna design. A novel hybrid THz antenna array design made from gold and perovskite layers is demonstrated. The antenna array was simulated using a multi-layered structure of perovskite, gold, and PEN substrate. Results show that in the frequency range of 0.9 - 1.2 THz, the antenna performance significantly improves over a gold-only antenna. The proposed work also shows that with the fast emergence of 2DMs having electrical conductivity. The electrical properties can be controlled to a better performance by selecting the preparation method by chemical doping or external basing. The perovskite and hybrid antenna array display better performance at room temperature which is superior. The result opens a way for more profound understanding and further improvement of perovskite material in various applications. The capacity to be a decent radiating element at room temperature is a remarkable feature which puts these materials in an exclusive class of supporting conventional metal at THz frequency band. The result shows that the $CH_3NH_3PbI_3$ is incredibly promising for advanced THz applications, particularly THz wireless communication. Future work would be concentrated on optimisation of the intrinsic property and fabrication methods of thin films for adoption in THz antenna. In this study, we have designed, fabricated, and measured five different designs using different materials in the THz band, which will pave the way for enabling future THz short-range wireless communication.

6.1 Future work

- Various types of 2DMs available , and some of them can provide high conductivity, which is required in THz wireless communications. Reviewing recent work. on 2DMs reveals that improved methods in terms of fabrication and measurement are required. 2DMs have a lot of advantages, including lightweight, flexibility, electrical characteristics, and environmental friendliness. 2DM can be ideal with THz wearable devices. On the contrary, a fundamental disadvantage of 2DMs is their high absorption. Finally, it is concluded that the current technology needs to be further developed in the years to come and many problems related to the THz communication system need to be solved.

- However, there are numerous other 2DMs that remain undiscovered. Furthermore, combining different 2DMs results in new structures with unique physical and concoction properties [45].

- The attractive feature about perovskite, graphene and other 2DMs is the ultra-high specific surface areas that enable their energy band structures to be sensitive to external basing. In the literature, scientists have tested a wide range of nano-antenna designs using modelling and simulation approaches. Nano-antenna fabrication and measurement using 2DMs is still the missing piece in the THz band. The design, fabrication, and measurement of THz antennas based on 2DMs for wearable wireless communication is the primary goal for future study work.

- Due to the limited RF output power supplied by presently available THz signal sources and the absence of a clear winner technology at these frequencies, free-space propagation losses and atmospheric absorption are of key concern. It is a daunting system design task to minimise generating losses while delivering sufficient power to the receiving end. To overcome the difficulty of increasing the radiated power at high frequencies, beamforming is an intriguing technique to examine.

- Increasing the directivity while maintaining the same height is possible with a flat antenna. There are a few antennas in the literature that operate at this frequency and have a comparable number of components. Planar, horn, reflectarray, and lens-type metal antennas have been developed for THz applications [249] [250] [251] [252] [253].

- The antenna array presented here was created to operate in the THz frequency range (0.75 – 1.1 THz). In the future, experimental measurements of radiation patterns will be made to confirm the simulations. Future study is also needed to scale the design to higher frequencies and characterise the performance for varied substrate thicknesses to examine the influence of thickness. Low-loss substrate material is critical for the development of THz components and systems, since the signal at these frequencies may be significantly attenuated by oxygen, water, and other gases in the environment. As a result, a suitable substrate material with low loss and dispersion in THz bands is required.

- As a result of further advancements in fabrication technologies, various new technologies are now available to match the THz processing requirements. 3D printing, also known as additive manufacturing [254] [255] [256], is a process for fabricating three-dimensional items by printing them layer by layer, typically from a three-dimensional digital model. 3D printing is well suited for massive structural components with complex forms. Precision of up to 0.01 mm may be achieved with 3D printing technologies. However, following printing, powder metallurgy pieces must be sintered. The sintering process results in deformation due to the high temperature and shrinkage rate. The machining process is required for the creation of high-precision components.

- Despite the substantial progress in THz devices work recently THz applications are still in the initial stages of development. As a result, numerous additional potential applications can be added to healthcare, short-range wireless communications, safety, food quality detection, spectroscopic analysis.

Bibliography

[1] D. Liu, U. Pfeiffer, J. Grzyb, and B. Gaucher, *Advanced millimeter-wave technologies: antennas, packaging and circuits*. John Wiley & Sons, 2009.

[2] D. Grischkowsky, S. Keiding, M. Van Exter, and C. Fattinger, "Far-infrared time-domain spectroscopy with terahertz beams of dielectrics and semiconductors," *JOSA B*, vol. 7, no. 10, pp. 2006–2015, 1990.

[3] B. Ferguson and X.-C. Zhang, "Materials for terahertz science and technology," *Nature materials*, vol. 1, no. 1, pp. 26–33, 2002.

[4] A. Davies, E. H. Linfield, and M. B. Johnston, "The development of terahertz sources and their applications," *Physics in Medicine & Biology*, vol. 47, no. 21, p. 3679, 2002.

[5] M. Tonouchi, "Cutting-edge terahertz technology," *Nature photonics*, vol. 1, no. 2, pp. 97–105, 2007.

[6] I. Hosako, N. Sekine, M. Patrashin, S. Saito, K. Fukunaga, Y. Kasai, P. Baron, T. Seta, J. Mendrok, S. Ochiai *et al.*, "At the dawn of a new era in terahertz technology," *Proceedings of the IEEE*, vol. 95, no. 8, pp. 1611–1623, 2007.

[7] J. Shi, Z. Li, D. K. Sang, Y. Xiang, J. Li, S. Zhang, and H. Zhang, "Thz photonics in two dimensional materials and metamaterials: properties, devices and prospects," *Journal of Materials Chemistry C*, vol. 6, no. 6, pp. 1291–1306, 2018.

[8] H.-J. Song and T. Nagatsuma, "Present and future of terahertz communications," *IEEE transactions on terahertz science and technology*, vol. 1, no. 1, pp. 256–263, 2011.

[9] T. Kleine-Ostmann and T. Nagatsuma, "A review on terahertz communications research," *Journal of Infrared, Millimeter, and Terahertz Waves*, vol. 32, no. 2, pp. 143–171, 2011.

[10] J. Pourahmadazar and T. A. Denidni, "Millimeter-wave planar antenna on flexible polyethylene terephthalate substrate with water base silver nanoparticles conductive ink," *Microwave and Optical Technology Letters*, vol. 60, no. 4, pp. 887–891, 2018.

[11] H.-T. Chen, W. J. Padilla, J. M. Zide, A. C. Gossard, A. J. Taylor, and R. D. Averitt, "Active terahertz metamaterial devices," *Nature*, vol. 444, no. 7119, p. 597, 2006.

[12] J. Campos-Delgado, J. M. Romo-Herrera, X. Jia, D. A. Cullen, H. Muramatsu, Y. A. Kim, T. Hayashi, Z. Ren, D. J. Smith, Y. Okuno *et al.*, "Bulk production of a new form of sp2 carbon: crystalline graphene nanoribbons," *Nano letters*, vol. 8, no. 9, pp. 2773–2778, 2008.

[13] L. Ju, B. Geng, J. Horng, C. Girit, M. Martin, Z. Hao, H. A. Bechtel, X. Liang, A. Zettl, Y. R. Shen *et al.*, "Graphene plasmonics for tunable terahertz metamaterials," *Nature nanotechnology*, vol. 6, no. 10, p. 630, 2011.

[14] S. Abadal, I. Llatser, A. Mestres, H. Lee, E. Alarcon, and A. Cabellos-Aparicio, "Time-domain analysis of graphene-based miniaturized antennas for ultra-short-range impulse radio communications," *IEEE Transactions on communications*, vol. 63, no. 4, pp. 1470–1482, 2015.

[15] M. Tamagnone, J. Gomez-Diaz, J. Mosig, and J. Perruisseau-Carrier, "Analysis and design of terahertz antennas based on plasmonic resonant graphene sheets," *Journal of Applied Physics*, vol. 112, no. 11, p. 114915, 2012.

[16] J. P. Guillet, B. Recur, L. Frederique, B. Bousquet, L. Canioni, I. Manek-Hønninger, P. Desbarats, and P. Mounaix, "Review of terahertz tomography techniques," *Journal of Infrared, Millimeter, and Terahertz Waves*, vol. 35, no. 4, pp. 382–411, 2014.

[17] N.-G. Park, T. Miyasaka, and M. Gr tzel, "Organic-inorganic halide perovskite photovoltaics," *Cham, Switzerland: Springer*, 2016.

[18] A. Chanana, Y. Zhai, S. Baniya, C. Zhang, Z. V. Vardeny, and A. Nahata, "Colour selective control of terahertz radiation using two-dimensional hybrid organic inorganic lead-trihalide perovskites," *Nature communications*, vol. 8, no. 1, p. 1328, 2017.

[19] T.-B. Song, Q. Chen, H. Zhou, C. Jiang, H.-H. Wang, Y. M. Yang, Y. Liu, J. You, and Y. Yang, "Perovskite solar cells: film formation and properties," *Journal of Materials Chemistry A*, vol. 3, no. 17, pp. 9032–9050, 2015.

[20] A. Kulkarni, F. Ciacchi, S. Giddey, C. Munnings, S. Badwal, J. Kimpton, and D. Fini, "Mixed ionic electronic conducting perovskite anode for direct carbon fuel cells," *International Journal of Hydrogen Energy*, vol. 37, no. 24, pp. 19 092–19 102, 2012.

[21] Z. Ahmad, M. A. Najeeb, R. Shakoor, A. Alashraf, S. A. Al-Muhtaseb, A. Soliman, and M. Nazeeruddin, "Instability in ch 3 nh 3 pbi 3 perovskite solar cells due to elemental migration and chemical composition changes," *Scientific reports*, vol. 7, no. 1, p. 15406, 2017.

[22] T. Wu, T. S. Rappaport, and C. M. Collins, "Safe for generations to come: Considerations of safety for millimeter waves in wireless communications," *IEEE microwave magazine*, vol. 16, no. 2, pp. 65–84, 2015.

[23] T. S. Rappaport, Y. Xing, O. Kanhere, S. Ju, A. Madanayake, S. Mandal, A. Alkhateeb, and G. C. Trichopoulos, "Wireless communications and applications above 100 ghz: Opportunities and challenges for 6g and beyond," *IEEE access*, vol. 7, pp. 78 729–78 757, 2019.

[24] P. H. Siegel, "Terahertz technology in biology and medicine," *IEEE transactions on microwave theory and techniques*, vol. 52, no. 10, pp. 2438–2447, 2004.

[25] ——, "Terahertz technology," *IEEE Transactions on microwave theory and techniques*, vol. 50, no. 3, pp. 910–928, 2002.

[26] Z. Jianyong, L. Haiyong, C. Zili, and L. Zhaohui, "Rssi based bluetooth low energy indoor positioning," in *2014 International Conference on Indoor Positioning and Indoor Navigation (IPIN)*. IEEE, 2014, pp. 526–533.

[27] P. Neumann, J. Montavont, and T. Noel, "Indoor deployment of low-power wide area networks (lpwan): A lorawan case study," in *2016 IEEE 12th International Conference on Wireless and Mobile Computing, Networking and Communications (WiMob)*. IEEE, 2016, pp. 1–8.

[28] I. Dey, M. M. Butt, and N. Marchetti, "Throughput analysis for virtual mimo wsns over measured mimo channels," *IEEE Transactions on Instrumentation and Measurement*, vol. 68, no. 1, pp. 297–299, 2018.

[29] F. Khan and Z. Pi, "mmwave mobile broadband (mmb): Unleashing the 3–300ghz spectrum," in *34th IEEE Sarnoff Symposium*. IEEE, 2011, pp. 1–6.

[30] T. Kürner and S. Priebe, "Towards thz communications-status in research, standardization and regulation," *Journal of Infrared, Millimeter, and Terahertz Waves*, vol. 35, no. 1, pp. 53–62, 2014.

[31] K.-C. Huang and Z. Wang, "Terahertz terabit wireless communication," *IEEE Microwave Magazine*, vol. 12, no. 4, pp. 108–116, 2011.

[32] J. A. Shaw, "Radiometry and the friis transmission equation," *American journal of physics*, vol. 81, no. 1, pp. 33–37, 2013.

[33] A. Tamminen, S. Mäkelä, J. Ala-Laurinaho, J. Häkli, P. Koivisto, P. Rantakari, J. Säily, A. Luukanen, and A. V. Räisänen, "Reflectarray design for 120-ghz radar application:

measurement results," *IEEE transactions on antennas and propagation*, vol. 61, no. 10, pp. 5036–5047, 2013.

[34] C. Jansen, S. Priebe, C. Moller, M. Jacob, H. Dierke, M. Koch, and T. Kurner, "Diffuse scattering from rough surfaces in thz communication channels," *IEEE Transactions on Terahertz Science and Technology*, vol. 1, no. 2, pp. 462–472, 2011.

[35] R. Piesiewicz, C. Jansen, D. Mittleman, T. Kleine-Ostmann, M. Koch, and T. Kurner, "Scattering analysis for the modeling of thz communication systems," *IEEE Transactions on Antennas and Propagation*, vol. 55, no. 11, pp. 3002–3009, 2007.

[36] M. Nieto-Vesperinas and J. Soto-Crespo, "Monte carlo simulations for scattering of electromagnetic waves from perfectly conductive random rough surfaces," *Optics letters*, vol. 12, no. 12, pp. 979–981, 1987.

[37] S. Dhillon, M. Vitiello, E. Linfield, A. Davies, M. C. Hoffmann, J. Booske, C. Paoloni, M. Gensch, P. Weightman, G. Williams *et al.*, "The 2017 terahertz science and technology roadmap," *Journal of Physics D: Applied Physics*, vol. 50, no. 4, p. 043001, 2017.

[38] T. Hochrein, "Markets, availability, notice, and technical performance of terahertz systems: Historic development, present, and trends," *Journal of Infrared, Millimeter, and Terahertz Waves*, vol. 36, no. 3, pp. 235–254, 2015.

[39] A. Rogalski and F. Sizov, "Terahertz detectors and focal plane arrays," *Opto-electronics review*, vol. 19, no. 3, pp. 346–404, 2011.

[40] M. Long, P. Wang, H. Fang, and W. Hu, "Progress, challenges, and opportunities for 2d material based photodetectors," *Advanced Functional Materials*, vol. 29, no. 19, p. 1803807, 2019.

[41] P. Gopalan and B. Sensale-Rodriguez, "2d materials for terahertz modulation," *Advanced Optical Materials*, vol. 8, no. 3, p. 1900550, 2020.

[42] L. Sun, W. Wang, and H. Yang, "Recent progress in synaptic devices based on 2d materials," *Advanced Intelligent Systems*, vol. 2, no. 5, p. 1900167, 2020.

[43] Y. Zhang, Y. Huang, T. Zhang, H. Chang, P. Xiao, H. Chen, Z. Huang, and Y. Chen, "Broadband and tunable high-performance microwave absorption of an ultralight and highly compressible graphene foam," *Advanced materials*, vol. 27, no. 12, pp. 2049–2053, 2015.

[44] R. Mas-Balleste, C. Gomez-Navarro, J. Gomez-Herrero, and F. Zamora, "2d materials: to graphene and beyond," *Nanoscale*, vol. 3, no. 1, pp. 20–30, 2011.

[45] A. Chaves, J. G. Azadani, H. Alsalman, D. R. da Costa, R. Frisenda, A. Chaves, S. H. Song, Y. D. Kim, D. He, J. Zhou *et al.*, "Bandgap engineering of two-dimensional semiconductor materials," *npj 2D Materials and Applications*, vol. 4, no. 1, pp. 1–21, 2020.

[46] E. Lee, Y. S. Yoon, and D.-J. Kim, "Two-dimensional transition metal dichalcogenides and metal oxide hybrids for gas sensing," *ACS sensors*, vol. 3, no. 10, pp. 2045–2060, 2018.

[47] A. Baron, S. Larouche, D. J. Gauthier, and D. R. Smith, "Scaling of the nonlinear response of the surface plasmon polariton at a metal/dielectric interface," *JOSA B*, vol. 32, no. 1, pp. 9–14, 2015.

[48] J. Liu, Z. U. Khan, and S. Sarjoghian, "Layered thz waveguides for spps, filter and sensor applications," *Journal of Optics*, vol. 48, no. 4, pp. 567–581, 2019.

[49] A. al Abohmra, H. T. Abbas, M. S. Rabbani, C. Li, A. Alomainy, M. Imran, Q. H. Abbasi *et al.*, "An ultrawideband microfabricated gold-based antenna array for terahertz communication," *IEEE Antennas and Wireless Propagation Letters*, 2021.

[50] A. Fernandez-Dominguez, E. Moreno, L. Martin-Moreno, and F. Garcia-Vidal, "Terahertz wedge plasmon polaritons," *Optics letters*, vol. 34, no. 13, pp. 2063–2065, 2009.

[51] K. Novoselov, o. A. Mishchenko, o. A. Carvalho, and A. C. Neto, "2d materials and van der waals heterostructures," *Science*, vol. 353, no. 6298, 2016.

[52] T. Gould, S. Lebègue, T. Bjørkman, and J. Dobson, "2d structures beyond graphene: The brave new world of layered materials and how computers can help discover them," in *Semiconductors and Semimetals*. Elsevier, 2016, vol. 95, pp. 1–33.

[53] P. Miro, M. Audiffred, and T. Heine, "An atlas of two-dimensional materials," *Chemical Society Reviews*, vol. 43, no. 18, pp. 6537–6554, 2014.

[54] C. L. Holloway, E. F. Kuester, J. A. Gordon, J. O, Hara, J. Booth, and D. R. Smith, "An overview of the theory and applications of metasurfaces: The two-dimensional equivalents of metamaterials," *IEEE Antennas and Propagation Magazine*, vol. 54, no. 2, pp. 10–35, 2012.

[55] B. Kapilevich, Y. Pinhasi, and B. Litvak, "Application of the matched thz power meter for material characterization in free space," in *2011 IEEE International Conference on Microwaves, Communications, Antennas and Electronic Systems (COMCAS 2011)*. IEEE, 2011, pp. 1–4.

[56] G. Hanson, "Radiation efficiency of nano-radius dipole antennas in the microwave and far-infrared regimes," *IEEE Antennas and Propagation Magazine*, vol. 50, no. 3, pp. 66–77, 2008.

[57] A. Ahmadi and H. Mosallaei, "Physical configuration and performance modeling of all-dielectric metamaterials," *Physical Review B*, vol. 77, no. 4, p. 045104, 2008.

[58] G.-H. Lee, Y.-J. Yu, C. Lee, C. Dean, K. L. Shepard, P. Kim, and J. Hone, "Electron tunneling through atomically flat and ultrathin hexagonal boron nitride," *Applied physics letters*, vol. 99, no. 24, p. 243114, 2011.

[59] C. R. Dean, A. F. Young, I. Meric, C. Lee, L. Wang, S. Sorgenfrei, K. Watanabe, T. Taniguchi, P. Kim, K. L. Shepard *et al.*, "Boron nitride substrates for high-quality graphene electronics," *Nature nanotechnology*, vol. 5, no. 10, pp. 722–726, 2010.

[60] C. R. Dean, L. Wang, P. Maher, C. Forsythe, F. Ghahari, Y. Gao, J. Katoch, M. Ishigami, P. Moon, M. Koshino *et al.*, "Hofstadter's butterfly and the fractal quantum hall effect in moiré superlattices," *Nature*, vol. 497, no. 7451, pp. 598–602, 2013.

[61] L. Britnell, R. Gorbachev, R. Jalil, B. Belle, F. Schedin, A. Mishchenko, T. Georgiou, M. Katsnelson, L. Eaves, S. Morozov *et al.*, "Field-effect tunneling transistor based on vertical graphene heterostructures," *Science*, vol. 335, no. 6071, pp. 947–950, 2012.

[62] Y. Hernandez, V. Nicolosi, M. Lotya, F. M. Blighe, Z. Sun, S. De, I. McGovern, B. Holland, M. Byrne, Y. K. Gun'Ko *et al.*, "High-yield production of graphene by liquid-phase exfoliation of graphite," *Nature nanotechnology*, vol. 3, no. 9, pp. 563–568, 2008.

[63] S. Nakamura, M. Senoh, S.-i. Nagahama, N. Iwasa, T. Yamada, T. Matsushita, H. Kiyoku, and Y. Sugimoto, "Ingan-based multi-quantum-well-structure laser diodes," *Japanese Journal of Applied Physics*, vol. 35, no. 1B, p. L74, 1996.

[64] M. Walther, D. Cooke, C. Sherstan, M. Hajar, M. Freeman, and F. Hegmann, "Terahertz conductivity of thin gold films at the metal-insulator percolation transition," *Physical Review B*, vol. 76, no. 12, p. 125408, 2007.

[65] Y. Huang, W.-Y. Yin, and Q. H. Liu, "Performance prediction of carbon nanotube bundle dipole antennas," *IEEE Transactions on Nanotechnology*, vol. 7, no. 3, pp. 331–337, 2008.

[66] T. Seifert, S. Jaiswal, U. Martens, J. Hannegan, L. Braun, P. Maldonado, F. Freimuth, A. Kronenberg, J. Henrizi, I. Radu *et al.*, "Efficient metallic spintronic emitters of ultrabroadband terahertz radiation," *Nature photonics*, vol. 10, no. 7, pp. 483–488, 2016.

[67] N. Laman and D. Grischkowsky, "Terahertz conductivity of thin metal films," *Applied Physics Letters*, vol. 93, no. 5, p. 051105, 2008.

[68] J. Liu, Z. U. Khan, C. Wang, H. Zhang, and S. Sarjoghian, "Review of graphene modulators from the low to the high figure of merits," *Journal of Physics D: Applied Physics*, vol. 53, no. 23, p. 233002, 2020.

[69] S. Singhal, "Cpw fed jasmine shaped superwideband terahertz antenna for pattern diversity applications," *Optik*, vol. 231, p. 166356, 2021.

[70] X. Li, L. Tao, Z. Chen, H. Fang, X. Li, X. Wang, J.-B. Xu, and H. Zhu, "Graphene and related two-dimensional materials: Structure-property relationships for electronics and optoelectronics," *Applied Physics Reviews*, vol. 4, no. 2, p. 021306, 2017.

[71] A. R. Davoyan, V. V. Popov, and S. A. Nikitov, "Tailoring terahertz near-field enhancement via two-dimensional plasmons," *Physical review letters*, vol. 108, no. 12, p. 127401, 2012.

[72] Y. Zhang, Y. Feng, B. Zhu, J. Zhao, and T. Jiang, "Graphene based tunable metamaterial absorber and polarization modulation in terahertz frequency," *Optics express*, vol. 22, no. 19, pp. 22 743–22 752, 2014.

[73] M. Tamagnone, C. Moldovan, J.-M. Poumirol, A. B. Kuzmenko, A. M. Ionescu, J. R. Mosig, and J. Perruisseau-Carrier, "Near optimal graphene terahertz non-reciprocal isolator," *Nature communications*, vol. 7, no. 1, pp. 1–6, 2016.

[74] R. Yan, S. Arezoomandan, B. Sensale-Rodriguez, and H. G. Xing, "Exceptional terahertz wave modulation in graphene enhanced by frequency selective surfaces," *ACS photonics*, vol. 3, no. 3, pp. 315–323, 2016.

[75] A. Vakil and N. Engheta, "Transformation optics using graphene," *Science*, vol. 332, no. 6035, pp. 1291–1294, 2011.

[76] I. Llatser Marti, C. Kremers, D. N. Chigrin, J. M. Jornet Montaña, M. C. Lemme, A. Cabellos Aparicio, and E. J. Alarcon Cot, "Radiation characteristics of tunable graphennas in the terahertz band," *Radioengineering*, vol. 21, no. 4, pp. 1–8, 2012.

[77] G. W. Hanson, "Dyadic green's functions and guided surface waves for a surface conductivity model of graphene," *Journal of Applied Physics*, vol. 103, no. 6, p. 064302, 2008.

[78] S. A. Mikhailov and K. Ziegler, "New electromagnetic mode in graphene," *Physical review letters*, vol. 99, no. 1, p. 016803, 2007.

[79] B. Guzelturk, R. A. Belisle, M. D. Smith, K. Bruening, R. Prasanna, Y. Yuan, V. Gopalan, C. J. Tassone, H. I. Karunadasa, M. D. McGehee *et al.*, "Terahertz emission from hybrid perovskites driven by ultrafast charge separation and strong electron–phonon coupling," *Advanced Materials*, vol. 30, no. 11, p. 1704737, 2018.

[80] A. Kumar, A. Solanki, M. Manjappa, S. Ramesh, Y. K. Srivastava, P. Agarwal, T. C. Sum, and R. Singh, "Excitons in 2d perovskites for ultrafast terahertz photonic devices," *Science advances*, vol. 6, no. 8, p. eaax8821, 2020.

[81] N. K. Noel, A. Abate, S. D. Stranks, E. S. Parrott, V. M. Burlakov, A. Goriely, and H. J. Snaith, "Enhanced photoluminescence and solar cell performance via lewis base passivation of organic–inorganic lead halide perovskites," *ACS nano*, vol. 8, no. 10, pp. 9815–9821, 2014.

[82] M. A. Green, A. Ho-Baillie, and H. J. Snaith, "The emergence of perovskite solar cells," *Nature photonics*, vol. 8, no. 7, pp. 506–514, 2014.

[83] A. Abohmra, H. Abbas, S. F. Jilani, A. Alomainy, M. A. Imran, and Q. H. Abbasi, "High bandwidth perovskite based antenna for high-resolution biomedical imaging at terahertz," in *2019 IEEE International Symposium on Antennas and Propagation and USNC-URSI Radio Science Meeting*. IEEE, 2019, pp. 503–504.

[84] T. Salim, J. Kadro, M.-T. Khuc, R. Haselsberger, L. Cheng, H. Xia, G. G. Gurzadyan, H. Su, Y. M. Lam, R. A. Marcus *et al.*, "Elucidating the role of disorder and free-carrier recombination kinetics in ch 3 nh 3 pbi 3 perovskite films," *Nature communications*, vol. 6, no. 1, pp. 1–8, 2015.

[85] N. Smith, "Classical generalization of the drude formula for the optical conductivity," *Physical Review B*, vol. 64, no. 15, p. 155106, 2001.

[86] Y. Rakita, O. Bar-Elli, E. Meirzadeh, H. Kaslasi, Y. Peleg, G. Hodes, I. Lubomirsky, D. Oron, D. Ehre, and D. Cahen, "Tetragonal ch3nh3pbi3 is ferroelectric," *Proceedings of the National Academy of Sciences*, vol. 114, no. 28, pp. E5504–E5512, 2017.

[87] A. Y. Pawar, D. D. Sonawane, K. B. Erande, and D. V. Derle, "Terahertz technology and its applications," *Drug invention today*, vol. 5, no. 2, pp. 157–163, 2013.

[88] T. Yasuda, T. Yasui, T. Araki, and E. Abraham, "Real-time two-dimensional terahertz tomography of moving objects," *Optics communications*, vol. 267, no. 1, pp. 128–136, 2006.

[89] Y. Huang, L. Zhu, Q. Zhao, Y. Guo, Z. Ren, J. Bai, and X. Xu, "Surface optical rectification from layered mos2 crystal by thz time-domain surface emission spectroscopy," *ACS applied materials & interfaces*, vol. 9, no. 5, pp. 4956–4965, 2017.

[90] L. Cong, Y. K. Srivastava, A. Solanki, T. C. Sum, and R. Singh, "Perovskite as a platform for active flexible metaphotonic devices," *Acs Photonics*, vol. 4, no. 7, pp. 1595–1601, 2017.

[91] J. Lou, J. Liang, Y. Yu, H. Ma, R. Yang, Y. Fan, G. Wang, and T. Cai, "Silicon-based terahertz meta-devices for electrical modulation of fano resonance and transmission amplitude," *Advanced Optical Materials*, vol. 8, no. 19, p. 2000449, 2020.

[92] R. Friend and A. Yoffe, "Electronic properties of intercalation complexes of the transition metal dichalcogenides," *Advances in Physics*, vol. 36, no. 1, pp. 1–94, 1987.

[93] X. Hong, J. Kim, S.-F. Shi, Y. Zhang, C. Jin, Y. Sun, S. Tongay, J. Wu, Y. Zhang, and F. Wang, "Ultrafast charge transfer in atomically thin mos 2/ws 2 heterostructures," *Nature nanotechnology*, vol. 9, no. 9, pp. 682–686, 2014.

[94] C.-H. Lee, G.-H. Lee, A. M. Van Der Zande, W. Chen, Y. Li, M. Han, X. Cui, G. Arefe, C. Nuckolls, T. F. Heinz *et al.*, "Atomically thin p–n junctions with van der waals heterointerfaces," *Nature nanotechnology*, vol. 9, no. 9, pp. 676–681, 2014.

[95] M. M. Furchi, A. Pospischil, J. Libisch, Florian, and T. Mueller, "Photovoltaic effect in an electrically tunable van der waals heterojunction," *Nano letters*, vol. 14, no. 8, pp. 4785–4791, 2014.

[96] K. S. Novoselov, D. Jiang, F. Schedin, T. Booth, V. Khotkevich, S. Morozov, and A. K. Geim, "Two-dimensional atomic crystals," *Proceedings of the National Academy of Sciences*, vol. 102, no. 30, pp. 10 451–10 453, 2005.

[97] H. Wang, L. Yu, Y.-H. Lee, Y. Shi, A. Hsu, M. L. Chin, L.-J. Li, M. Dubey, J. Kong, and T. Palacios, "Integrated circuits based on bilayer mos2 transistors," *Nano letters*, vol. 12, no. 9, pp. 4674–4680, 2012.

[98] K. Kaasbjerg, K. S. Thygesen, and K. W. Jacobsen, "Phonon-limited mobility in n-type single-layer mos 2 from first principles," *Physical Review B*, vol. 85, no. 11, p. 115317, 2012.

[99] H. Shi, H. Pan, Y.-W. Zhang, and B. I. Yakobson, "Quasiparticle band structures and optical properties of strained monolayer mos 2 and ws 2," *Physical Review B*, vol. 87, no. 15, p. 155304, 2013.

[100] Y. Kang, S. Najmaei, Z. Liu, Y. Bao, Y. Wang, X. Zhu, N. J. Halas, P. Nordlander, P. M. Ajayan, J. Lou *et al.*, "Plasmonic hot electron induced structural phase transition in a mos2 monolayer," *Advanced Materials*, vol. 26, no. 37, pp. 6467–6471, 2014.

[101] L. Tao, K. Chen, Z. Chen, C. Cong, C. Qiu, J. Chen, X. Wang, H. Chen, T. Yu, W. Xie *et al.*, "1t transition metal telluride atomic layers for plasmon-free sers at femtomolar levels," *Journal of the American Chemical Society*, vol. 140, no. 28, pp. 8696–8704, 2018.

[102] C. J. Docherty, P. Parkinson, H. J. Joyce, M.-H. Chiu, C.-H. Chen, M.-Y. Lee, L.-J. Li, L. M. Herz, and M. B. Johnston, "Ultrafast transient terahertz conductivity of monolayer mos2 and wse2 grown by chemical vapor deposition," *ACS nano*, vol. 8, no. 11, pp. 11 147–11 153, 2014.

[103] M. Dragoman, A. Muller, D. Dragoman, F. Coccetti, and R. Plana, "Terahertz antenna based on graphene," *Journal of Applied Physics*, vol. 107, no. 10, p. 104313, 2010.

[104] I. Llatser, C. Kremers, A. Cabellos-Aparicio, J. M. Jornet, E. Alarcón, and D. N. Chigrin, "Graphene-based nano-patch antenna for terahertz radiation," *Photonics and Nanostructures-Fundamentals and Applications*, vol. 10, no. 4, pp. 353–358, 2012.

[105] W. Xu, L. Xie, J. Zhu, L. Tang, R. Singh, C. Wang, Y. Ma, H.-T. Chen, and Y. Ying, "Terahertz biosensing with a graphene-metamaterial heterostructure platform," *Carbon*, vol. 141, pp. 247–252, 2019.

[106] S. E. Hosseininejad, K. Rouhi, M. Neshat, R. Faraji-Dana, A. Cabellos-Aparicio, S. Abadal, and E. Alarcon, "Reprogrammable graphene-based metasurface mirror with adaptive focal point for thz imaging," *Scientific reports*, vol. 9, no. 1, pp. 1–9, 2019.

[107] L. Vicarelli, M. Vitiello, D. Coquillat, A. Lombardo, A. C. Ferrari, W. Knap, M. Polini, V. Pellegrini, and A. Tredicucci, "Graphene field-effect transistors as room-temperature terahertz detectors," *Nature materials*, vol. 11, no. 10, pp. 865–871, 2012.

[108] J. Gomez-Diaz, M. Esquius-Morote, and J. Perruisseau-Carrier, "Plane wave excitation-detection of non-resonant plasmons along finite-width graphene strips," *Optics express*, vol. 21, no. 21, pp. 24 856–24 872, 2013.

[109] W. Zheng, F. Fan, M. Chen, S. Chen, and S.-J. Chang, "Optically pumped terahertz wave modulation in mos2-si heterostructure metasurface," *AIP Advances*, vol. 6, no. 7, p. 075105, 2016.

[110] Y. Huang, L. Zhu, Z. Yao, L. Zhang, C. He, Q. Zhao, J. Bai, and X. Xu, "Terahertz surface emission from layered mos2 crystal: competition between surface optical rectification and surface photocurrent surge," *The Journal of Physical Chemistry C*, vol. 122, no. 1, pp. 481–488, 2018.

[111] Y. Zhong, Y. Huang, S. Zhong, T. Lin, M. Luo, Y. Shen, and J. Ding, "Tunable terahertz broadband absorber based on mos2 ring-cross array structure," *Optical Materials*, vol. 114, p. 110996, 2021.

[112] A. Abohmra, H. Abbas, M. Al-Hasan, I. B. Mabrouk, A. Alomainy, M. A. Imran, and Q. H. Abbasi, "Terahertz antenna array based on a hybrid perovskite structure," *IEEE Open Journal of Antennas and Propagation*, vol. 1, pp. 464–471, 2020.

[113] K.-S. Lee, R. Kang, B. Son, D.-Y. Kim, N. E. Yu, and D.-K. Ko, "All-optical thz wave switching based on ch 3 nh 3 pbi 3 perovskites," *Scientific reports*, vol. 6, p. 37912, 2016.

[114] J. Zhou, Y. Hu, T. Jiang, H. Ouyang, H. Li, Y. Sui, H. Hao, J. You, X. Zheng, Z. Xu *et al.*, "Ultrasensitive polarization-dependent terahertz modulation in hybrid perovskites plasmon-induced transparency devices," *Photonics Research*, vol. 7, no. 9, pp. 994–1002, 2019.

[115] V. W. Brar, M. S. Jang, M. Sherrott, S. Kim, J. J. Lopez, L. B. Kim, M. Choi, and H. Atwater, "Hybrid surface-phonon-plasmon polariton modes in graphene/monolayer h-bn heterostructures," *Nano letters*, vol. 14, no. 7, pp. 3876–3880, 2014.

[116] Y. Cao, S. Gan, Z. Geng, J. Liu, Y. Yang, Q. Bao, and H. Chen, "Optically tuned terahertz modulator based on annealed multilayer mos 2," *Scientific reports*, vol. 6, no. 1, pp. 1–9, 2016.

[117] M. G. Ahangari, A. Salmankhani, A. H. Imani, N. Shahab, and A. H. Mashhadzadeh, "Density functional theory study on the mechanical properties and interlayer interactions of multi-layer graphene: carbonic, silicon-carbide and silicene graphene-like structures," *Silicon*, vol. 11, no. 3, pp. 1235–1246, 2019.

[118] L. Yu, D. Liu, X.-Z. Qi, X. Xiong, L.-T. Feng, M. Li, G.-P. Guo, G.-C. Guo, and X.-F. Ren, "Gap plasmon-enhanced photoluminescence of monolayer mos2 in hybrid nanostructure," *Chinese Physics B*, vol. 27, no. 4, p. 047302, 2018.

[119] S. Najmaei, Z. Liu, W. Zhou, X. Zou, G. Shi, S. Lei, B. I. Yakobson, J.-C. Idrobo, P. M. Ajayan, and J. Lou, "Vapour phase growth and grain boundary structure of molybdenum disulphide atomic layers," *Nature materials*, vol. 12, no. 8, pp. 754–759, 2013.

[120] A. Locatelli, G. E. Town, and C. De Angelis, "Graphene-based terahertz waveguide modulators," *IEEE Transactions on Terahertz Science and Technology*, vol. 5, no. 3, pp. 351–357, 2015.

[121] B. Wu, Y. Hu, Y. T. Zhao, W. B. Lu, and W. Zhang, "Large angle beam steering thz antenna using active frequency selective surface based on hybrid graphene-gold structure," *Optics express*, vol. 26, no. 12, pp. 15 353–15 361, 2018.

[122] L. Deng, Y. Wu, C. Zhang, W. Hong, B. Peng, J. Zhu, and S. Li, "Manipulating of different-polarized reflected waves with graphene-based plasmonic metasurfaces in terahertz regime," *Scientific reports*, vol. 7, no. 1, pp. 1–10, 2017.

[123] F. Bonaccorso, Z. Sun, T. Hasan, and A. Ferrari, "Graphene photonics and optoelectronics," *Nature photonics*, vol. 4, no. 9, pp. 611–622, 2010.

[124] R. H. Ritchie, "Plasma losses by fast electrons in thin films," *Physical review*, vol. 106, no. 5, p. 874, 1957.

[125] A. Otto, "Excitation of nonradiative surface plasma waves in silver by the method of frustrated total reflection," *Zeitschrift fur Physik A Hadrons and nuclei*, vol. 216, no. 4, pp. 398–410, 1968.

[126] H. Raether, "Surface plasmons on gratings," in *Surface plasmons on smooth and rough surfaces and on gratings*. Springer, 1988, pp. 91–116.

[127] D. G. Myszka, "Survey of the 1998 optical biosensor literature," *Journal of Molecular Recognition*, vol. 12, no. 6, pp. 390–408, 1999.

[128] R. C. Jorgenson and S. S. Yee, "A fiber-optic chemical sensor based on surface plasmon resonance," *Sensors and Actuators B: Chemical*, vol. 12, no. 3, pp. 213–220, 1993.

[129] S. Lal, N. K. Grady, J. Kundu, C. S. Levin, J. B. Lassiter, and N. J. Halas, "Tailoring plasmonic substrates for surface enhanced spectroscopies," *Chemical Society Reviews*, vol. 37, no. 5, pp. 898–911, 2008.

[130] C. Suessmeier, S. Abadal, D. Stock, S. Schaeffer, E. Alarcon, S. E. Hosseininejad, A. K. Wigger, S. Wagner, A. Cabellos-Aparicio, M. Lemme *et al.*, "Material-dependencies of the thz emission from plasmonic graphene-based photoconductive antenna structures," in *2017 42nd International Conference on Infrared, Millimeter, and Terahertz Waves (IRMMW-THz)*. IEEE, 2021, pp. 1–2.

[131] K. I. Bolotin, K. J. Sikes, Z. Jiang, M. Klima, G. Fudenberg, J. Hone, P. Kim, and H. Stormer, "Ultrahigh electron mobility in suspended graphene," *Solid state communications*, vol. 146, no. 9-10, pp. 351–355, 2008.

[132] H. Hirai, H. Tsuchiya, Y. Kamakura, N. Mori, and M. Ogawa, "Electron mobility calculation for graphene on substrates," *Journal of Applied Physics*, vol. 116, no. 8, p. 083703, 2014.

[133] J.-S. G. Hong and M. J. Lancaster, *Microstrip filters for RF/microwave applications*. John Wiley & Sons, 2004, vol. 167.

[134] S. Yoo, A. Kalatzis, N. Amini, Z. Ye, and M. Pourhomayoun, "Interactive predictive analytics for enhancing patient adherence in remote health monitoring," in *Proceedings of the 8th ACM MobiHoc 2018 Workshop on Pervasive Wireless Healthcare Workshop*, 2018, pp. 1–6.

[135] N. Kalid, A. Zaidan, B. Zaidan, O. H. Salman, M. Hashim, and H. Muzammil, "Based real time remote health monitoring systems: A review on patients prioritization and related big data using body sensors information and communication technology," *Journal of medical systems*, vol. 42, no. 2, p. 30, 2018.

[136] N. Mohammadzadeh and R. Safdari, "Patient monitoring in mobile health: opportunities and challenges," *Medical Archives*, vol. 68, no. 1, p. 57, 2014.

[137] R. Negra, I. Jemili, and A. Belghith, "Wireless body area networks: Applications and technologies," *Procedia Computer Science*, vol. 83, pp. 1274–1281, 2016.

[138] M. Totaro, T. Poliero, A. Mondini, C. Lucarotti, G. Cairoli, J. Ortiz, and L. Beccai, "Soft smart garments for lower limb joint position analysis," *Sensors*, vol. 17, no. 10, p. 2314, 2017.

[139] V. Custodio, F. J. Herrera, G. Lopez, and J. I. Moreno, "A review on architectures and communications technologies for wearable health-monitoring systems," *Sensors*, vol. 12, no. 10, pp. 13 907–13 946, 2012.

[140] M. S. Islam, M. I. Ibrahimy, S. Motakabber, A. Z. Hossain, and S. K. Azam, "Microstrip patch antenna with defected ground structure for biomedical application," *Bulletin of Electrical Engineering and Informatics*, vol. 8, no. 2, pp. 586–595, 2019.

[141] H. R. Khaleel, H. M. Al-Rizzo, A. I. Abbosh, and A. Kishk, "Design, fabrication, and testing of flexible antennas," *Advancement in Microstrip Antennas with Recent Applications*, pp. 363–383, 2013.

[142] G. Shoemaker, T. Tsukitani, Y. Kitamura, and K. S. Booth, "Body-centric interaction techniques for very large wall displays," in *Proceedings of the 6th Nordic Conference on Human-Computer Interaction: Extending Boundaries*, 2010, pp. 463–472.

[143] R. Bharadwaj, C. Parini, S. K. Koul, and A. Alomainy, "Effect of limb movements on compact uwb wearable antenna radiation performance for healthcare monitoring," *Progress In Electromagnetics Research C*, vol. 91, pp. 15–26, 2019.

[144] S. K. Jain, N. Baviskar, N. Golait, and S. Jain, "Design of wearable antenna for various applications," *Antenna Test & Measurement Society (ATMS India-18)*, pp. 2–6, 2018.

[145] D. E. Anagnostou, A. A. Gheethan, A. K. Amert, and K. W. Whites, "A direct-write printed antenna on paper-based organic substrate for flexible displays and wlan applications," *Journal of Display Technology*, vol. 6, no. 11, pp. 558–564, 2010.

[146] P. S. Hall and Y. Hao, "Antennas and propagation for body centric communications," in *2006 First European Conference on Antennas and Propagation*. IEEE, 2006, pp. 1–7.

[147] M. Klemm and G. Troester, "Textile uwb antennas for wireless body area networks," *IEEE Transactions on Antennas and propagation*, vol. 54, no. 11, pp. 3192–3197, 2006.

[148] G. Piro, K. Yang, G. Boggia, N. Chopra, L. A. Grieco, and A. Alomainy, "Terahertz communications in human tissues at the nanoscale for healthcare applications," *IEEE Transactions on Nanotechnology*, vol. 14, no. 3, pp. 404–406, 2015.

[149] I. F. Akyildiz and J. M. Jornet, "Electromagnetic wireless nanosensor networks," *Nano Communication Networks*, vol. 1, no. 1, pp. 3–19, 2010.

[150] R. Zhang, K. Yang, Q. H. Abbasi, K. A. Qaraqe, and A. Alomainy, "Analytical modelling of the effect of noise on the terahertz in-vivo communication channel for body-centric nano-networks," *Nano communication networks*, vol. 15, pp. 59–68, 2018.

[151] G. J. L. Hernandez, "Wearable technology: Shaping market opportunities through innovation, learning, and networking," in *Reverse Entrepreneurship in Latin America*. Springer, 2019, pp. 29–44.

[152] C. Flynn, A. Taberner, and P. Nielsen, "Modeling the mechanical response of in vivo human skin under a rich set of deformations," *Annals of biomedical engineering*, vol. 39, no. 7, pp. 1935–1946, 2011.

[153] S. Alekseev and M. Ziskin, "Human skin permittivity determined by millimeter wave reflection measurements," *Bioelectromagnetics: Journal of the Bioelectromagnetics Society, The Society for Physical Regulation in Biology and Medicine, The European Bioelectromagnetics Association*, vol. 28, no. 5, pp. 331–339, 2007.

[154] S. E. Lynch, R. B. Colvin, H. N. Antoniades *et al.*, "Growth factors in wound healing. single and synergistic effects on partial thickness porcine skin wounds." *The Journal of clinical investigation*, vol. 84, no. 2, pp. 640–646, 1989.

[155] M. Dashti and J. D. Carey, "Graphene microstrip patch ultrawide band antennas for thz communications," *Advanced Functional Materials*, vol. 28, no. 11, p. 1705925, 2018.

[156] K. Yaws, D. Mixon, and W. Roach, "Electromagnetic properties of tissue in the optical region," in *Optical Interactions with Tissue and Cells XVIII*, vol. 6435. International Society for Optics and Photonics, 2007, p. 643507.

[157] E. Pickwell, B. Cole, A. Fitzgerald, V. Wallace, and M. Pepper, "Simulation of terahertz pulse propagation in biological systems," *Applied Physics Letters*, vol. 84, no. 12, pp. 2190–2192, 2004.

[158] E. Pickwell, B. E. Cole, A. J. Fitzgerald, M. Pepper, and V. P. Wallace, "In vivo study of human skin using pulsed terahertz radiation," *Physics in Medicine & Biology*, vol. 49, no. 9, p. 1595, 2004.

[159] N. Chopra, K. Yang, Q. H. Abbasi, K. A. Qaraqe, M. Philpott, and A. Alomainy, "Thz time-domain spectroscopy of human skin tissue for in-body nanonetworks," *IEEE Transactions on Terahertz Science and Technology*, vol. 6, no. 6, pp. 803–809, 2016.

[160] R. Bancroft, "Design of an integrated loop coupler and loop antenna for rfid applications," *Microwave and Optical Technology Letters*, vol. 51, no. 8, pp. 1830–1833, 2009.

[161] C. A. Balanis, *Modern antenna handbook.* John Wiley & Sons, 2011.

[162] L. Verma, M. Fakharzadeh, and S. Choi, "Wifi on steroids: 802.11 ac and 802.11 ad," *IEEE Wireless Communications*, vol. 20, no. 6, pp. 30–35, 2013.

[163] B. Biglarbegian, M. Fakharzadeh, D. Busuioc, M.-R. Nezhad-Ahmadi, and S. Safavi-Naeini, "Optimized microstrip antenna arrays for emerging millimeter-wave wireless applications," *IEEE Transactions on antennas and propagation*, vol. 59, no. 5, pp. 1742–1747, 2011.

[164] A. M. Qasim and T. A. Rahman, "A compact & high gain series array planar antenna for 60-ghz wpan applications," in *2010 IEEE Asia-Pacific Conference on Applied Electromagnetics (APACE)*. IEEE, 2010, pp. 1–5.

[165] M. Grätzel, "The light and shade of perovskite solar cells," *Nature Materials*, vol. 13, no. 9, pp. 838–842, Sep 2014. [Online]. Available: http://www.nature.com/articles/nmat4065

[166] C. Randall, A. Bhalla, T. Shrout, and L. Cross, "Classification and consequences of complex lead perovskite ferroelectrics with regard to b-site cation order," *Journal of Materials Research*, vol. 5, no. 4, pp. 829–834, 1990.

[167] Y. Yamada, T. Nakamura, M. Endo, A. Wakamiya, and Y. Kanemitsu, "Photocarrier Recombination Dynamics in Perovskite CH $_3$ NH $_3$ PbI $_3$ for Solar Cell Applications," *Journal of the American Chemical Society*, vol. 136, no. 33, pp. 11 610–11 613, Aug 2014. [Online]. Available: https://pubs.acs.org/doi/10.1021/ja506624n

[168] J.-S. Hong and M. J. Lancaster, *Microstrip Filters for RF/Microwave Applications*. New York, USA: John Wiley & Sons, Inc., Jun 2001. [Online]. Available: http://doi.wiley.com/10.1002/0471221619

[169] B. Radisavljevic, A. Radenovic, J. Brivio, V. Giacometti, and A. Kis, "Single-layer mos 2 transistors," *Nature nanotechnology*, vol. 6, no. 3, pp. 147–150, 2011.

[170] B. Radisavljevic, M. B. Whitwick, and A. Kis, "Integrated circuits and logic operations based on single-layer mos2," *ACS nano*, vol. 5, no. 12, pp. 9934–9938, 2011.

[171] C. Altavilla, M. Sarno, and P. Ciambelli, "A novel wet chemistry approach for the synthesis of hybrid 2d free-floating single or multilayer nanosheets of ms2 oleylamine (m mo, w)," *Chemistry of Materials*, vol. 23, no. 17, pp. 3879–3885, 2011.

[172] Y.-H. Lee, X.-Q. Zhang, W. Zhang, M.-T. Chang, C.-T. Lin, K.-D. Chang, Y.-C. Yu, J. T.-W. Wang, C.-S. Chang, L.-J. Li *et al.*, "Synthesis of large-area mos2 atomic layers with chemical vapor deposition," *Advanced materials*, vol. 24, no. 17, pp. 2320–2325, 2012.

[173] Y.-H. Lee, L. Yu, H. Wang, W. Fang, X. Ling, Y. Shi, C.-T. Lin, J.-K. Huang, M.-T. Chang, C.-S. Chang *et al.*, "Synthesis and transfer of single-layer transition metal disulfides on diverse surfaces," *Nano letters*, vol. 13, no. 4, pp. 1852–1857, 2013.

[174] Z. Tao, L. Huang, and H. Dong, "Surface plasmon polaritons in mos 2 nanostructures," *Brazilian Journal of Physics*, vol. 48, no. 6, pp. 604–607, 2018.

[175] P. Cerwall, P. Jonsson, R. Maller, S. Bavertoft, S. Carson, I. Godor *et al.*, "Ericsson mobility report - june 2020," Ericsson, SE-164 80 Stockholm, Sweden, Tech. Rep., Jun 2020.

[176] M. Koch, "Terahertz communications: A 2020 vision," in *Terahertz frequency detection and identification of materials and objects*. Springer, 2007, pp. 325–338.

[177] J. Laskar, S. Pinel, D. Dawn, S. Sarkar, B. Perumana, and P. Sen, "The next wireless wave is a millimeter wave," *Microwave Journal*, vol. 50, no. 8, p. 22, 2007, publisher: Citeseer.

[178] J. M. Jornet and I. F. Akyildiz, "Graphene-based Plasmonic Nano-Antenna for Terahertz Band Communication in Nanonetworks," *IEEE Journal on Selected Areas in Communications*, vol. 31, no. 12, pp. 685–694, Dec. 2013.

[179] P. H. Siegel, "Terahertz technology in biology and medicine," *IEEE transactions on microwave theory and techniques*, vol. 52, no. 10, pp. 2438–2447, 2004, publisher: IEEE.

[180] A. J. Fitzgerald, E. Berry, N. N. Zinovev, G. C. Walker, M. A. Smith, and J. M. Chamberlain, "An introduction to medical imaging with coherent terahertz frequency radiation," *Physics in Medicine & Biology*, vol. 47, no. 7, p. R67, 2002, publisher: IOP Publishing.

[181] M. K. Choi, K. Taylor, A. Bettermann, and D. W. Van der Weide, “Broadband 10–300 GHz stimulus-response sensing for chemical and biological entities,” *Physics in Medicine & Biology*, vol. 47, no. 21, p. 3777, 2002, publisher: IOP Publishing.

[182] G.-J. Kim, W.-K. Han, J.-I. Kim, and S.-G. Jeon, “High resolution terahertz imaging (T-ray) with a horn antenna,” in *35th International Conference on Infrared, Millimeter, and Terahertz Waves*. IEEE, 2010, pp. 1–2.

[183] D. L. Woolard, J. O. Jensen, and R. J. Hwu, *Terahertz science and technology for military and security applications*. world scientific, 2007, vol. 46.

[184] R. E. Cofield and P. C. Stek, “Design and field-of-view calibration of 114-660-GHz optics of the Earth observing system microwave limb sounder,” *IEEE transactions on geoscience and remote sensing*, vol. 44, no. 5, pp. 1166–1181, 2006, publisher: IEEE.

[185] P. H. Siegel, “THz instruments for space,” *IEEE Transactions on Antennas and Propagation*, vol. 55, no. 11, pp. 2957–2965, 2007, publisher: IEEE.

[186] M. Tonouchi, “Cutting-edge terahertz technology,” *Nature photonics*, vol. 1, no. 2, pp. 97–105, 2007, publisher: Nature Publishing Group.

[187] D. L. Woolard, R. Brown, M. Pepper, and M. Kemp, “Terahertz frequency sensing and imaging: A time of reckoning future applications?” *Proceedings of the IEEE*, vol. 93, no. 10, pp. 1722–1743, 2005, publisher: IEEE.

[188] G. P. Williams, “Filling the THz gap—high power sources and applications,” *Reports on Progress in Physics*, vol. 69, no. 2, p. 301, 2005, publisher: IOP Publishing.

[189] K.-M. Luk, S.-F. Zhou, Y. J. Li, F. Wu, K.-B. Ng, C.-H. Chan, and S. W. Pang, “A microfabricated low-profile wideband antenna array for terahertz communications,” *Scientific reports*, vol. 7, no. 1, pp. 1–11, 2017, publisher: Nature Publishing Group.

[190] D.-K. Lee, J.-H. Kang, J.-S. Lee, H.-S. Kim, C. Kim, J. H. Kim, T. Lee, J.-H. Son, Q.-H. Park, and M. Seo, “Highly sensitive and selective sugar detection by terahertz nano-antennas,” *Scientific reports*, vol. 5, no. 1, pp. 1–7, 2015, publisher: Nature Publishing Group.

[191] L. Razzari, A. Toma, M. Clerici, M. Shalaby, G. Das, C. Liberale, M. Chirumamilla, R. P. Zaccaria, F. De Angelis, and M. Peccianti, “Terahertz dipole nanoantenna arrays: resonance characteristics,” *Plasmonics*, vol. 8, no. 1, pp. 133–138, 2013, publisher: Springer.

[192] D. Gray, J. W. Lu, and D. V. Thiel, “Electronically steerable Yagi-Uda microstrip patch antenna array,” *IEEE Transactions on antennas and propagation*, vol. 46, no. 5, pp. 605–608, 1998, publisher: IEEE.

[193] C. Feuillet-Palma, Y. Todorov, A. Vasanelli, and C. Sirtori, "Strong near field enhancement in THz nano-antenna arrays," *Scientific reports*, vol. 3, no. 1, pp. 1–8, 2013, publisher: Nature Publishing Group.

[194] K. Sengupta and A. Hajimiri, "A 0.28 THz power-generation and beam-steering array in CMOS based on distributed active radiators," *IEEE Journal of Solid-State Circuits*, vol. 47, no. 12, pp. 3013–3031, 2012, publisher: IEEE.

[195] F. Caster II, L. Gilreath, S. Pan, Z. Wang, F. Capolino, and P. Heydari, "Design and analysis of a W-band 9-element imaging array receiver using spatial-overlapping super-pixels in silicon," *IEEE Journal of Solid-State Circuits*, vol. 49, no. 6, pp. 1317–1332, 2014, publisher: IEEE.

[196] E. Brown, A. Lee, B. Navi, and J. Bjarnason, "Characterization of a planar self-complementary square-spiral antenna in the thz region," *Microwave and optical technology letters*, vol. 48, no. 3, pp. 524–529, 2006.

[197] D. F. Filipovic, S. S. Gearhart, and G. M. Rebeiz, "Double-slot antennas on extended hemispherical and elliptical silicon dielectric lenses," *IEEE Transactions on Microwave Theory and Techniques*, vol. 41, no. 10, pp. 1738–1749, Oct. 1993.

[198] G. M. Rebeiz, D. P. Kasilingam, Y. Guo, P. A. Stimson, and D. B. Rutledge, "Monolithic millimeter-wave two-dimensional horn imaging arrays," *IEEE Transactions on Antennas and Propagation*, vol. 38, no. 9, pp. 1473–1482, Sep. 1990.

[199] R. Hincapie and J. E. Sierra, *Advanced Transmission Techniques in WiMAX*. BoD–Books on Demand, 2012.

[200] S.-Y. Suh, W. L. Stutzman, and W. A. Davis, "A new ultrawideband printed monopole antenna: The planar inverted cone antenna (pica)," *IEEE Transactions on Antennas and Propagation*, vol. 52, no. 5, pp. 1361–1364, 2004.

[201] S.-Y. Suh, W. Stutzman, W. Davis, A. Waltho, and J. Schiffer, "A novel cpw-fed disc antenna," in *IEEE Antennas and Propagation Society Symposium, 2004.*, vol. 3. IEEE, 2004, pp. 2919–2922.

[202] M. Altissimo, "E-beam lithography for micro-/nanofabrication," *Biomicrofluidics*, vol. 4, no. 2, p. 026503, 2010.

[203] A. A. Tseng, K. Chen, C. D. Chen, and K. J. Ma, "Electron beam lithography in nanoscale fabrication: recent development," *IEEE Transactions on electronics packaging manufacturing*, vol. 26, no. 2, pp. 141–149, 2003.

[204] M. Angelopoulos, J. M. Shaw, R. D. Kaplan, and S. Perreault, “Conducting polyanilines: Discharge layers for electron-beam lithography,” *Journal of Vacuum Science & Technology B: Microelectronics Processing and Phenomena*, vol. 7, no. 6, pp. 1519–1523, 1989.

[205] S.-Y. Suh, “A Comprehensive Investigation of New Planar Wideband Antennas,” Ph.D. dissertation, Virginia Polytechnic Institute and State University, Jul. 2002. [Online]. Available: https://vtechworks.lib.vt.edu/handle/10919/28801

[206] A. Abohmra, H. Abbas, M. Al-Hasan, I. B. Mabrouk, A. Alomainy, M. A. Imran, and Q. H. Abbasi, “Terahertz Antenna Array Based on a Hybrid Perovskite Structure,” *IEEE Open Journal of Antennas and Propagation*, vol. 1, pp. 464–471, 2020.

[207] A. R. Conn, N. I. M. Gould, and P. L. Toint, *Trust-region methods*, ser. MPS-SIAM series on optimization. Philadelphia, PA: Society for Industrial and Applied Mathematics, 2000.

[208] J. R. James, P. S. Hall, and C. Wood, *Microstrip antenna: Theory and Design*, ser. IEE electromagnetic waves series. London: Peregrinus on behalf of the Institution of Electrical Engineers, 1986, no. 12.

[209] A. V. Kabashin, P. Delaporte, A. Pereira, D. Grojo, R. Torres, T. Sarnet, and M. Sentis, “Nanofabrication with pulsed lasers,” *Nanoscale research letters*, vol. 5, no. 3, p. 454, 2010.

[210] T. J. Reck, L. Chen, C. Zhang, A. Arsenovic, C. Groppi, A. W. Lichtenberger, R. M. Weikle, and N. S. Barker, “Micromachined probes for submillimeter-wave on-wafer measurements—part i: Mechanical design and characterization,” *IEEE Transactions on Terahertz Science and Technology*, vol. 1, no. 2, pp. 349–356, 2011.

[211] D. F. Williams, R. B. Marks, and A. Davidson, “Comparison of on-wafer calibrations,” in *38th ARFTG Conference Digest*, vol. 20. IEEE, 1991, pp. 68–81.

[212] B. T. Rosner, T. Bork, V. Agrawal, and D. W. van der Weide, “Microfabricated silicon coaxial field sensors for near-field scanning optical and microwave microscopy,” *Sensors and Actuators A: Physical*, vol. 102, no. 1-2, pp. 185–194, 2002.

[213] L. Chen, C. Zhang, T. J. Reck, A. Arsenovic, M. Bauwens, C. Groppi, A. W. Lichtenberger, R. M. Weikle, and N. S. Barker, “Terahertz micromachined on-wafer probes: Repeatability and reliability,” *IEEE Transactions on Microwave Theory and Techniques*, vol. 60, no. 9, pp. 2894–2902, 2012.

[214] T. J. Reck, L. Chen, C. Zhang, C. Groppi, H. Xu, A. Arsenovic, N. S. Barker, A. Lichtenberger, and R. M. Weikle, “Micromachined on-wafer probes,” in *2010 IEEE MTT-S International Microwave Symposium*. IEEE, 2010, pp. 65–68.

[215] P. C. Planken, H.-K. Nienhuys, H. J. Bakker, and T. Wenckebach, "Measurement and calculation of the orientation dependence of terahertz pulse detection in znte," *JOSA B*, vol. 18, no. 3, pp. 313–317, 2001.

[216] Q. Yu, M. F. Bauwens, C. Zhang, A. W. Lichtenberger, R. M. Weikle, and N. S. Barker, "Improved micromachined terahertz on-wafer probe using integrated strain sensor," *IEEE transactions on microwave theory and techniques*, vol. 61, no. 12, pp. 4613–4620, 2013.

[217] A. Rumiantsev, R. Doerner, and E. M. Godshalk, "The influence of calibration substrate boundary conditions on cpw characteristics and calibration accuracy at mm-wave frequencies," in *2008 72nd ARFTG Microwave Measurement Symposium*. IEEE, 2008, pp. 168–173.

[218] M. Bauwens, L. Chen, C. Zhang, A. Arsenovic, A. Lichtenberger, N. S. Barker, and R. M. Weikle, "A terahertz micromachined on-wafer probe for wr-1.2 waveguide," in *2012 7th European Microwave Integrated Circuit Conference*. IEEE, 2012, pp. 88–91.

[219] M. Potereau, C. Raya, M. De Matos, S. Fregonese, A. Curutchet, M. Zhang, B. Ardouin, T. Zimmer *et al.*, "Limitations of on-wafer calibration and de-embedding methods in the sub-thz range," *Journal of Computer and Communications*, vol. 1, no. 06, p. 25, 2013.

[220] Y. H. Hu, H. Wang, and B. Hu, "Thinnest two-dimensional nanomaterial—graphene for solar energy," *ChemSusChem*, vol. 3, no. 7, pp. 782–796, 2010.

[221] C. e. e. Rao, A. e. Sood, K. e. Subrahmanyam, and A. Govindaraj, "Graphene: the new two-dimensional nanomaterial," *Angewandte Chemie International Edition*, vol. 48, no. 42, pp. 7752–7777, 2009.

[222] F. Perreault, A. F. De Faria, and M. Elimelech, "Environmental applications of graphene-based nanomaterials," *Chemical Society Reviews*, vol. 44, no. 16, pp. 5861–5896, 2015.

[223] M. Pumera, "Graphene-based nanomaterials and their electrochemistry," *Chemical Society Reviews*, vol. 39, no. 11, pp. 4146–4157, 2010.

[224] P. R. Somani, S. P. Somani, and M. Umeno, "Planer nano-graphenes from camphor by cvd," *Chemical Physics Letters*, vol. 430, no. 1-3, pp. 56–59, 2006.

[225] M. Batzill, "The surface science of graphene: Metal interfaces, cvd synthesis, nanoribbons, chemical modifications, and defects," *Surface Science Reports*, vol. 67, no. 3-4, pp. 83–115, 2012.

[226] R. Munoz and C. Gomez-Aleixandre, "Review of cvd synthesis of graphene," *Chemical Vapor Deposition*, vol. 19, no. 10-11-12, pp. 297–322, 2013.

[227] W. Kong, H. Kum, S.-H. Bae, J. Shim, H. Kim, L. Kong, Y. Meng, K. Wang, C. Kim, and J. Kim, "Path towards graphene commercialization from lab to market," *Nature nanotechnology*, vol. 14, no. 10, pp. 927–938, 2019.

[228] P. R. Kidambi, D. D. Mariappan, N. T. Dee, A. Vyatskikh, S. Zhang, R. Karnik, and A. J. Hart, "A scalable route to nanoporous large-area atomically thin graphene membranes by roll-to-roll chemical vapor deposition and polymer support casting," *ACS applied materials & interfaces*, vol. 10, no. 12, pp. 10 369–10 378, 2018.

[229] T. Yamada, M. Ishihara, J. Kim, M. Hasegawa, and S. Iijima, "A roll-to-roll microwave plasma chemical vapor deposition process for the production of 294 mm width graphene films at low temperature," *Carbon*, vol. 50, no. 7, pp. 2615–2619, 2012.

[230] G.-X. Ni, Y. Zheng, S. Bae, H. R. Kim, A. Pachoud, Y. S. Kim, C.-L. Tan, D. Im, J.-H. Ahn, B. H. Hong *et al.*, "Quasi-periodic nanoripples in graphene grown by chemical vapor deposition and its impact on charge transport," *ACS nano*, vol. 6, no. 2, pp. 1158–1164, 2012.

[231] B. N. Chandrashekar, B. Deng, A. S. Smitha, Y. Chen, C. Tan, H. Zhang, H. Peng, and Z. Liu, "Roll-to-roll green transfer of cvd graphene onto plastic for a transparent and flexible triboelectric nanogenerator," *Advanced materials*, vol. 27, no. 35, pp. 5210–5216, 2015.

[232] P. Hall and C. Hall, "Coplanar corporate feed effects in microstrip patch array design," in *IEE Proceedings H (Microwaves, Antennas and Propagation)*, vol. 135. IET, 1988, pp. 180–186.

[233] J. Huang, "Microstrip antenna developments at jpl," *IEEE Antennas and Propagation Magazine*, vol. 33, no. 3, pp. 33–41, 1991.

[234] M. J. Fitch and R. Osiander, "Terahertz waves for communications and sensing," *Johns Hopkins APL technical digest*, vol. 25, no. 4, pp. 348–355, 2004.

[235] D. L. Woolard, R. Brown, M. Pepper, and M. Kemp, "Terahertz frequency sensing and imaging: A time of reckoning future applications?" *Proceedings of the IEEE*, vol. 93, no. 10, pp. 1722–1743, 2005.

[236] J. Choi, V. Va, N. Gonzalez-Prelcic, R. Daniels, C. R. Bhat, and R. W. Heath, "Millimeter-wave vehicular communication to support massive automotive sensing," *IEEE Communications Magazine*, vol. 54, no. 12, pp. 160–167, 2016.

[237] S. Mumtaz, J. M. Jornet, J. Aulin, W. H. Gerstacker, X. Dong, and B. Ai, "Terahertz communication for vehicular networks," *IEEE Transactions on Vehicular Technology*, vol. 66, no. 7, 2017.

[238] R. Köhler, A. Tredicucci, F. Beltram, H. E. Beere, E. H. Linfield, A. G. Davies, D. A. Ritchie, R. C. Iotti, and F. Rossi, "Terahertz semiconductor-heterostructure laser," *Nature*, vol. 417, no. 6885, pp. 156–159, 2002.

[239] S. Preu, G. Döhler, S. Malzer, L. Wang, and A. Gossard, "Tunable, continuous-wave terahertz photomixer sources and applications," *Journal of Applied Physics*, vol. 109, no. 6, p. 4, 2011.

[240] R. Mendrzik, D. Cabric, and G. Bauch, "Error bounds for terahertz mimo positioning of swarm uavs for distributed sensing," in *2018 IEEE International Conference on Communications Workshops (ICC Workshops)*. IEEE, 2018, pp. 1–6.

[241] P. H. Siegel, P. de Maagt, and A. I. Zaghloul, "Antennas for terahertz applications," in *2006 IEEE Antennas and Propagation Society International Symposium*. IEEE, 2006, pp. 2383–2386.

[242] S. M. Farzaneh and S. Rakheja, "Voltage tunable plasmon propagation in dual gated bilayer graphene," *Journal of Applied Physics*, vol. 122, no. 15, p. 153101, 2017.

[243] S. Rakheja and P. Sengupta, "Gate-voltage tunability of plasmons in single-layer graphene structures—analytical description, impact of interface states, and concepts for terahertz devices," *IEEE Transactions on Nanotechnology*, vol. 15, no. 1, pp. 113–121, 2015.

[244] S. Dash and A. Patnaik, "Material selection for th z antennas," *Microwave and Optical Technology Letters*, vol. 60, no. 5, pp. 1183–1187, 2018.

[245] ——, "Performance of graphene plasmonic antenna in comparison with their counterparts for low-terahertz applications," *Plasmonics*, vol. 13, no. 6, pp. 2353–2360, 2018.

[246] J. M. Jornet and I. F. Akyildiz, "Graphene-based plasmonic nano-antenna for terahertz band communication in nanonetworks," *IEEE Journal on selected areas in communications*, vol. 31, no. 12, pp. 685–694, 2013.

[247] S. Dash, A. Patnaik, and B. K. Kaushik, "Performance enhancement of graphene plasmonic nanoantennas for thz communication," *IET Microwaves, Antennas & Propagation*, vol. 13, no. 1, pp. 71–75, 2019.

[248] S. Dash and A. Patnaik, "Dual band reconfigurable plasmonic antenna using bilayer graphene," in *2017 IEEE International Symposium on Antennas and Propagation & USNC/URSI National Radio Science Meeting*. IEEE, 2017, pp. 921–922.

[249] A. Hocini, M. Temmar, D. Khedrouche, and M. Zamani, "Novel approach for the design and analysis of a terahertz microstrip patch antenna based on photonic crystals," *Photonics and Nanostructures-Fundamentals and Applications*, vol. 36, p. 100723, 2019.

[250] H. Davoudabadifarahani and B. Ghalamkari, “High efficiency miniaturized microstrip patch antenna for wideband terahertz communications applications,” *Optik*, vol. 194, p. 163118, 2019.

[251] M. Koch, “Terahertz communications: A 2020 vision,” in *Terahertz frequency detection and identification of materials and objects*. Springer, 2007, pp. 325–338.

[252] K. Konstantinidis, A. P. Feresidis, Y. Tian, X. Shang, and M. J. Lancaster, “Micromachined terahertz fabry–perot cavity highly directive antennas,” *IET Microwaves, Antennas & Propagation*, vol. 9, no. 13, pp. 1436–1443, 2015.

[253] D. Kim, J. Hirokawa, M. Ando, J. Takeuchi, and A. Hirata, “32-element slot array antennas using double-layer hollow-waveguide corporate-feed in the 120 ghz band,” *IEEE Transactions on Antennas and Propagation*, vol. 62, no. 3, pp. 1507–1512, 2014.

[254] S. Y. Jun, B. Sanz-Izquierdo, E. A. Parker, D. Bird, and A. McClelland, “Manufacturing considerations in the 3-d printing of fractal antennas,” *IEEE Transactions on Components, Packaging and Manufacturing Technology*, vol. 7, no. 11, pp. 1891–1898, 2017.

[255] R. Sorrentino and O. A. Peverini, “Additive manufacturing: a key enabling technology for next-generation microwave and millimeter-wave systems [point of view],” *Proceedings of the IEEE*, vol. 104, no. 7, pp. 1362–1366, 2016.

[256] E. A. Rojas-Nastrucci, J. T. Nussbaum, N. B. Crane, and T. M. Weller, “Ka-band characterization of binder jetting for 3-d printing of metallic rectangular waveguide circuits and antennas,” *IEEE Transactions on Microwave Theory and Techniques*, vol. 65, no. 9, pp. 3099–3108, 2017.